Development of New Transition Metal Complexes Designed for Water Oxidation

Okamura, Masaya

SOKENDAI (The Graduate University for Advanced Studies)

School of Physical Sciences
Department of Structural Molecular Science

Contents

General Introduction

Water Oxidation in Oxygenic Photosynthesis

The oxidation of water into molecular oxygen ($2H_2O \rightarrow O_2 + 4H^+ + 4e^-$) is one of the most important and fundamental reactions on the Earth. The present our atmosphere consists mainly of nitrogen and oxygen, but it's not original atmosphere. An emergence of oxygenic photosynthetic organisms stated the water oxidation and caused the major transformation of global atmosphere into current O_2-rich environment. These organisms utilize the water oxidation reaction not to get oxygen, but to obtain "high energy electrons". Although oxygen itself is a by-product, the oxygenation of the atmosphere lead to thermodynamically more efficient O_2-based respiratory metabolisms that enable the development of the current diverse and complex life.[1]

The purpose of the oxygenic photosynthesis is harvesting energy in sunlight and storing it in the chemical compounds. Overviews of the oxygenic photosynthesis process are shown in Scheme 1. Photon from sun is collected at antenna molecules in the photosystem II (PSII) and is used to excite electrons to a higher energy level. The obtained high energy electrons are transferred to lower-energy molecule creating a chain of electron transfer reactions to ultimately perform CO_2 fixation into energy-rich carbohydrate and biomass. In this processes, the electrons and protons are originated from the water oxidation reaction. The water oxidation reaction thus serves as the bedrock for the photosynthesis system that all life depends on.

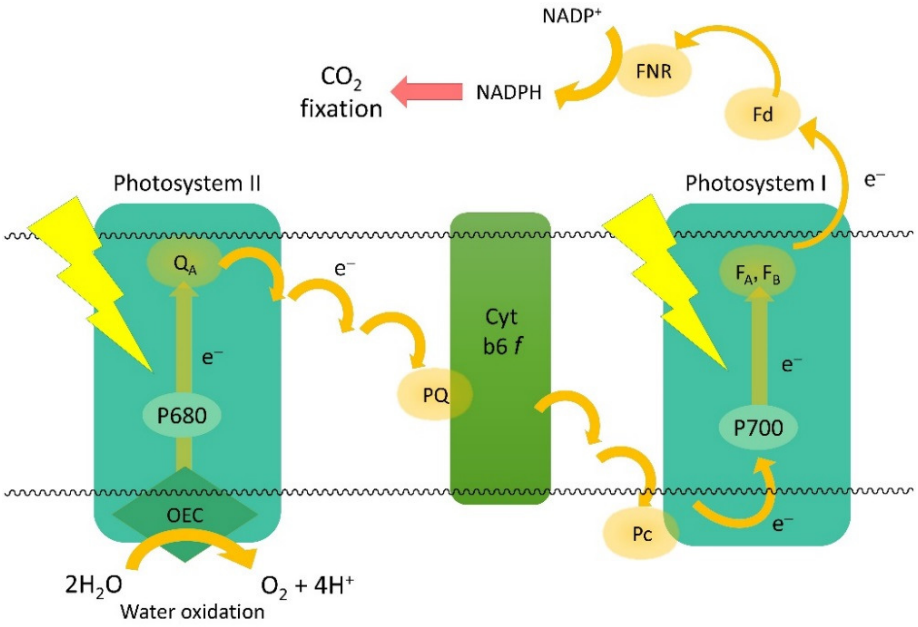

Scheme 1. Overview of the oxygenic photosynthesis

Water Oxidation in Artificial Photosynthesis

Humans have been used fossil fuel such as coal and oil to get heat or electricity. However, the burning of them causes air pollution and their sources are limited in the earth. Therefore, artificial photosynthesis that mimics natural photosynthesis cycle has attracted growing interest in recent years to replace fossil fuel with environment friendly fuels. In the artificial photosynthesis, sun light energy is stored in the form of the reduced compounds using the reaction shown in following schemes.

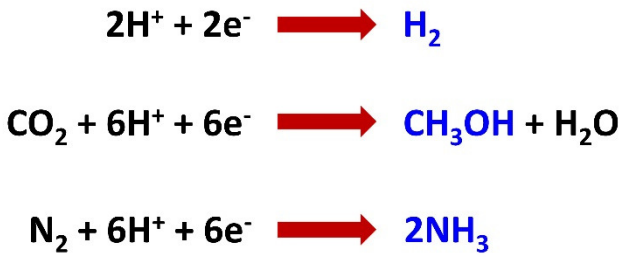

The protons and electrons required for making such chemical fuels should be extracted from the water oxidation because water is the most abundant, cheap and sustainable source of them. However, the creation of efficient water oxidation catalysts is difficult to achieve due to the complexity of the reaction, which needs the loss of $4e^-$ and $4H^+$ and the formation of the O-O bond from two water molecules. Therefore, the water oxidation reaction is an energy demanding process and occurs at +1.23 V *vs.* NHE in pH 0, as shown in Eq. (1).

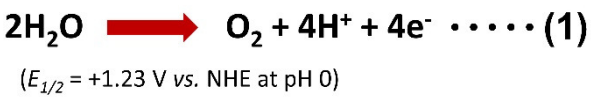

In order for this reaction to proceed at reasonable rates, higher applied potentials are required. The difference between the thermodynamic potential and applied potential is referred to as an overpotential. Because a high overpotential causes a significant loss of energy in the energy conversion from light, catalysts that can decrease the overpotential are required.

In nature, efficient light-driven water oxidation is achieved by an oxygen-evolving complex (OEC) embedded in PSII[2]. The OEC forms an O-O bond from two water molecules after storing four oxidizing equivalents that are provided by the energy of the four successive photons absorbed by a primary chlorophyll electron donor (P680) in PSII.[3] The oxidized $P680^+$ has a high redox potential (*ca.* +1.25 V *vs.* NHE)[4] and finally oxidizes water, mediated by a tyrosine residue (Y_Z). The Yz radical formed from Yz acts as an oxidant for the oxidation of the OEC. Given the estimated Y_Z•/Y_Z potential of 1.0-

1.2 V[5] and an O_2/H_2O couple equilibrium potential of 0.9 V at pH 5.5, the OEC drives the water oxidation within a very narrow range of overpotential (less than 0.3 V).[6]

Because the extraction of the OEC is extremely difficult, the development of various synthetic molecular catalysts have been investigated over the last decades[7] Initially, chemists have paid great attention to dinuclear complexes in hopes to facilitate the O_2-evolution reaction with the aid of two active centers.[8] Recently, some single-site ruthenium complexes were found to act as a water oxidation catalyst.[9-17] These findings are considered as significant progress because some single-site ruthenium complexes exhibited much-improved stability and activity compared with the dinuclear systems. It should be noted that the high activity and stability of single-site Ru complexes lead the detailed analysis of the water oxidation mechanism at the molecular level.

PCET in Water Oxidation

In water oxidation reactions by single-site ruthenium catalysts, high-valent ruthenium-oxo species (*e.g.*, Ru^{V}=O) are considered as the key intermediate triggering the formation of the O-O bond. The high-valent ruthenium-oxo species can be formed from Ru^{II}-OH_2 via stepwise electron removal involving concomitant proton loss, the so-called proton-coupled electron transfer (PCET) process.[18] A general scheme of the PCET process from Ru^{II}-OH_2 to Ru^{IV}=O is shown in Scheme 2.

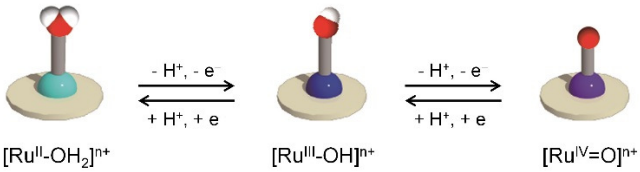

Scheme 2. Two-step PCET reaction between Ru^{II}-OH_2 and Ru^{IV}=O. The ligands are illustrated as a round plate and the colored spheres represent the following atoms (Ru^{II} = light blue, Ru^{III} = blue, Ru^{IV} = purple, O = red and H = white).

With increasing positive charge of the metal ion, the acidity of the protons of the attached water molecule is enhanced, leading to the simultaneous proton release. Importantly, the PCET process can suppress the build-up of total charge of the complex during the electron transfer reactions and, therefore, can dramatically decrease the redox potentials to make high-valent species.

For the typical example of a single-site ruthenium complex, $[Ru^{II}(trpy)(bpy)(OH_2)]^{2+}$ (**1** in Figure 1, trpy = 2,2':6',2"-terpyridine, bpy = 2,2'-bipyridine), the redox potentials for $[Ru^{III}\text{-}OH]^{2+}/[Ru^{II}\text{-}OH_2]^{2+}$ and $[Ru^{IV}{=}O]^{2+}/[Ru^{III}\text{-}OH]^{2+}$ are 0.73 V and 0.86 V *vs.* NHE at pH 7, respectively.[19] Given that the potentials for Ru^{III}/Ru^{II} and Ru^{IV}/Ru^{III} in *cis*-$[Ru(bpy)_2Cl_2]^{n+}$ (n = 0-2) are 0.08 V and 1.74 V, respectively (ΔE = 1.66 V),[20] the difference between the two redox potentials for **1** (ΔE = 0.13 V) is very small. The small difference comes from the avoidance of charge build-up in the electron transfer reaction. Moreover, a π-donation from a *p* orbital of the oxo moiety to a *d* orbital of the Ru atom also stabilizes the high-valent state of the Ru center. Thus, the Ru^{IV}=O/Ru^{II}-OH_2 system plays the important role of accumulating multiple oxidizing equivalents over a small potential range. By contrast, further one-electron oxidation of $[Ru^{IV}{=}O]^{2+}$ to form $[Ru^{V}{=}O]^{3+}$ species for **1** is not accompanied by proton loss, and occurs at 1.60 V.[9d] The difference of the two potentials between Ru^{IV}/Ru^{III} and Ru^{V}/Ru^{IV} (ΔE = 0.74 V) is very large compared to that between Ru^{III}/Ru^{II} and Ru^{IV}/Ru^{III} (ΔE = 0.13 V).

The $[Ru^{V}{=}O]^{3+}$ state of **1** is the active species for O-O bond formation in water oxidation catalyzed by **1**, and the most oxidized state during the reaction. The electronic

structure of the $[Ru^{V}=O]^{3+}$ state of **1** was previously discussed based on the results of DFT calculations.[10e] In consequence, the O(oxo) atom of the $[Ru^{V}=O]^{3+}$ species was found to be possess a substantial radical character, in which 61% of the Mulliken spin density was located at the O(oxo) atom. This result indicates that the $[Ru^{V}=O]^{3+}$ species bears a character of ruthenium(IV) oxyl radical, which can be represented by using two resonance structures ($Ru^{V}=O \leftrightarrow Ru^{IV}$-O•). Because the $Ru^{V}=O$ species triggers the O-O bond formation, the redox potentials for Ru^{V}/Ru^{IV} are closely related to the onset potentials for water oxidation. Thus the development of single-site ruthenium catalysts with the low Ru^{V}/Ru^{IV} potentials can conduce to the creation of the low overpotential catalysts, although the rapid follow-up reactions of the $Ru^{V}=O$ species is also important to lower the overpotential.

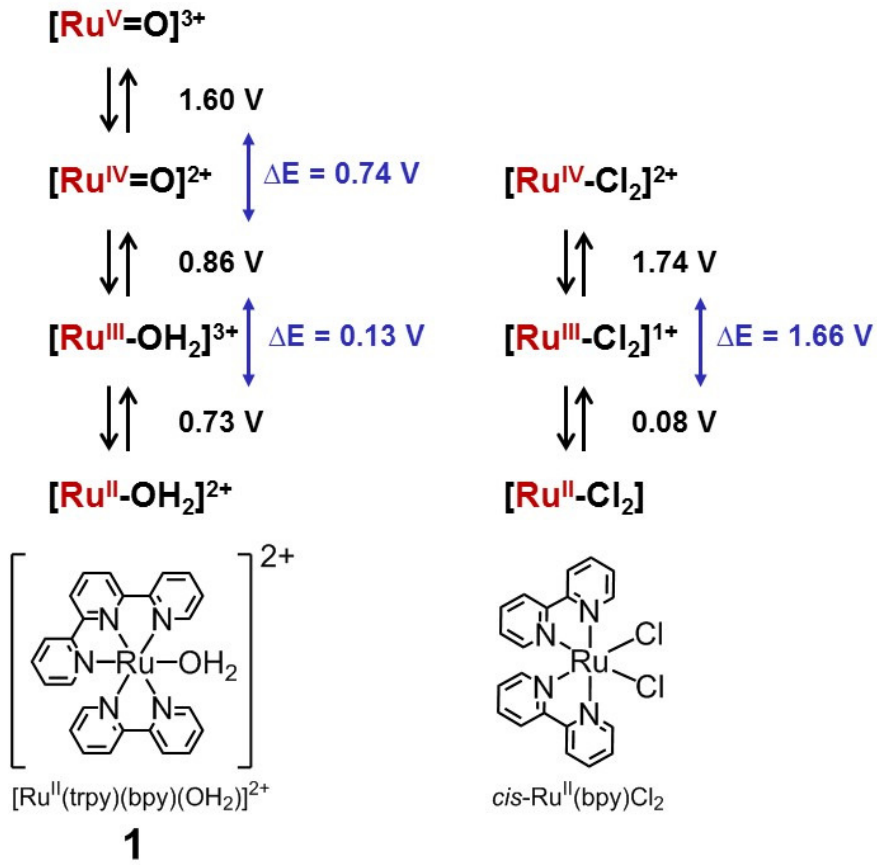

Figure 1. Redox potentials of Ru complexes in the PCET process and non-PCET process.

Strategies to Decrease the Overpotential

The O-O bond formation in water oxidation by single-site ruthenium complexes is most often triggered by an active Ru^{V}=O species. However, in general, a very high oxidizing potential needs to be applied to form the Ru^{V}=O species even though the formation of a Ru^{IV}=O species is easily accessible. As a result, very strong oxidants such as Ce^{4+} have often been employed to perform the water oxidation catalyses. However, to apply those catalysts to solar energy conversion systems, the development of catalysts driven at low overpotentials is required because high overpotentials cause significant energy losses in the conversion of energy from light. Therefore, several molecular designs to achieve low-overpotential water oxidation are described below.

Substituent Effect

The substituent effect for $[Ru(tpy)(bpy)(OH_2)]^{2+}$ (**1**) on catalytic behaviours were investigated by Berlinguette and co-workers.[12a,12b] They performed a variety of substitutions including both electron-donating (*e.g.*, -OMe) and electron-withdrawing (*e.g.*, -Cl, -COOH) groups, at the tpy and/or bpy ligand. In cyclic voltammetry, they observed that the Ru^{V}/Ru^{IV} potentials for the derivatives with electron-donating groups (*e.g.*, 1.63 V for **1c**) were lower than those with electron-withdrawing groups (*e.g.*, 1.71 V for **1a**, 1.80 V for **1b**).[12a] Thus, the presence of electron-donating groups can decrease the potential to produce Ru^{V}=O species. They also mentioned that the increase of the electron density at Ru center accelerate initial rate of oxygen evolution, however, decrease the stability of the catalyst in the Ce^{4+}-driven water oxidation.

Similar results have been obtained in other catalyst systems.[10b, 10c,11] Sakai and co-workers, synthesized a series of single-site ruthenium complexes containing facial-type tridentate ligands, $[Ru^{II}(tmtacn)(R_2bpy)(OH_2)]^{2+}$ (**2** for R = H, **2a** for R = Me, and **2b** for R = OMe) and $[Ru^{II}(tpzm)(R_2bpy)(OH_2)]^{2+}$ (**3** for R = H, **3a** for R = Me, and **3b** for R = OMe), and evaluated their catalytic activity for electrocatalytic water oxidation.[10c] The cyclic voltammograms showed that the stronger electron-donating groups (-OMe > -Me > -H) gave rise to a larger negative shift in the onset potentials for water oxidation.

Sun and co-workers demonstrated that the use of negatively charged ligands can stabilize the high-valent Ru^{V}=O states of single-site ruthenium catalysts.[11] Cyclic voltammograms of **4a** in acidic solution at pH 1 showed oxidation waves at 0.86 V *vs*. NHE for Ru^{III}/Ru^{II} and at 1.11 V for Ru^{IV}/Ru^{III}. The onset of water oxidation for **4a** occurs at approximately 1.5 V,[11b] which is relatively small compared with other complexes. Moreover, the lower onset potential of *ca*. 1.1 V at pH 1 was achieved for complex **4b,** in which the water oxidation reaction was enhanced by the non-covalent interactions

between isoquinolines.[11m] The onset potential of **4a** decreased to *ca*. 1.0 V in a pH 7.0 aqueous solution. Because of the low overpotential of **4a** for water oxidation at neutral pH, they accomplished light-driven water oxidation by using the photogenerated $[Ru(bpy)_3]^{3+}$ (1.26 V) as a mild oxidant. It has also been reported that the introduction of imidazole and its derivatives to the axial position of ruthenium catalysts (**5**, **5a**, **5b** and **5c**) is an effective strategy to lower the onset potentials for water oxidation due to the electron-donating ability of the imidazoles.[11o]

They also noted that the substitution effect is less influential on the higher oxidation states in a series of $Ru(bda)L_2$ (**6**) by modifying the 4-position of the pyridine ligand with electron-donating and withdrawing substituents.[11p] The potentials of $E_{1/2}$ for Ru^{III}/Ru^{II} decreases from 0.75 to 0.47 V as the axial ligand was changed from the electron-withdrawing group to the electron-donating group. However, the difference in $E_{1/2}$ for Ru^{IV}/Ru^{III} of these complexes is less than 50 mV, and the onset potentials for water oxidation are almost the same. It should also be noted that the electron-donating and electron-withdrawing substituents may have an opposite effect on the potential in case that the redox process involves the transfer of a proton, *i.e.*, a PCET process.[12b] For example, the introduction of electron-donating groups causes the increase of electron density at the Ru center, thus leading to the elevation of the pK_a value of the [Ru-OH_2] or [Ru-OH] complex. In the case of a PCET process, the oxidation potential may increase by electron-donating groups because the proton is hard to release from the electron-rich metal center.

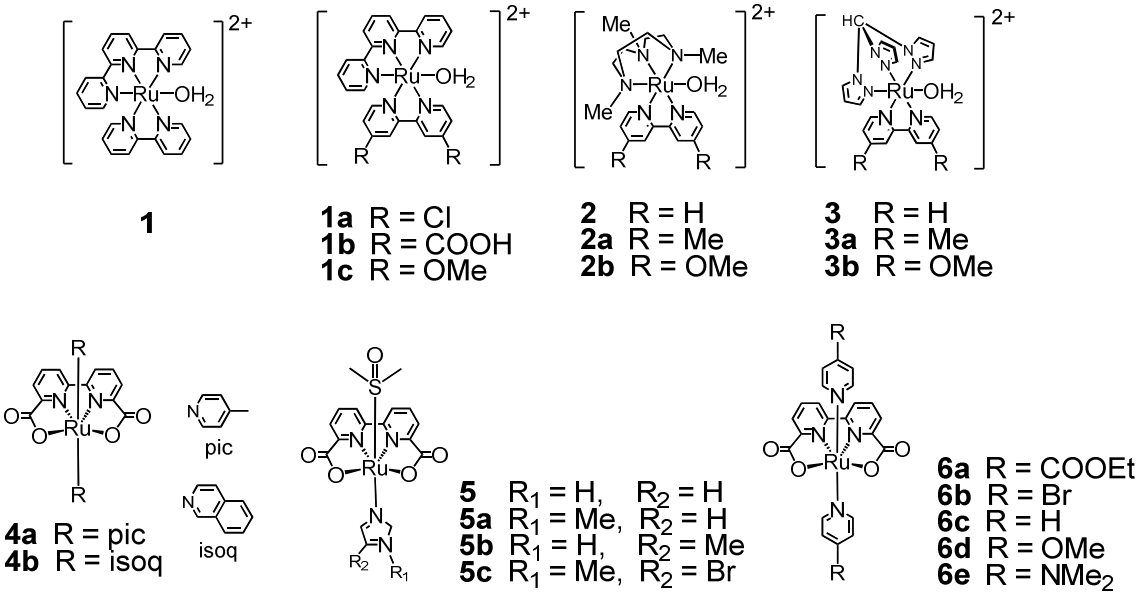

Figure 2. Structures of the complex aimed for substitution effect.

Redox Mediator

For water oxidation with a low overpotential, Meyer and co-workers introduced an electron-transfer mediator into a single-site ruthenium complex.[9k] They employed a new ruthenium catalyst, $[(bpy)_2Ru(BL)Ru(tpy)(OH_2)]^{4+}$ (**8a**, BL = bridging ligand, see Figure 4) and the phosphonic acid-derivatised complex (**8b**), by combining a $[Ru(bpy)_3]^{2+}$ redox mediator and a single-site ruthenium catalyst (**7**). The cyclic voltammograms of **8b** loaded on a fluoride-doped tin oxide (FTO) electrode showed a reversible oxidation at 0.90 V for the $[Ru_a^{II}\text{-}Ru_b^{III}\text{-}OH_2]^{5+}/[Ru_a^{II}\text{-}Ru_b^{II}\text{-}OH_2]^{4+}$ couple followed by a second oxidation for the $[Ru_a^{II}\text{-}Ru_b^{IV}{=}O]^{4+}/[Ru_a^{II}\text{-}Ru_b^{III}\text{-}OH_2]^{5+}$ couple at 1.15 V, where Ru_a is the ruthenium center in the redox mediator and Ru_b is that in the catalyst. For the mononuclear catalyst **7**, water oxidation started at approximately 1.55 V for $[Ru^{V}{=}O]^{3+}/[Ru^{IV}{=}O]^{2+}$ (Fig. 3).

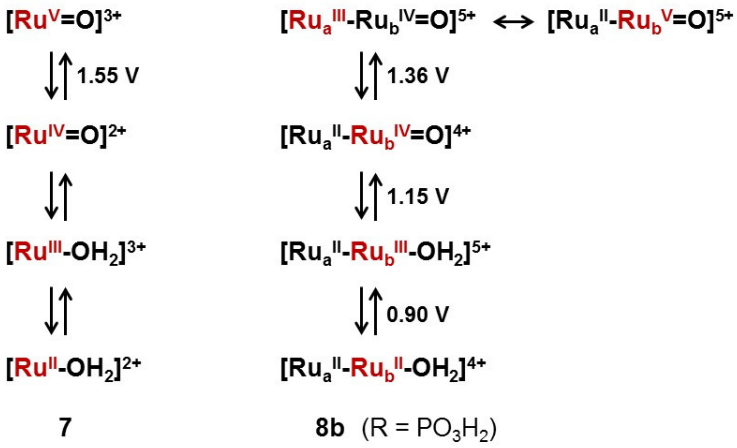

Figure 3. Redox mediator effect on water oxidation.

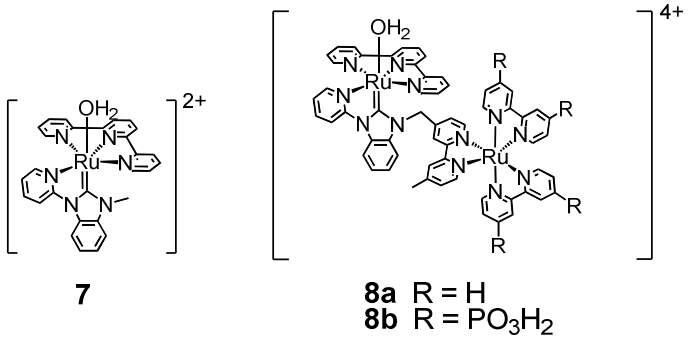

Figure 4. Structures of the complex with redox mediator.

Interestingly, in the case of **8b**, oxidation of the redox mediator began at 1.36 V to form $[Ru_a^{III}\text{-}Ru_b^{IV}=O]^{5+}$, which triggers the water oxidation. The "redox isomer" $[Ru_a^{II}\text{-}Ru_b^{V}=O]^{5+}$ is an active species responsible for O-O bond formation. This equilibrium enables the avoidance of the further direct oxidation of $[Ru_a^{III}\text{-}Ru_b^{IV}=O]^{5+}$ to $[Ru_a^{III}\text{-}Ru_b^{V}=O]^{6+}$ at approximately 1.5 V. To demonstrate the low-overpotential oxidation of water, they evaluated the oxygen evolution activity by rotating ring-disk electrode (RRDE) voltammetry for **8b** attached to a film of mesoporous, nano-structured, tin-doped indium oxide (nanoITO). In this experiment, oxygen was detected at the Pt ring of the RRDE by dual-electrode cyclic voltammetry (DECV). For positive sweepings, a large increase in disk current assigned to the water oxidation occurred at 1.40 V which corresponds to the potential for oxidation of the redox mediator modified on the electrode surface. The onset potential of **8b** is lower than the potential required for the oxidation of **7** to the $[Ru^{V}=O]^{3+}$ species (1.55 V).

Utilization of PCET

Another way to decrease the redox potential is to introduce PCET, which is a fundamental process in nature. Most single-site ruthenium complexes require the formation of a catalytically active Ru^{V}=O intermediate in which the Ru^{V}=O/Ru^{IV}=O couple is pH independent[9-12,15]. Therefore, as the pH increases, the thermodynamic potential for the O_2/H_2O couple decreases, while the onset potential of the catalysis remains unchanged.

$[Ru(L)(pic)_2(H_2O)]^{2+}$ (**7** and **8**, L = 4-*t*-butyl-2,6-di-1',8'-(naphthyrid-2'-yl)-pyridine and 2,6-bis(benzo[*b*]-1',8'-naphthyridin-2'-yl)-4-*t*-butylpyridine, respectively), in which the coordinated water molecule is hydrogen-bonded to the non-coordinated nitrogen atom in equatorial ligand L, Fujita *et al*. found that the O-O bond formation can proceed through the thermodynamically more favourable "direct pathway" via $[Ru^{IV}=O]^{2+}$, which avoid the formation of $[Ru^{V}=O]^{3+}$ in neutral and basic media (Fig. 5).[13b-13e] A four-electron oxidation of $[Ru^{II}\text{-}OH_2]^{2+}$ by the bulk electrolysis at 1.15 V at pH 6 yielded a red coloured solution. The obtained product was determined to be $[Ru^{IV}\text{-}OO]^{2+}$ by ESI-MS with labelling experiments, UV-vis and resonance Raman spectroscopy. The oxidation of $[Ru^{IV}=O]^{2+}$ is a pH-independent process and it takes place at 1.42 V. Thus, the O-O bond formation proceeded at the applied potentials (1.15 V) without the formation of the $[Ru^{V}=O]^{3+}$ species (1.42 V).

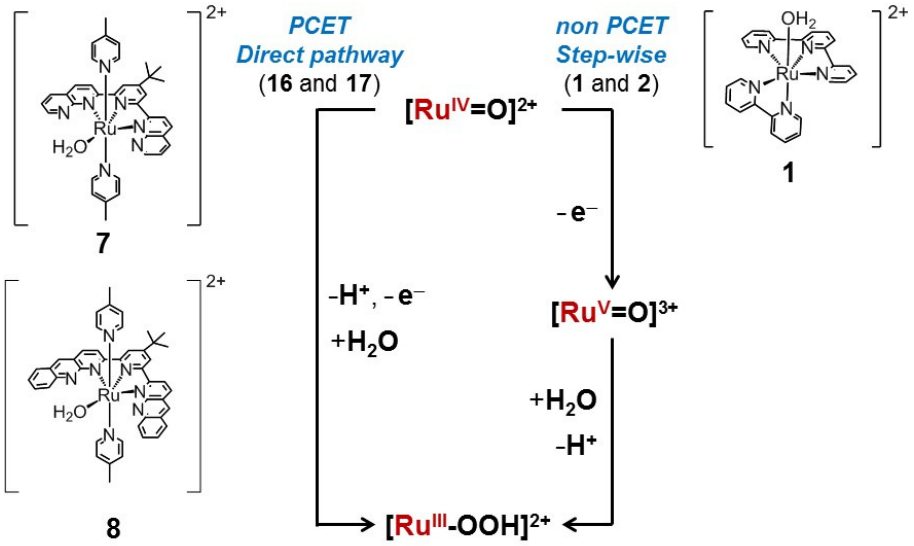

Figure 5. Direct pathway via the PCET reaction from $[Ru^{IV}=O]^{2+}$ to $[Ru^{III}\text{-}OOH]^{2+}$, which avoids the higher oxidation state $[Ru^{V}=O]^{3+}$.

From these results, they proposed that at higher pH, the formation of $[Ru^{III}\text{-}OOH]^{2+}$ proceeds through the reaction of $[Ru^{IV}=O]^{2+}$ with a water molecule concomitant with the loss of an electron and a proton. Indeed, they found that the onset of the catalytic current

exhibits pH dependence with a slope of -59 mV/pH in the pH range from 4 to 11, indicating a low-energy pathway of O-O bond formation through the PCET process. The direct pathway enables the photocatalytic water oxidation reaction by $[Ru(bpy)_3]^{2+}$ at high pH. Photogenerated $[Ru(bpy)_3]^{3+}$ (1.26 V) cannot thermodynamically produce the $[Ru^{V}=O]^{3+}$ species in the catalyses for **1**, but the direct-pathway reactions for **7** and **8** are pH dependent, and the O-O bond formation can be achieved at relatively low potentials under the neutral conditions (Fig. 5).

It should also be mentioned here that Åkermark *et al*. reported two systems of low overpotential-driven water oxidation.[14a,14b] They employed the tridentate ligand, which consists of imidazole and phenol motifs, in combination with carboxylate groups to introduce both a redox and proton transfer mediator (**9** and **10** in Figure. 6).[14a] The cyclic voltammograms shows three oxidation waves assigned to Ru^{III}/Ru^{II}, Ru^{IV}/Ru^{III} and Ru^{V}/Ru^{IV} and all three oxidation steps displayed pH dependence with a slope of -59 mV/pH. The onset of the catalytic reaction was observed at *ca*. 1.24 V at pH 7. Because of the low overpotential, the light-driven water oxidation was achieved by using the $[Ru(bpy)_3]^{2+}$ photosensitiser (1.26 V). They also reported unique oxidation behaviour in $[Ru(bpb)(pic)_2]^{+}$ (**11**, H_2bpb = *N,N'*-1,2-phenylene-bis (2-pyridine-carboxamide)), which also drive the water oxidation by $[Ru(bpy)_3]^{2+}$.[14b] The differential pulse voltammograms (DPVs) at pH 7.2 exhibited three oxidation waves at 0.15, 0.70 and 0.98 V, which correspond to Ru^{III}/Ru^{II}, Ru^{IV}/Ru^{III} and Ru^{VI}/Ru^{IV}, respectively. From the Pourbaix diagram, the third oxidation process shows a slope of -29 mV/pH, implying the formation of $Ru^{VI}=O$ species as the active species for O-O bond formation.

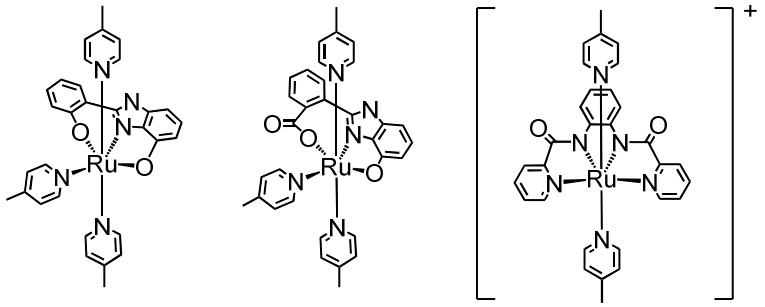

9 **10** **11**

Figure 6. Structures of the complex aimed for PCET.

Survey of this thesis

Chapter 1 describes the synthesis and characterization of a new ruthenium(II) complex showing multiple PCET by incorporating two kinds of PCET modules in a single molecule. Two new ruthenium(II) complexes bearing dissociable protons, $[Ru(trpy)(H_2bim)Cl]PF_6$ (**1**) and $[Ru(trpy)(H_2bim)(OH_2)](PF_6)_2$ (**2**) (H_2bim = 2,2'-biimidazole and trpy = 2,2':6',2"-terpyridine), were synthesized and characterized, where the H_2bim and M-OH_2 moieties are expected to serve as proton-dissociation sites. Electrochemical studies of **2** demonstrates four-step proton-coupled electron transfer (PCET) to give the four-electron oxidized species, $[Ru^{IV}(trpy)(bim)(O)]^{2+}$, without electrostatic charge buildup during the reactions. This multiple PCET of **2** would be applicable to various multi-electron oxidation reactions. Catalysis of electrochemical water oxidation was evaluated in the initial attempt to demonstrate multi-electron oxidation reactions, revealing that the water oxidation potential for **2** is lower than that for other ruthenium catalysts, $[Ru(trpy)(bpy)(OH_2)]^{2+}$, $[Ru(trpy)(bpm)(OH_2)]^{2+}$ and $[Ru(tmtacn)(bpy)(OH_2)]^{2+}$, (bpy = 2,2'-bipyridine, bpm = 2,2'-bipyrimidine, and tmtacn = 1,4,7-trimethyl-1,4,7-triazacyclononane), which are known as active catalysts for water oxidation.

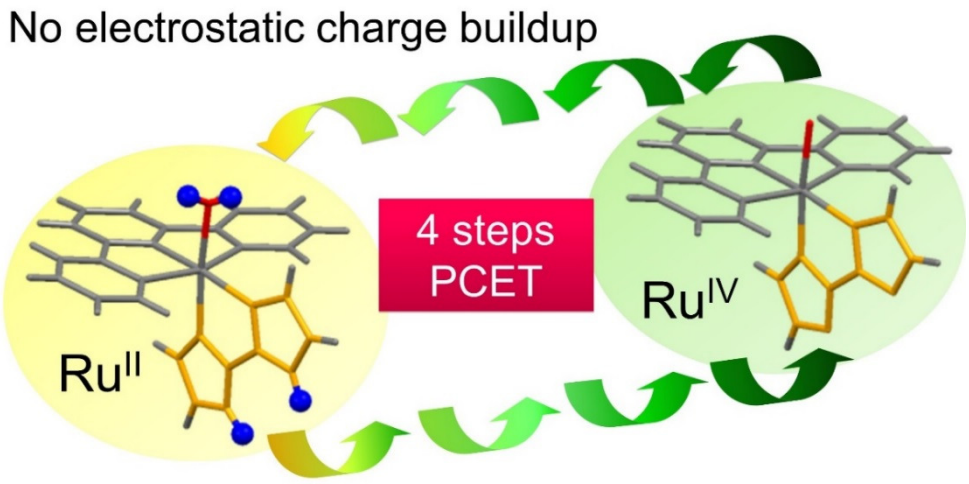

Chapter 2 describes a water oxidation reaction catalyzed by a pentanuclear iron complex. Inspired by the structures of biological active sites and artificial molecular catalysts, multinuclear iron complexes with redox flexibility and adjacent water-activation sites was employed. Electrochemical analysis revealed that the pentairon complex exhibits rich redox flexibility with six different oxidation states between Fe^{II}_5 and Fe^{III}_5, in which the Fe^{III}_5 state is the active species for oxidizing water. The turnover frequency of the water oxidation catalyst was determined to be 1,900 s^{-1}, which is considerably greater than that of the OEC (100-400 s^{-1}). A computational investigation indicated that the O-O bond formation proceeds from the mixed-valence $Fe^{II}_2Fe^{III}(Fe^{IV}{=}O)_2$ intermediate with a reaction barrier of less than 10 kcal mol^{-1}. Although the need for a high overpotential and inability to operate in water-rich solutions limit the practicality of the present system, these findings clearly indicate that efficient water oxidation catalysts based on iron complexes can be created by ensuring the system has redox flexibility and contains adjacent water-activation sites.

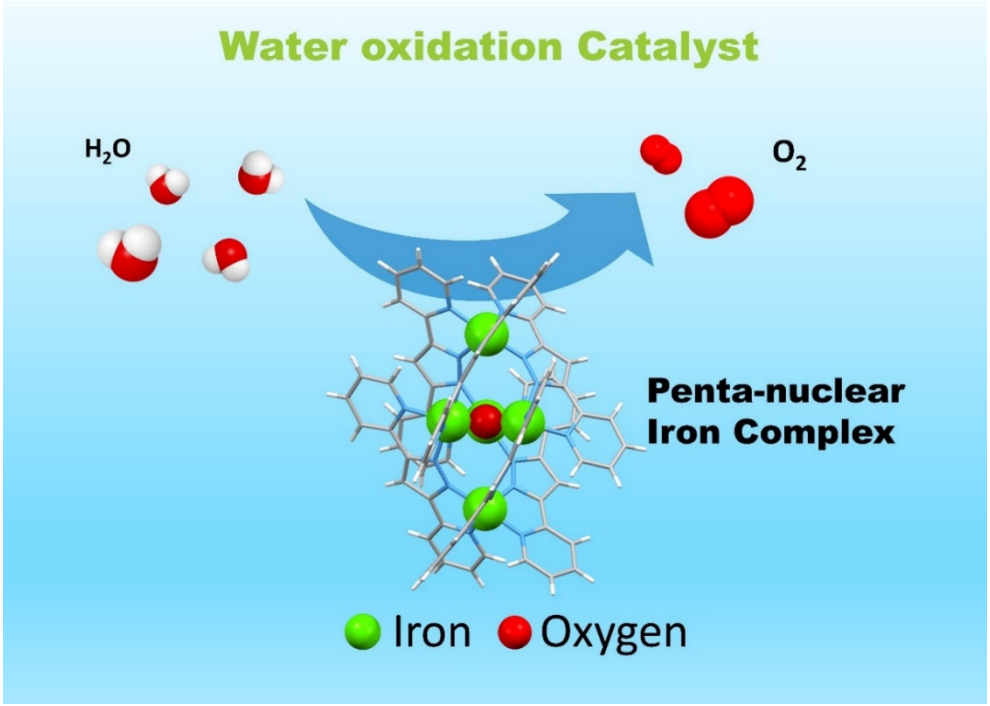

Chapter 3 describes a new penta-nuclear iron complex bearing the proton dissociative sites showing the water oxidation with a lower overpotential. The ligand with proton coupled electron transfer (PCET) sites, 3,5-(2-benzimidazolyl)pyrazole (H_3bip), is installed into the penta-nuclear iron complex. A novel complex, $[Fe_5O(H_2bip)_5]^{3+}$, was successively synthesized by the reaction of $Fe(ClO_4)_2 \cdot 6H_2O$ and 1 equiv. of H_3bip with base in DMF at 90 °C. The cyclic voltammetry (CV) in various pH solution using the complex-modified electrode revealed pH-dependent shifts in the oxidation potentials of the complex, which is not observed in the $[Fe_5O(bpp)_5]^{3+}$. Furthermore, the catalytic current attributed to water oxidation was observed at lower oxidation potential than that of $[Fe_5O(bpp)_5]^{3+}$. The results of this work indicate that molecular design of catalytic systems capable of PCET is critical to the development of water oxidation catalysts with a low overpotential.

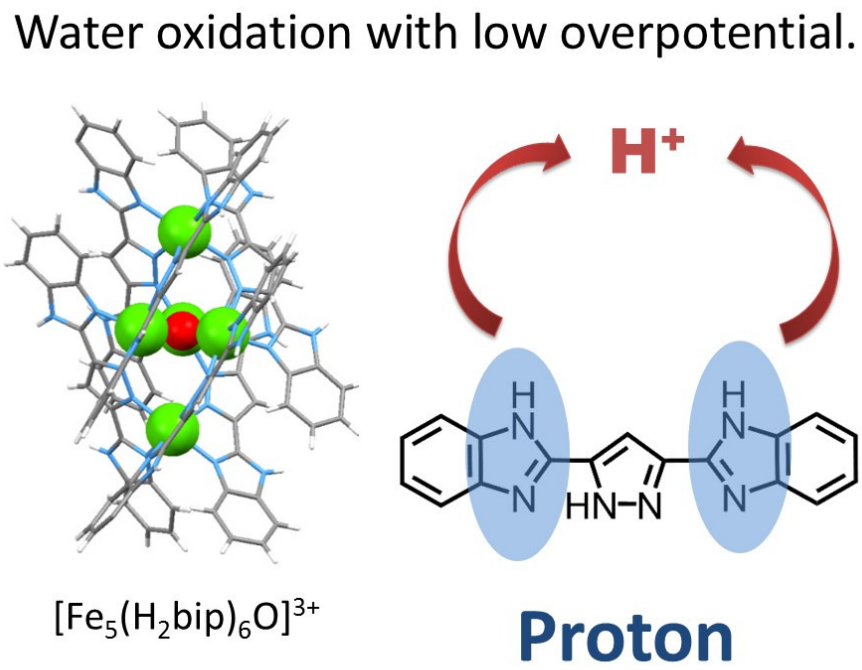

References

1. J. Raymond and D. Segrè, *Science* **2006**, *311*, 1764; b) G. J. Burton, *J. Anat*. **2009**, *215*, 27.
2. Y. Umena, K. Kawakami, J.-R. Shen and N. Kamiya, *Nature* **2011**, *473*, 55.
3. a) B. Kok, B. Forbush and M. McGloin, *Photochem. Photobiol*. **1970**, *11*, 457; b) J. P. McEvoy and G. W. Brudvig, *Chem. Rev.* **2006**, *106*, 4455; c) A. Klauss, M. Haumann and H. Dau, *Proc Natl Acad Sci USA* **2012**, *109*, 16035; d) N. Cox, D. A. Pantazis, F. Neese and W. Lubitz, *Acc. Chem. Res.* **2013**, *46*, 1588.
4. a) F. Rappaport, M. Guergova-Kuras, P. J. Nixon, B. A. Diner and J. Lavergne, *Biochemistry* **2002**, *41*, 8518; b) M. Grabolle and H. Dau, *Biochim. Biophys. Acta* **2005**, *1708*, 209.
5. a) C, Tommos and G. T. Babcock, *Biochim. Biophys. Acta* **2000**, *1458,* 199; b) W. Lubitz, E. J. Reijerse and J. Messinger, *Energy Environ. Sci.* **2008**, *1*, 15; c) F, Rappaport and B. A. Diner, *Coord. Chem. Rev.* **2008**, *252*, 259.
6. H. Dau and I. Zaharieva, *Acc. Chem. Res*. **2009**, *42*, 1861.
7. a) G. W. Brudvig and R. H. Crabtree, *Prog. Inorg. Chem.* **1989**, *37*, 99; b) T. J. Meyer, *Acc. Chem. Res.* **1989**, *22*, 163; c) W. Rüttinger and C. Dismukes, *Chem. Rev.* **1997**, *97*, 1; d) M. Yagi and Kaneko, *Chem. Rev.* **2001**, *101*, 21; e) I. Romero, M. Rodríguez, C. Sens, J. Mola, M. R. Kollipara, L. Francàs, E. Mas-Marza, L. Escriche and A. Llobet, *Inorg. Chem.* **2008**, *47*, 1824; f) H. Dau, C. Limberg, T. Reier, M. Risch, S. Roggan and P. Strasser, *ChemCatChem* **2010**, *2*, 724; g) X. Liu and F. Wang, *Coord. Chem. Rev.* **2012**, *256*, 1115; h) R. Cao, W. Lai and P. Du, *Energy Environ. Sci.* **2012**, *5*, 8134; i) D. J. Wasylenko, R. D. Palmer and C. P. Berlinguette, *Chem. Commun.* **2013**, *49*, 218; j) A. Singh and L. Spiccia, *Coord. Chem. Rev.* **2013**, *257*, 2607; k) T. Kikuchi and K. Tanaka, *Eur. J. Inorg. Chem.* **2014**, *4*, 607.
8. a) S. W. Gersten, G. J. Samuels and T. J. Meyer, *J. Am. Chem. Soc.* **1982**, *104*, 4029; b) R. Ramaraj, A. Kira and M. Kaneko, *Angew. Chem. Int. Ed. Engl.* **1986**, *25*, 1009; c) F. P. Rotzinger, S. Munavalli, P. Comte, J. K. Hurst, M. Grätzel, F. Pern and A. J. Frank, *J. Am. Chem. Soc*. **1987**, *109*, 6619; d) M. Yagi, Y. Osawa, N. Sukegawa and M. Kaneko, *Langmuir* **1999**, 15, 7406; e) T. Wada, K. Tsuge and K. Tanaka, *Angew. Chem. Int. Ed*. **2000**, *39*, 1479; f) C. Sens, I. Romero, M. Rodíguez, A. Llobet, T. Parella and J. Benet-Buchholz, *J. Am. Chem. Soc.* **2004**, *126*, 7798; g) R. Zong and R. P. Thummel, *J. Am. Chem. Soc.* **2005**, *127*, 12802; h) Y. Xu, T. Åkermark, V. Gyollai, D. Zou, L. Eriksson, L. Duan, R. Zhang, B. Åkermark and L. Sun, *Inorg. Chem.* **2009**, *48*, 2717; i) Y. Xu, A. Fischer, L. Duan, L. Tong, E. Gabrielsson, B. Åkermark and L. Sun, *Angew. Chem. Int. Ed.* **2010**, *49*, 8934; j) D. J. Wasylenko, C.

Ganesamoorthy, B. D. Koivisto and C. P. Berlinguette, *Eur. J. Inorg. Chem.* **2010**, 3135; k) Y. Xu, L. Duan, T. Åkermark, L. Tong, B.-L. Lee, R. Zhang, B. Åkermark and L. Sun, *Chem. Eur. J.* **2011**, *17*, 9520.

9. a) J. J. Concepcion, J. W. Jurss, J. L. Templeton and T. J. Meyer, *J. Am. Chem. Soc.* **2008**, *130,* 16462; b) Z. Chen, J. J. Concepcion, J. W. Jurss and T. J. Meyer, *J. Am. Chem. Soc.* **2009**, *131*, 15580; c) J. J. Concepcion, J. W. Jurss, P. G. Hoertz and T. J. Meyer, *Angew. Chem. Int. Ed.* **2009**, *48*, 9473; d) J. J. Concepcion, J. W. Jurss, M. R. Norris, Z. Chen, J. L. Templeton and T. J. Meyer, *Inorg. Chem.* **2010**, *49*, 1277; e) J. J. Concepcion, M.-K. Tsai, J. T. Muckerman and T. J. Meyer, *J. Am. Chem. Soc.* **2010**, *132*, 1545; f) Z. Chen, J. J. Concepcion, H. Luo, J. F. Hull, A. Paul and T. J. Meyer, *J. Am. Chem. Soc.* **2010**, *132*, 17670; g) Z. Chen, J. J. Concepcion, X. Hu, W. Yang, P. G. Hoertz and T. J. Meyer, *Proc. Natl. Acad. Sci. USA* **2010**, *107*, 7225; h) Z. Chen, J. J. Concepcion, J. F. Hull, P. G. Hoertz and T. J. Meyer, *Dalton Trans.* **2010**, *39*, 6950; i) Z. Chen, J. J. Concepcion and T. J. Meyer, *Dalton Trans*. **2011**, *40*, 3789; j) D. L. Ashford, D. J. Stewart, C. R. Glasson, R. A. Binstead, D. P. Harrison, M. R. Norris, J. J. Concepcion, Z. Fang, J. L. Templeton and T. J. Meyer, *Inorg. Chem*. **2012**, *51*, 6428; k) M. R. Norris, J. J. Concepcion, Z. Fang, J. L. Templeton and T. J. Meyer, *Angew. Chem. Int. Ed*. **2013**, *52*, 13580; l) M. R. Norris, J. J. Concepcion, D. P. Harrison, R. A. Binstead, D. L. Ashford, Z. Fang, J. L. Templeton and T. J. Meyer, *J. Am. Chem. Soc*. **2013**, *135*, 2080; m) J. J. Concepcion, R. A. Binstead, L. Alibabaei and T. J. Meyer, *Inorg. Chem*. **2013**, *52*, 10744.
10. a) S. Masaoka and K. Sakai, *Chem. Lett.* **2009**, *38*, 182; b) M. Yoshida, S. Masaoka and K. Sakai, *Chem. Lett.* **2009**, *38*, 702; c) M. Yoshida, S. Masaoka, J. Abe and K. Sakai, *Chem. Asian J.* **2010**, *5*, 2369; d) J. Kiyota, J. Yokoyama, M. Yoshida, S. Masaoka and K. Sakai, *Chem. Lett.* **2010**, *39*, 1146; e) A. Kimoto, K. Yamauchi, M. Yoshida and S. Masaoka, *Chem. Commun.* **2012**, *48*, 239; f) M. Okamura, M. Yoshida, R. Kuga, K. Sakai, M. Kondo and S. Masaoka, *Dalton Trans*. **2012**, *41*, 13081; g) G. Nakamura, M. Okamura, M. Yoshida, T. Suzuki, H. D. Takagi, M. Kondo and S. Masaoka, *Inorg. Chem.* **2014**, *53*, 7214.
11. a) L. Duan, A. Fischer, Y. Xu and L. Sun, *J. Am. Chem. Soc.* **2009**, *131*, 10397; b) L. Duan, Y. Xu, P. Zhang, M. Wang and L. Sun, *Inorg. Chem.* **2010**, *49*, 209; c) J. Nyhlén, L. Duan, B. Åkermark, L. Sun and T. Privalov, *Angew. Chem. Int. Ed.* **2010**, *49*, 1773; d) L. Li, L. Duan, Y. Xu, M. Gorlov, A. Hagfeldt and L. Sun, *Chem. Commun.* **2010**, *46*, 7307; e) L. Duan, Y. Xu, M. Gorlov, L. Tong, S. Andersson and L. Sun, *Chem. Eur. J.* **2010**, *16*, 4659; f) L. Tong, L. Duan, Y. Xu, T. Privalov and L. Sun, *Angew. Chem. Int. Ed.* **2011**, *50*, 445; g) T. Privalov, B. Åkermark and L. Sun, *Chem. Eur. J.*

2011, *17*, 8313; h) Y. Xu, L. Duan, T. Åkermark, L. Tong, B.-L. Lee, R. Zhang, B. Åkermark and L. Sun, *Chem. Eur. J.* **2011**, *17*, 9520; i) L. Duan, Y. Xu, L. Tong and L. Sun, *ChemSusChem*. **2011**, *4*, 238; j) L. Tong, Y. Wang, L. Duan, Y. Xu, X. Cheng, A. Fischer, M. S. G. Ahlquist and L. Sun, *Inorg. Chem*. **2012**, *51*, 3388; k) F. Li, Y. Jiang, B. Zhang, F. Huang, Y. Gao and L. Sun, *Angew. Chem. Int. Ed.* **2012**, *51*, 2417; l) L. Duan, C. M. Araujo, M. S. G. Ahlquist and L. Sun, *Proc. Natl. Acad. Sci. USA* **2012**, *109*, 15584; m) L. Duan, F. Bozoglian, S. Mandal, B. Stewart, T. Privalov, A. Llobet and L. Sun, *Nat. Chem*. **2012**, *4* 418; n) L. Tong, M. Göthelid and L. Sun, *Chem. Commun*. **2012**, *48*, 10025; o) L. Wang, L. Duan, B. Stewart, M. Pu, J. Liu, T. Privalov and L. Sun, *J. Am. Chem. Soc*. **2012**, *134*, 18868; p) L. Duan, L. Wang, A. K. Inge, A. Fischer, X. Zhou and L. Sun, *Inorg. Chem*. **2013**, *52*, 7844; q) L. Tong, A. K. Inge, L. Duan, L. Wang, X. Zou and L. Sun, *Inorg. Chem.* **2013**, *52*, 2505; r) Y. Jiang, F. Li, F. Huang, B. Zhang and L. Sun, *Chin. J. Catal*. **2013**, *34*, 1489; s) R. Staehle, L. Tong, L. Wang, L. Duan, A. Fischer, M. S. G. Ahlquist and L. Sun, *Inorg. Chem.* **2014**, *53*, 1307.

12. a) D. J. Wasylenko, C. Ganesamoorthy, B. D. Koivisto, M. A. Henderson and C. P. Berlinguette, *Inorg. Chem.* **2010**, *49*, 2202; b) D. J. Wasylenko, C. Ganesamoorthy, M. A. Henderson, B. D. Koivisto, H. D. Osthoff and C. P. Berlinguette, *J. Am. Chem. Soc.* **2010**, *132*, 16094; c) D. J. Wasylenko, C. Ganesamoorthy, M. A. Henderson and C. P. Berlinguette, *Inorg. Chem.* **2011**, *50*, 3662.
13. a) J. L. Boyer, D. E. Polyansky, D. J. Szalda, R. Zong, R.P. Thummel and E. Fujita, *Angew. Chem. Int. Ed*. **2011**, *50*, 12600; b) D. E. Polyansky, J. T. Muckerman, J. Rochford, R. Zong, R. P. Thummel and E. Fujita, *J. Am. Chem. Soc.* **2011**, *133*, 14649; c) A. Lewandowska-Andralojc, D. E. Polyansky, R. Zong, R. P. Thummel and E. Fujita, *Phys. Chem. Chem. Phys.* **2013**, *15*, 14058; d) Y. M. Badiei, D. E. Polyansky, J. T. Muckerman, D. J. Szalda, R. Haberdar, R. Zong, R. P. Thummel and E. Fujita, *Inorg. Chem.* **2013**, *52*, 8845; e) J. T. Muckerman, M. Kowalzcyk, Y. M. Badiei, D. E. Polyansky, J. J. Concepcion, R. Zong, R. P. Thummel and E. Fujita, *Inorg. Chem*. **2014**, *53*, 6904.
14. a) M. D. Kärkäs, T Åkermark, E. V. Johnston, S. R. Karim, T. M. Laine, B.-L. Lee, T. Åkermark, T. Privalov and B. Åkermark, *Angew. Chem. Int. Ed*. **2012**, *51*, 11589; b) M. D. Kärkäs, T Åkermark, H. Chen, J. Sun and B. Åkermark, *Angew. Chem. Int. Ed*. **2013**, *52*, 4189.
15. a) X. Sala, M. Z. Ertem, L. Vigara, T. K. Todorova, W. Chen, R. C. Rocha, F. Aquilante, C. J. Cramer, L. Gagliardi and A. Llobet, *Angew. Chem. Int. Ed.* **2010**, *49*, 7745; b) L. Bernet, R. Lalrempuia, W. Ghattas, H. Mueller-Bunz, L. Vigara, A.

Llobet and M. Albrecht, *Chem. Commun.* **2011**, *47*, 8058; c) L. Vigara, M. Z. Ertem, N. Planas, F. Bozoglian, N. Leidel, H. Dau, M. Haumann, L. Gagliardi, C. J. Cramer and A. Llobet, *Chem. Sci.* **2012**, *3*, 2576; d) S. Roeser, P. Farràs, F. Bozoglian, M. Martínez-Belmonte, J. Benet-Buchholz and A. Llobet, *ChemSusChem.* **2011**, *4*, 197; e) S. Maji, I. López, F. Bozoglian, J. B.-Buchholz and A. Llobet, *Inorg. Chem*. **2013**, *52*, 3591; f) I. López, M. Z. Ertem, S. Maji, J. B.-Buchholz, A. Keidel, U. Kuhlmann, P. Hildebrandt, C. J. Cramer, V. S. Batista and A. Llobet, *Angew. Chem. Int. Ed*. **2014**, *53*, 205.

16. a) M. Yagi, A. Syouji, S. Yamada, M. Komi, H. Yamazaki and S. Tajima, *Photochem. Photobiol. Sci.* **2009**, *8*, 139; b) M. Yagi, S. Tajima, M. Komi and H. Yamazaki, *Dalton Trans.* **2011**, *40*, 3802; c) H. Yamazaki, T. Hakamata, M. Komi and M. Yagi, *J. Am. Chem. Soc.* **2011**, *133*, 8846; d) M. Hirahara, M. Z. Ertem, M. Komi, H. Yamazaki, C. J. Cramer and M. Yagi, *Inorg. Chem*. **2013**, *52*, 6354.
17. a) R. Zong and R. P. Thummel, *J. Am. Chem. Soc*. **2005**, *127*, 12802; b) H.-W. Tseng, R. Zong, J. T. Muckerman and R. P. Thummel, *Inorg. Chem*. **2008**, *47*, 1763; c) S. K. Padhi, R. Fukuda, M. Ehara and K. Tanaka, *Inorg. Chem*. **2012**, *51*, 5386; d) M. Vennampalli, G. Liang, C. E. Webster and X. Zhao, *Eur. J. Inorg. Chem.* **2014**, *4*, 715.
18. a) M. H. V. Huynh and T. J. Meyer, *Chem. Rev.* **2007**, *107*, 5004; b) J. J. Warren, T. A. Tronic and J. M. Mayer, *Chem. Rev*. **2010**, *110*, 6961.
19. K. J. Takeuchi, M. S. Thompson, D. W. Pipes and T. J. Meyer, *Inorg. Chem*. **1984**, *23*, 1845.
20. T. R. Weaver, S. A. Adeyemi, G. M. Brown, R. P. Eckberg, W. E. Hatfieid, E. C. Johnson, R. W. Murray, D. Untereker and T. J. Meyer, *J. Am. Chem. Soc.* **1975**, *97*, 3039.

Chapter 1

A mononuclear ruthenium complex showing multiple proton-coupled electron transfer toward multi-electron transfer reactions

Introduction

Proton-coupled electron transfer (PCET) is an important chemical process that involves the concerted transfer of a proton (H^+) and an electron (e^-).[1-5] It is widely employed to achieve multi-electron transfer reactions such as water oxidation by photosystem II[1] and nitrogen fixation by nitrogenase[2] as well as solar energy conversion in artificial photosynthesis,[3] since high-energy intermediates and/or electrostatic charge buildup during the reactions are generally avoided by going through PCET processes.[4] In order to understand and utilize the PCET reactions, a number of studies have been conducted experimentally and theoretically.[5]

Water-coordinated metal ions (M^{n+}-OH_2; see Scheme 1) are considered as one of the important modules for PCET reactions.[4a,5k] As the positive charge of the metal ion increases, the acidity of protons of the attached water molecule increases. As a result, it can afford a variety of protonation and oxidation states through proton transfer (PT), electron transfer (ET) and PCET reactions. Two electron oxidation of M^{n+}-OH_2 can afford a high-valent metal-oxo species ($M^{(n+2)+}$=O) via two-step PCET processes, which has been identified as the key intermediate in a variety of oxidation reactions.[6]

Along with extensive studies on water-coordinated metal ions,[4a,5k] organic modules for PCET reactions have also been investigated. One significant example of the organic PCET modules is imidazole, which is contained in the amino-acid residue of Histidine (His) and plays an important role in PCET reactions in biological systems.[7] In addition, 2,2'-biimidazole (H_2bim), regarded as a covalently-linked dimer of imidazole, has various protonation/oxidation states via PT, ET and PCET reactions, as shown in Scheme 2.[8] Since H_2bim serves as a bidentate ligand coordinating to a metal ion, metal-H_2bim complexes have also been investigated as modules for metal-mediated PCET reactions.[9]

In this context, metal complexes bearing both a coordinated water molecule and an organic PCET module are expected not only to afford a rich acid-base and redox

chemistry based on a variety of protonation/oxidation states, but also to serve as catalysts for various multi-electron transfer reactions. However, in spite of many investigations, there have been only a few reports on metal complexes bearing both a coordinated water molecule and an organic PCET module.[10] In particular, conscious efforts to utilize such metal complexes for multi-electron transfer reactions have yet to be made. The acid-base and redox properties and reactivity for multi-electron transfer reactions of such complexes have to be clarified.

This chapter describes the synthesis and structures of new ruthenium complexes with an H_2bim ligand, [Ru(trpy)(H_2bim)Cl]PF_6 (**1**) and [Ru(trpy)(H_2bim)(OH_2)]$(PF_6)_2$ (**2**) (trpy = 2,2':6',2"-terpyridine) (Scheme 3). The detailed analyses on the acid-base and redox properties of **2** revealed that **2** demonstrates four-step PCET reactions to give the four-electron oxidized species, $[Ru^{IV}(trpy)(bim)(O)]^{2+}$, without electrostatic charge buildup during the reactions.

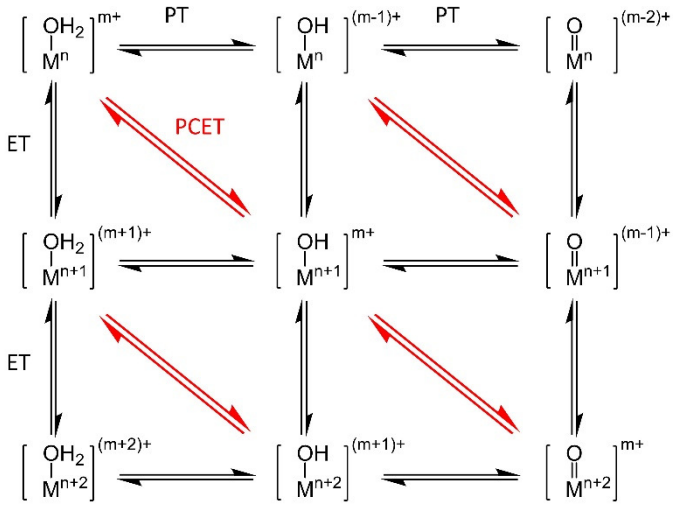

Scheme 1. Square diagram for proton transfer (PT), electron transfer (ET) and proton-coupled electron transfer (PCET) reactions of a water-coordinated metal ion (M^{n+}– OH_2).

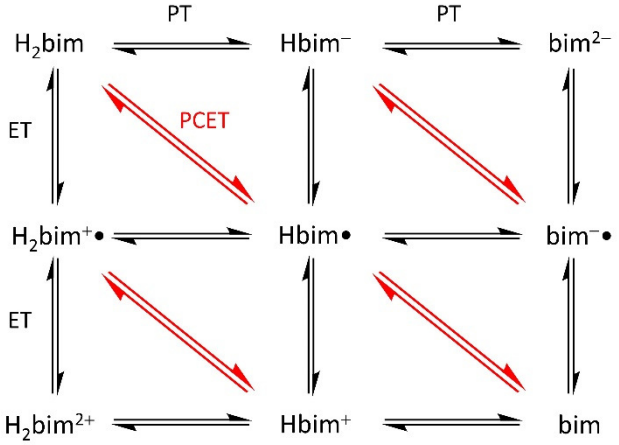

Scheme 2. Square diagram for PT, ET and PCET reactions of 2,2'-biimidazole (H_2bim).

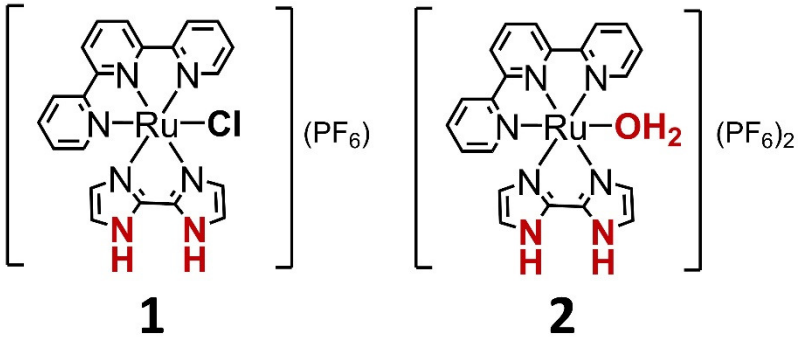

1 **2**

Scheme 3. Structures of [Ru(trpy)(H_2bim)Cl]PF_6 (**1**) and [Ru(trpy)(H_2bim)(OH_2)]-(PF_6)$_2$ (**2**).

Experimental section

Materials.

LiCl, $NaPF_6$ and $AgNO_3$ were purchased from Wako Pure Chemical Industries, Ltd. All solvents and reagents were of the highest quality available and were used as received. Ru(trpy)Cl_3 (trpy = 2,2':6',2''-terpyridine)[11] and H_2bim (2,2'-biimidazole)[12] were prepared by the literature methods.

Measurements.

UV-visible absorption spectra were recorded on a Shimadzu UV-2450SIM UV/Visible spectrophotometer. Elemental analyses were carried out on a Yanagimoto MT-5 elemental analyzer. ESI-TOF mass spectra were recorded on a JEOL JMS-T100LC mass spectrometer. All the ESI-TOF mass spectrometric measurements were recorded in the positive ion mode at a cone voltage of 25 V. ^{1}H NMR spectra were acquired on a Bruker DRX600 spectrometer, where chemical shifts in CD_3CN were referenced to internal tetramethylsilane. Square-wave and cyclic voltammograms were recorded on a BAS ALS Model 650DKMP electrochemical analyzer. The measurements were carried out in argon-purged aqueous solution using a glassy carbon disk working electrode, a Pt wire counter electrode, and a saturated calomel electrode (0.241 V *vs*. NHE).

Synthesis.

[Ru(trpy)(H_2bim)Cl]PF_6 (1). Ru(trpy)Cl_3 (451 mg, 1 mmol), 2,2'-biimidazole (189 mg, 1.4 mmol), and LiCl (108 mg, 2.5 mmol) were mixed in a methanol (200 mL) and the reaction mixture was refluxed for 8 h. After the solution was cooled down to room temperature, the insoluble materials were removed by filtration. A water (15 mL) was added to the filtrate and the methanol was evaporated under reduced pressure. A saturated $NaPF_6$ solution added to the solution and kept in the refrigerator, resulted in the precipitate of the complex. The solid was collected by filtration, washed with water and diethyl ether, and dried in vacuo. The crude product was further purified by gel permeation chromatography (Sephadex LH-20) using an acetonitrile/methanol (1:1) mixture as the eluent. Yield 397 mg (0.61 mmol, 61.5 %). ^{1}H NMR (600 MHz, CD_3CN): δ = 8.40 (d, 2H, J = 8.0 Hz), 8.31 (d, 2H, J = 8.0 Hz), 8.07 (d, 1H, J = 1.3 Hz), 7.91 (t, 1 H, J = 7.9 Hz), 7.87 (d, 2 H, J = 5.0), 7.83 (t, 2H, J = 7.8 Hz), 7.74(d, 1H, J = 1.3 Hz), 7.33(t, 1H, J = 6.5 Hz), 6.82 (d, 1H, J = 1.5 Hz), 5.82 (d, 1H, J = 1.9 Hz). ESI-TOF MS (positive ion, acetonitrile): m/z 504 ([Ru^{II}(trpy)(H_2bim)Cl]$^+$). Elemental analysis: $C_{21}H_{17}ClF_6N_7PRu$: C 38.87, H 2.64, N 15.11. Found: C 38.75, H 2.71, N 15.17. Single crystals suitable for X-

ray crystallography were grown by the slow diffusion of diethyl ether into an acetonitrile solution of **1**.

[Ru(trpy)(H_2bim)(OH_2)](PF_6)$_2$ (2). A solution of **1** (32.5 mg, 0.05 mmol) and $AgNO_3$ (91 mg, 0.05 mmol) were stirred at r.t. in an acetone/water mixture (3:1 (v/v), 8 mL) for 4 h under argon in the dark. The precipitated AgCl was removed by filtration and the filtrate was evaporated under reduced pressure to remove the acetone. The solution was filtered and an aqueous saturated $NaPF_6$ was added to the solution. The brown solid was collected by filtration, and dried in vacuo. Yield 34.5 mg (0.042 mmol, 85 %). ^{1}H NMR (600 MHz, CD_3CN): δ = 8.43 (d, 2H, *J* = 8.1 Hz), 8.33 (d, 2H, *J* = 8.0 Hz), 8.11 (t, 1H, *J* = 8.1 Hz), 7.93 (t, 2 H, *J* = 7.9 Hz), 7.87(d, 2H, *J* = 5.3 Hz), 7.86 (s, 1H), 7.65 (s, 1H), 7.38 (t, 2H, *J* = 6.5 Hz), 6.80 (s, 1H), 5.76 (s, 1H). ESI-TOF MS (positive ion, acetonitrile): m/z 255 ([Ru^{II}(trpy)(H_2bim)CH_3CN]$^{2+}$), m/z 248.5 ([Ru^{II}(trpy)-(H_2bim)N_2]$^{2+}$), m/z 509 ([Ru^{II}(trpy)(Hbim)CH_3CN]$^{+}$),. Elemental analysis: $C_{21}H_{23}F_{12}N_7O_3P_2Ru$: C 31.04, H 2.85, N 12.07. Found: C 31.08, H 2.63, N 12.06. Single crystals suitable for X-ray crystallography of [Ru(trpy)(H_2bim)(OH_2)](BF_4)$_2$ (**2'**) were grown by the slow evaporation of acetone in an acetone/water mixed solution of **2** containing excess amount of $NaBF_4$.

X-ray crystallography.

Crystal of **1** was mounted on glass fiber using paraton oil and immediately cooled to 100 K in a cold stream of nitrogen. Diffraction data were measured on a Bruker SMART APEXII ULTRA CCD-detector diffractometer. Graphite-monochromated Mo-Kα radiation (λ = 0.71073 Å) was used. Cell parameters were retrieved using the *APEX2*[13] software and refined using *SAINT*[14] on all observed reflections. Data reduction was performed using the *SAINT* software. Absorption corrections were applied using *SADABS*.[15] The structure was solved by direct methods using *SHELXS-97*[16] and refined on F^2 by the full matrix least-squares techniques with *SHELXL-97* program.[16] All non-hydrogen atoms were refined anisotropically. Molecular graphics were generated using *ORTEP-3 for Windows*[17a] and *POV-RAY*.[17b]

Crystal of **2'** was mounted in a loop. Diffraction data at 123 K were measured on a Rigaku AFC8 diffractometer using a Rigaku Saturn CCD system. Graphite-monochromated Mo-Kα radiation (0.71075 Å) was used. Cell parameters were retrieved using Crystal Clear-SM 1.4.0 software and refined using Crystal Clear-SM 1.4.0 on all observed reflections. Data reduction and empirical absorption correction using equivalent reflections and

Lorentzian polarization were performed with the program Crystal Clear-SM 1.4.0. The structure was solved by direct method using *SIR-92*[55] and refined on F^2 by the full-matrix least squares techniques with *SHELXL-97*.[16] All non-hydrogen atoms were refined anisotropically. Molecular graphics were generated using *ORTEP-3 for Windows*[17a] and *POV-RAY*.[17b]

DFT calculations.

Calculations were carried out using the DFT method implemented in the Gaussian 03 package of programs.[18] The structures were fully optimized using the B3LYP which uses hybrid Becke's three-parameter exchange functional[19] with the correlation energy functional of Lee, Yang, and Parr.[20] All the calculations were performed using the standard double-ζ type LanL2DZ basis set[21] implemented in Gaussian 03, without adding any extra polarization or diffuse function. The LanL2DZ basis set also uses relativistic effective core potentials (RECP) for the Ru atom to account for the scalar relativistic effects of the inner 28 core electrons ($[Ar]3d^{10}$) for Ru. All the calculations were performed using the polarizable continuum model (PCM)[22] to compute the structures in aqueous media. All the stationary points were characterized by their harmonic vibrational frequencies as minima. The exited states were calculated by the TD-DFT[23] method within the Tamm-Dancoff approximation as implemented in Gaussian 03. These calculations employ the hybrid B3LYP functional along with the basis sets described above. At least 300 excited states were computed in each calculation. To obtain the simulated spectrum of each species, transition energies and oscillator strengths have been interpolated by a Gaussian convolution with a common σ value of 0.2 eV.

Crystal Structures

The molecular structures of $[Ru(trpy)(H_2bim)Cl]PF_6$ (**1**) and $[Ru(trpy)(H_2bim)(OH_2)](BF_4)_2$ (**2'**) were determined by X-ray crystallographic investigation. An ORTEP drawing of the cationic moiety of **1** is shown in Figure. 1a, and selected bond distances and angles are also presented in Table 2. **1** crystallizes with one independent Ru complex and two PF_6 anions in the asymmetric unit of the tetragonal $P4_1$ crystal. The crystal structure shows that the three pyridyl rings of the trpy ligand are nearly coplanar, as are the two imidazolyl rings of H_2bim. The two ligands are coordinated to the metal ion through their nitrogen atoms in a mutually perpendicular fashion. The complex has a distorted-octahedral geometry at ruthenium atom where three nitrogen atoms of the trpy ring and one nitrogen atom N5 of the H_2bim ring form the equatorial base. The remaining nitrogen atom N4 of the H_2bim ring and the chlorine atom are in the axial position with the Ru1-Cl distance of 2.416(1) Å, which is slightly longer than that of 2,2'-bipyridine analogue ($[Ru(trpy)(bpy)Cl]^+$ (2.3969(7) Å)[24], indicating that the stronger electron donating ability of the nitrogen atoms of H_2bim than those of bpy. The average bond distance between the Ru atom and each nitrogen atom N1, N2, or N3 of the tpy ligand is 2.014 Å with the middle nitrogen atom N2 and the metal ion distance being the shortest (1.936(3) Å). On the other hand, the average bond distance between the Ru atom and each nitrogen atom N4 or N5 of the H_2bim ligand is 2.086 Å, which is longer than that of the tpy ligand. The bond angles of 80.4(1)° formed by two nitrogen atoms of the tpy ring and the Ru atom is slightly larger than that formed by the Ru atom and two nitrogen atoms of the H_2bim ring in the cis position (78.6(1)°).

The corresponding aqua complex was crystallized as BF_4 salt, $[Ru(trpy)(H_2bim)(OH_2)](BF_4)_2$ (**2'**), which was obtained the slow evaporation of acetone in an acetone/water mixed solution of **2** containing excess amount of $NaBF_4$. An ORTEP drawing of the cationic moiety shown in Fig. 1b is basically similar to that of **1** except for the coordination of an aqua ligand instead of a chloro anion. Selected bond distances and angles are listed in Table 3. **2'** crystallizes with one independent Ru complex and two BF_4 anions in the asymmetric unit of the monoclinic $P2_1/a$ crystal. Two ligands are coordinated to the Ru atom in a mutually perpendicular manner, which provides a distorted octahedral environment, as is the case for **1**. The bond distance between the Ru atom and the oxygen atom of the axial aqua ligand is 2.133(3) Å, which is longer than that found in $[Ru(trpy)(bpy)(OH_2)]^{2+}$ (2.097(6) Å)[25], indicating that the stronger electron donating ability of the nitrogen atoms of H_2bim than those of bpy.

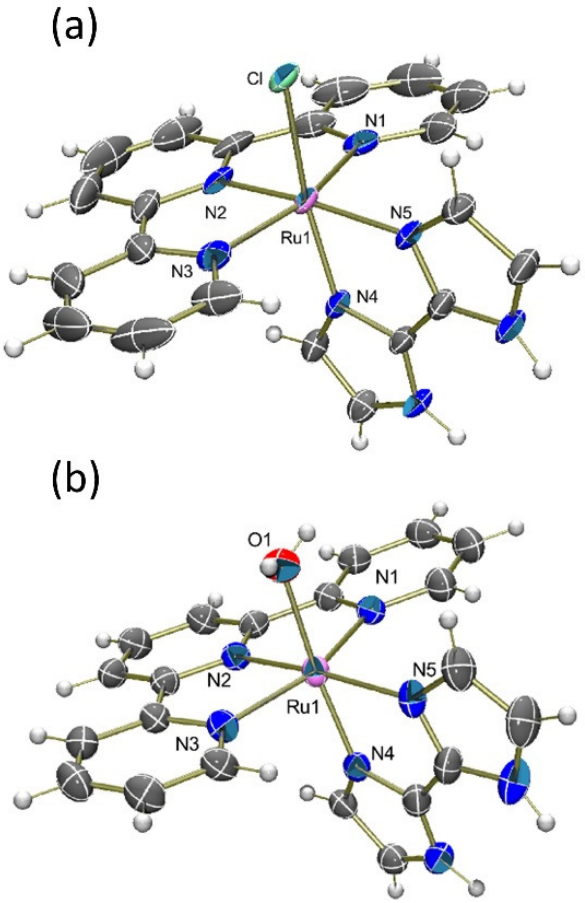

Figure 1. ORTEP drawings of the cationic moieties of (a) **1** and (b) **2'** (50% probability ellipsoids).

The H_2bim and M-OH_2 moieties in **1** and **2'** serve as proton donors in hydrogen bonding, as expected from their proton dissociable character (Schemes 1 and 2). In the crystal structure of **1**, H_2bim indeed interacts with the Cl ligand from the neighboring complex via two hydrogen bonds (Fig. 2), where the N···Cl separations are 3.150(4) and 3.243(4) Å for N7-Cl and N6-Cl, respectively (Table 2). Therefore, the cationic moiety of **1** has both proton donating (H_2bim) and proton accepting (Cl) sites, thus forming a one-dimensional hydrogen-bonded infinite chain along c axis. The PF_6 anions are contained to maintain charge balance of the structure with no hydrogen bond interaction. In the case of **2'**, there are two types of hydrogen donors, H_2bim and M-OH_2. H_2bim is hydrogen-bonded with a BF_4 anion via two N-H···F interactions, where the N···F separations are 2.791(5) and 2.822(6) Å for N7-F7 and N6-F8, respectively (Table 3 and Fig. 3). Meanwhile the Ru-OH_2 site acts as a proton donor for the hydrogen bonds with

BF_4 anions, forming a hydrogen-bonded supramolecular dimer. The proton-donating character of H_2bim in crystalline solids has been reported in many literatures so far.[26]

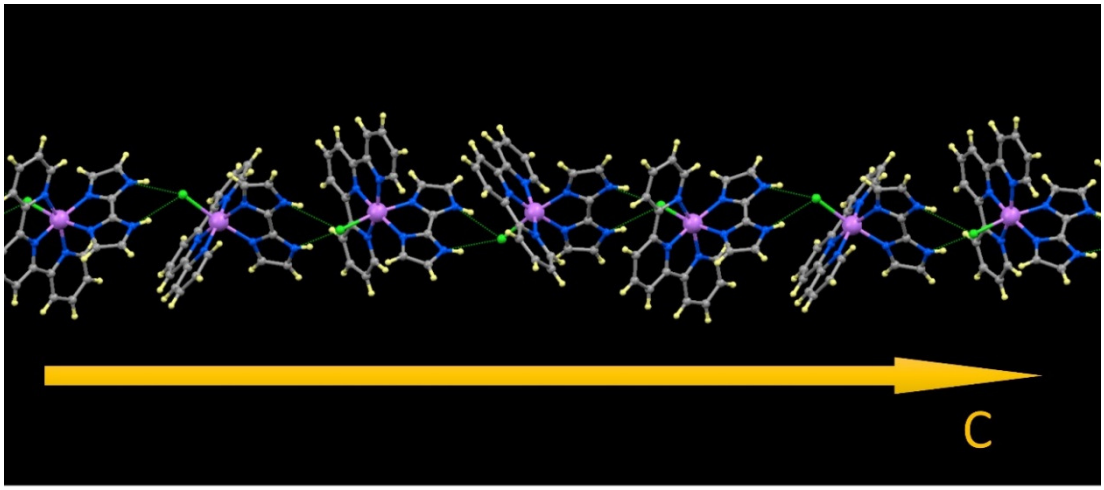

Figure 2. Hydrogen-bonded one-dimensional network of the cationic moieties of **1** in the crystal.

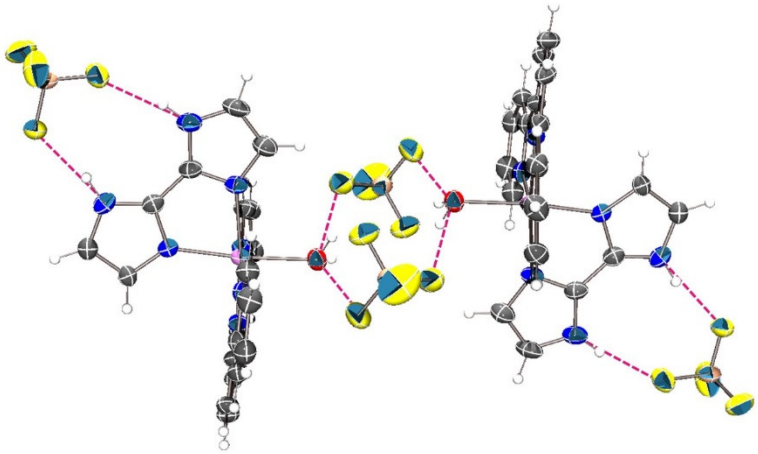

Figure 3. Hydrogen-bonded dimeric structure of the complex **2'** in the crystal. Thermal ellipsoids are displayed at the 50% probability level.

Table 2. Selected bond distances (Å) and angles (°) for **1**.

Ru1-Cl	2.416(1)	Ru1-N1	2.055(3)
Ru1-N2	1.936(3)	Ru1-N3	2.051(3)
Ru1-N4	2.069(3)	Ru1-N5	2.104(4)
N3-Ru1-N2	80.4(1)	N2-Ru1-N1	80.4(1)
N5-Ru1-N4	78.6(1)		
N6···Cl^{i}	3.243(4)	N7···Cl^{i}	3.150(4)

Symmetry codes: (i) -y, x, z+0.25

Table 3. Selected bond distances (Å) and angles (°) for **2'**.

Ru1-O1	2.134(3)	Ru1-N1	2.053(4)
Ru1-N2	1.940(3)	Ru1-N3	2.076(4)
Ru1-N4	2.041(3)	Ru1-N5	2.113(3)
N3-Ru1-N2	79.9(1)	N2-Ru1-N1	80.0(2)
N5-Ru1-N4	78.0(1)		
O1···F2^{i}	2.915(6)	O1···F4^{ii}	2.699(6)
N6···F8^{iii}	2.822(6)	N7···F7^{iv}	2.791(5)

Symmetry codes: (i) 2-x, -y, 1-z; (ii) x, y, 1+z; (iii) 0.5-x, y-0.5, 1-z.
(iv) 0.5-x, y-0.5, 1-z

UV-visible absorption spectra

UV-visible absorption spectra of the complex **2** were measured in the various pH buffer solutions (Figs. 4 and 5). In any pH conditions, the complex displays intense absorption bands in the UV region that were assigned to ligand-based π–π* transitions. Additionally, two moderately intense bands were observed in the visible region. These bands are assigned to the metal-to-ligand charge transfer (MLCT) transition from dπ orbital of Ru to π* orbitals of trpy and H_2bim.

The pH dependence of the MLCT bands in the visible region is considered from a standpoint of protonation/deprotonation of **2** (see Figure. 4). The measurements of the solutions with pH 0–8 shows an absorption band centered at 476 nm ($\varepsilon = 5.7\times10^3$ M^{-1} cm^{-1}) and an absorption shoulder around 360 nm (ε = *ca.* 6.0×10^3 M^{-1} cm^{-1}). These spectra are assigned to the totally protonated form of **2**. As the pH increases to 10.0, a band at 496 nm ($\varepsilon = 5.5\times10^3$ M^{-1} cm^{-1}) and a shoulder around 390 nm (ε = *ca.* 4.5×10^3 $M^{-1}cm^{-1}$) grow up with clear isosbestic points (λ = 377 and 421 nm, Fig. 5). Further increase of the pH results in the appearance of the new absorption bands at 401 nm (ε = ca. 5.0×10^3 M^{-1} cm^{-1}) and 536 nm ($\varepsilon = 3.6\times10^3$ $M^{-1}cm^{-1}$) with new isosbestic points (451 nm, Fig. 5). The absorbances at 421 nm and 451 nm, which are isosbestic points for the first and second deprotonations, respectively, were plotted against pH to determine pK_{a1} = 9.0 and pK_{a2} = 11.3 (Fig. 5b and 5d). These stepwise spectral changes with the isosbestic points indicate two-step clean interconversions between the protonated and mono-deprotonated forms, and mono-deprotonated and di-deprotonated forms of **2**.

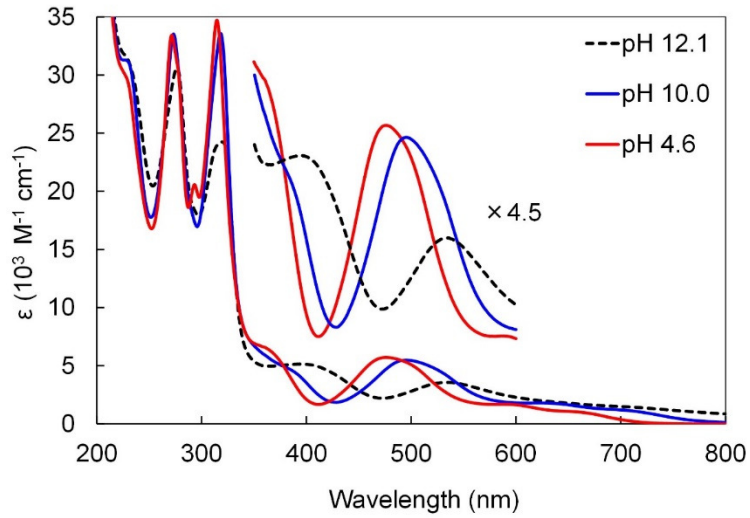

Figure 4. UV-visible absorption spectra **2** (0.5 mM) in different pH buffer solutions. The pH values were controlled with Britton Robinson buffer (citric acid + boric acid + phosphoric acid) and adjusted with NaOH and H_2SO_4.

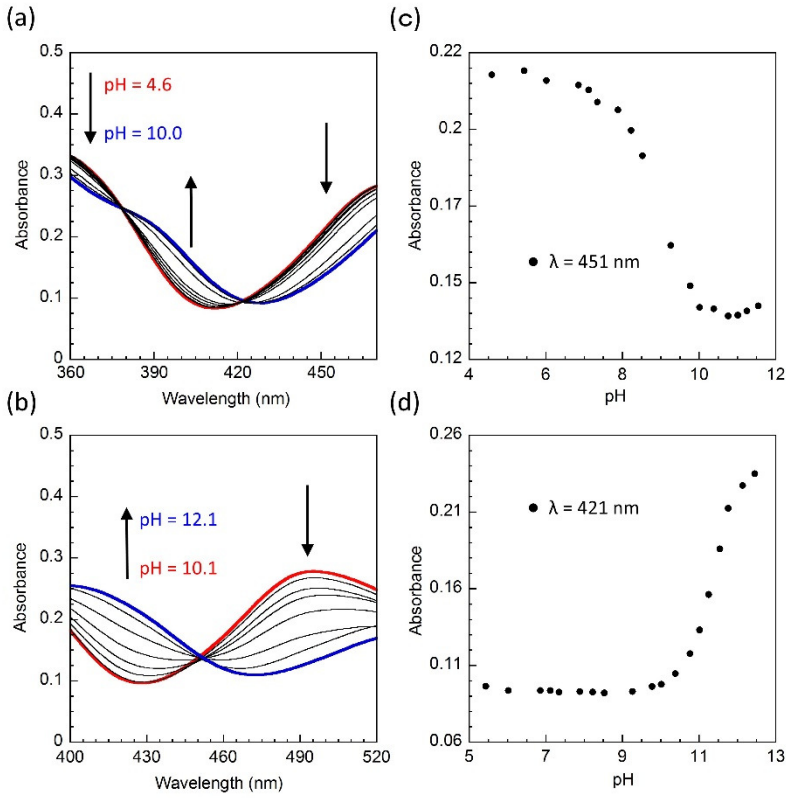

Figure 5. Absorption spectra of aqueous solutions of **2** (0.5 mM) in buffer solution at (a) pH 4.6 – 10.0 and (b) pH 10.1 – 12.1. The dependences of the absorbance at (c) 451 nm and (d) 421 nm on pH.

Deprotonation from **2** affords two different isomers, $[Ru(trpy)(Hbim)(OH_2)]^+$ and $[Ru(trpy)(H_2bim)(OH)]^+$, which are probably in equilibrium in an aqueous solution with pH between pK_{a1} and pK_{a2}. The dominant species in the equilibrium was determined by the comparison with reported pK_a values of analogous Ru complexes with M-OH_2[27-30] or H_2bim[9b,31] moieties, which are listed in Table 4. As a rough guess, the first pK_a values of Ru(H_2bim) complexes (pK_a ~ 7) are smaller than those of Ru-OH_2 complexes (pK_a ~ 10), implying that the H_2bim moiety of **2** is more acidic than the M-OH_2 moiety. Moreover, as discussed above (see Crystal Structures section), the nitrogen atoms of H_2bim have stronger electron-donating characters than those of bpy, 2,2'-bipyrimidine (bpm) and 1,10-phenanthroline (phen), thus suggesting that the pK_a value of the Ru-OH_2 moiety of **2** should be larger than those of $[Ru(trpy)(bpy)(OH_2)]^{2+}$ (pK_a = 9.7),[27] $[Ru(trpy)(bpm)(OH_2)]^{2+}$ (pK_a = 9.7),[28] and $[Ru(trpy)(phen)(OH_2)]^{2+}$ (pK_a = 9.6).[29] Therefore, it is reasonable to support that the dominant form of the mono-deprotonated species of **2** is assigned to $[Ru(trpy)(Hbim)(OH_2)]^+$ rather than $[Ru(trpy)(H_2bim)(OH)]^+$.

The next step of deprotonation from $[Ru(trpy)(Hbim)(OH_2)]^+$ appears to be associated with the M-OH_2 moiety, by considering the difference of the two pK_a values ($\Delta pK_a = pK_{a2} - pK_{a1}$). The ΔpK_a values of the reported Ru(H_2bim) complexes[9b,31] are more than 4, as listed in Table 4. If the second deprotonation occurs at the Hbim moiety of the mono-deprotonated form $[Ru(trpy)(Hbim)(OH_2)]^+$, pK_{a2} of **2** is expected to be more than 13. Taking into consideration the ΔpK_a value of **2** ($\Delta pK_a = 2.3$), the next step of deprotonation from $[Ru(trpy)(Hbim)(OH_2)]^+$ appears to be from the M-OH_2 moiety, thus affording $[Ru(trpy)(Hbim)(OH)]^0$. These assignments of the two-step dissociations of protons are also supported by DFT calculations, as discussed below.

The stepwise red shifts of the MLCT transitions on deprotonations can be attributed to the destabilization of metal orbitals due to an increase in the negative charge on the ligand and a decrease in the effective positive charge on the metal. Degree of the red shift that occurs on the first deprotonation ($\Delta\lambda_{max}$ ~ 20 nm) is smaller than that on the second deprotonation ($\Delta\lambda_{max}$ ~ 40 nm). This is because the destabilization of the metal orbitals is more strongly influenced by the second deprotonation (-OH_2 to -OH) than the first one (H_2bim to Hbim). This result is also supported by DFT calculations, as discussed below.

It is also noted that the chloro complex **1** easily undergoes hydrolysis after the dissolution in an aqueous media to afford the equilibrium mixture of **1** and the aqua complex **2**, which prevents us to examine pH-dependence properties of **1** in aqueous media. The absorption maximum of the aqueous solution gradually shifts from 487 nm to 477 nm after dissolution of **1** in water (Fig. 6), where the latter is very close to that of **2** at pH 0-8 (476 nm, Fig. 4). UV-visible absorption spectrum for **1** (0.5 mM) in an

acetonitrile solution (Fig. 7) exhibits two MLCT transition from dπ orbital of Ru to π* orbitals of trpy and H_2bim in the visible region. The two MLCT bands are red shifted compared with those for **2** at pH 0-8 because of the negative charge of coordinated Cl^- anion.

Table 4. The pK_a values of Ru complexes with H_2bim and M–OH_2 moieties (bpm = 2,2'-bipyrimidine, phen = 1,10-phenanthroline, tmtacn = 1,4,7-trimethyl-1,4,7-triazacyclononane, acac = acetylacetone).

Complex	pK_{a1}	pK_{a2}	Ref.
$[Ru(trpy)(H_2bim)(OH_2)]^{2+}$ (**2**)	9.0	11.3	This work
$[Ru(trpy)(bpy)(OH_2)]^{2+}$	9.7	-	27
$[Ru(trpy)(bpm)(OH_2)]^{2+}$	9.7	-	28
$[Ru(trpy)(phen)(OH_2)]^{2+}$	9.6	-	29
$[Ru(tmtacn)(bpy)(OH_2)]^{2+}$	11.8	-	30
$[Ru(bpy)_2(H_2bim)(OH_2)]^{2+}$	7.2	12.1	9b
$[Ru(acac)_2(H_2bim)(OH_2)]^{2+}$	6.8	11.0	31

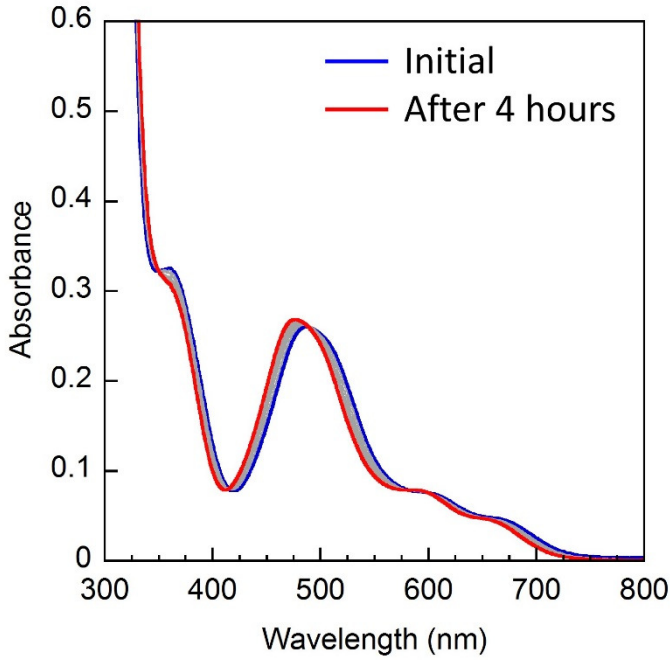

Figure 6. Time course of absorption spectra after dissolution of **1** (0.5 mM) in water.

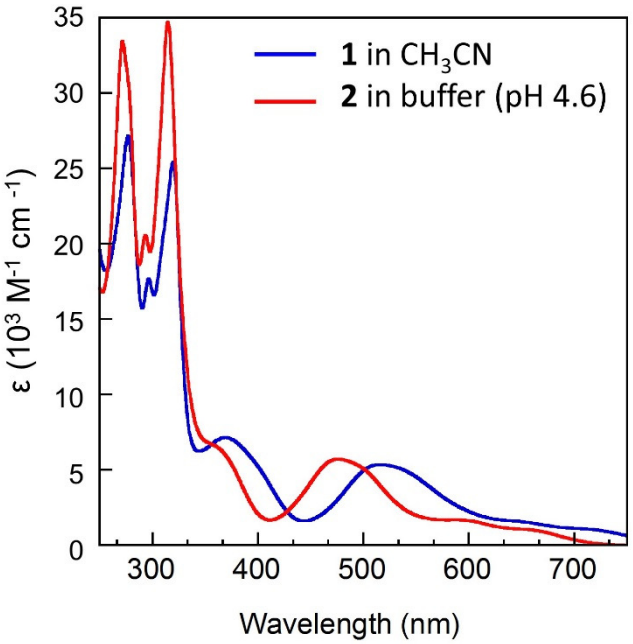

Figure 7. UV-visible spectrum of an acetonitrile solution of **1** (0.5 mM) and a buffer solution of **2** (0.5 mM, at pH 4.6).

DFT Calculations

In order to discuss the electronic structures of $[Ru(trpy)(H_2bim)(OH_2)]^{2+}$ and its deprotonated forms, density functional theory (DFT) and time-dependent density functional theory (TD-DFT) calculations were carried out. All calculations were performed with the polarizable continuum model (PCM) to account for solvent effects in aqueous media.

The optimized structure for $[Ru(trpy)(H_2bim)(OH_2)]^{2+}$ are similar to the X-ray crystal structure. For example, the calculated Ru-O bond distance is 2.167 Å, which are comparable to the experimental value (2.133(3) Å). Figure 8 depicts the frontier MO surfaces of $[Ru(trpy)(H_2bim)(OH_2)]^{2+}$. The highest occupied molecular orbitals (HOMOs, HOMO to HOMO-3) contain t_{2g} (d_{xy}, d_{xz}, and d_{yz}) character of d(Ru) with π-back donation to π* orbitals of H_2bim and trpy, while the lowest unoccupied molecular orbitals (LUMOs, LUMO to LUMO+5) are dominated by π* orbitals of H_2bim and trpy.

The electronic transitions for the calculated complexes have been investigated by the TD-DFT method. Calculated excitation wavelengths and oscillator strengths for selected transitions are listed in Table 5 and absorption spectra constructed by convolution of these calculated transitions with Gaussian functions are depicted in Figure 9. The profiles of the convoluted absorption spectra are similar to those observed experimentally, i.e., two moderately intense absorption bands around 350 and 450 nm. From the results of TD-DFT calculation, it can be concluded that the lower-energy transition around 450 nm mainly arises from the MLCT transition from dπ orbitals of Ru to π* orbitals of and trpy, and the higher-energy transition around 350 nm originates from the MLCT transition to π* orbitals of H_2bim (see Table 5).

The $[Ru(trpy)(H_2bim)(OH_2)]^{2+}$ cation has two types of proton dissociative sites, and therefore can afford two types of conjugate bases, $[Ru(trpy)(Hbim)(OH_2)]^{+}$ and $[Ru(trpy)(H_2bim)(OH)]^{+}$, relative energies of which were estimated by DFT calculations. It can be seen that the $[Ru(trpy)(Hbim)(OH_2)]^{+}$ form is more stable than the $[Ru(trpy)(H_2bim)(OH)]^{+}$ form, and the energy difference is 10.7 kJ/mol, consistent with the discussion in the above section. Moreover, the TD-DFT calculated absorption spectra and oscillator strengths of the $[Ru(trpy)(Hbim)(OH_2)]^{+}$ form (Table 5 and Fig. 9) provide further evidence to support the conclusion that the $[Ru(trpy)(Hbim)(OH_2)]^{+}$ form predominates in solution with pH between pK_{a1} and pK_{a2}; the calculated absorption maxima (475 and 371 nm) are very close to the experimental value for the mono-deprotonated form (496 and ca. 390 nm).

As suggested in the UV-Visible Absorption Spectra section, the dominant species of the di-deprotonated form is $[Ru(trpy)\text{-}(Hbim)(OH)]^{0}$. Indeed, the calculation for

[Ru(trpy)(Hbim)-(OH)]^0 afforded an energy much lower (by 21.6 kJ/mol) than that for [Ru(trpy)(bim)(OH_2)]^0. Moreover, the TD-DFT calculation for [Ru(trpy)(Hbim)(OH)]^0 also suggests the calculated profiles of the absorption spectra (Fig. 9) are similar to that observed experimentally (Fig. 4).

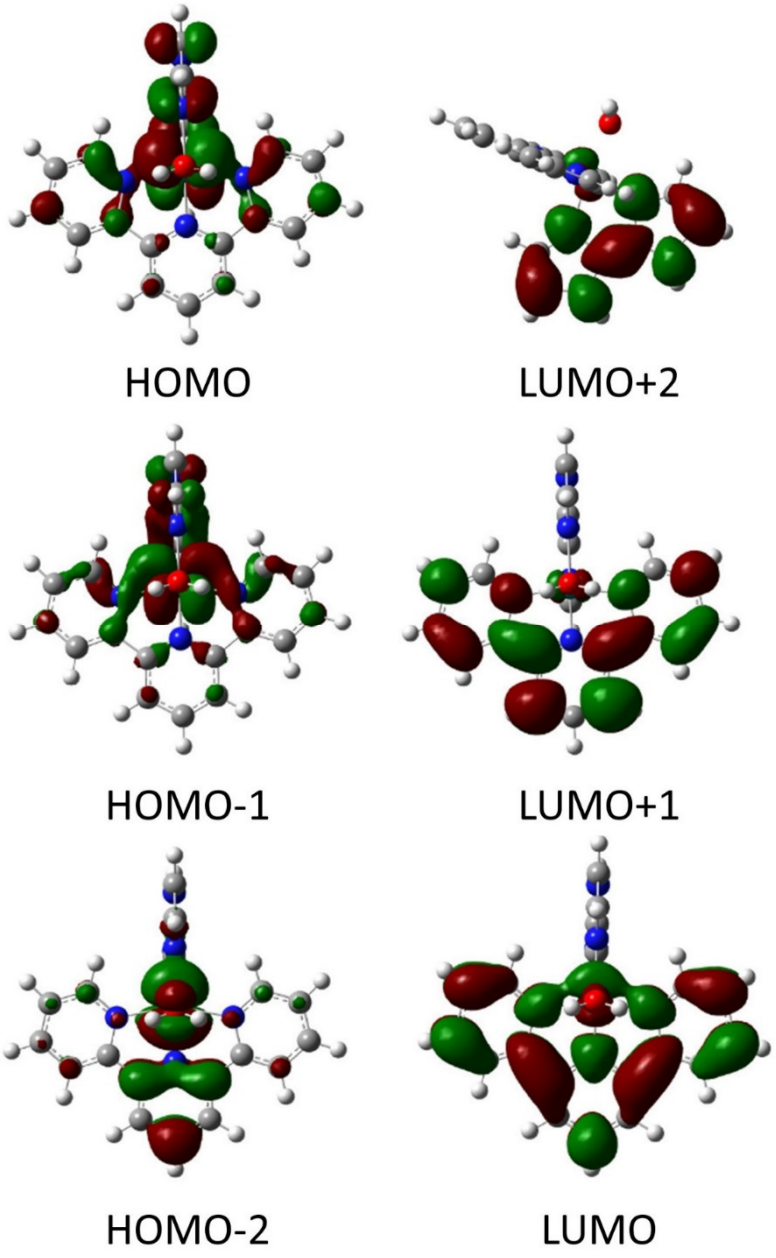

Figure 8. Isodensity surface plots of selected frontier molecular orbitals of **2** based on the optimized ground-state geometry.

Table 5. Wavelength and oscillator strengths of both isomers at MLCT band from TD-DFT calculated absorption spectra.

Complex	Wavelength (nm)	Oscillator strength	Transition	|CI coef| (> 0.3)
$[Ru(trpy)(H_2bim)(OH_2)]^{2+}$	466	0.0469	HOMO-2→LUMO+1	0.68751
	442	0.0912	HOMO-2→LUMO	0.34681
			HOMO-1→LUMO+1	0.39629
			HOMO→LUMO+1	0.36473
	364	0.0606	HOMO-1→LUMO+2	0.42111
			HOMO→LUMO+4	0.39707
$[Ru(trpy)(Hbim)(OH_2)]^{+}$	500	0.0486	HOMO-2→LUMO+1	0.68547
	477	0.0652	HOMO-2→LUMO	0.44248
			HOMO→LUMO+1	0.33187
	389	0.0381	HOMO→LUMO+2	0.65208
$[Ru(trpy)(Hbim)(OH)]^{0}$	660	0.056	HOMO→LUMO+1	0.60367
	414	0.117	HOMO-1→LUMO+2	0.66706

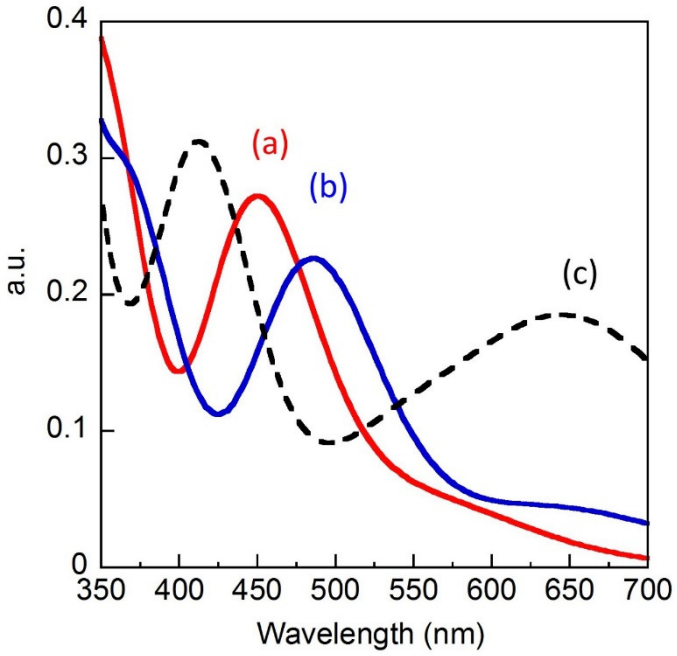

Figure 9. Calculated absorption spectra of (a) $[Ru(trpy)(H_2bim)(OH_2)]^{2+}$, (b) $[Ru(trpy)(Hbim)(OH_2)]^{+}$ and (c) $[Ru(trpy)(Hbim)(OH)]^{0}$.

Electrochemical properties

Square wave voltammograms (SWV) of **2** were examined in various pH conditions under an argon atmosphere (Fig. 10). The SWVs in any pH conditions show one oxidation peak and following two or three smaller peaks, which are shifted to a positive direction with decreasing pH (Fig. 10).

The first oxidation process starting from the Ru(II) complex is ascribed to the Ru(III)/Ru(II) redox couple. In all the pH range investigated (1 < pH < 12), the potentials of the Ru(III)/Ru(II) couples of **2** are largely shifted to the lower potential compared with 2,2'-bipyridine analogue $[Ru(trpy)(bpy)(OH_2)]^{2+}$, *e.g.* $E_{1/2}$ = 0.53 V for **2** and 0.81 V for $[Ru(trpy)(bpy)(OH_2)]^{2+}$ in acidic solution (pH = 1) This is due to the stronger-donating character of the H_2bim ligand, consistent with the results of X-ray crystallographic analysis.

Figure. 11 illustrates the potential versus pH (Pourbaix) diagram for **2** in the range of 1 < pH < 12 in water. According to the Nernst equation,[32] the slope in this diagram is equivalent to –(m/n)0.059 V/pH, where m and n represent the number of protons and electrons transferred, respectively.

$$\mathrm{Ox} + \mathrm{mH^+} + \mathrm{ne^-} \rightleftharpoons \mathrm{Red}$$

$$E_{1/2} = E^{o\prime} - \frac{\mathrm{m}}{\mathrm{n}} 0.059\mathrm{pH}$$

For example, when the potential is independent of pH (slope = 0 mV/pH), no proton is coupled in the one-electron redox process. On the other hand, when the potential decreases with increasing pH with a slope of –59 and –118 mV/pH, one and two protons are coupled with the one-electron redox process, respectively.

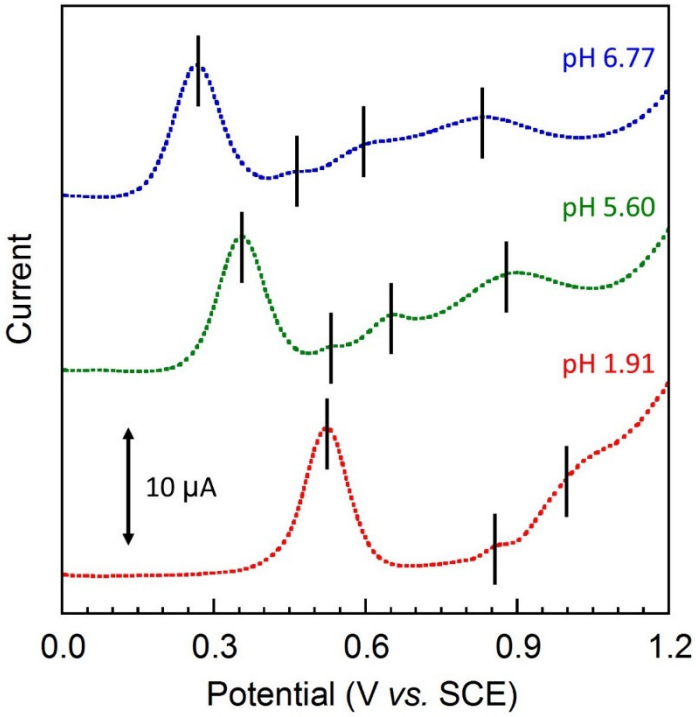

Figure 10. Square wave voltammograms of **2** (0.5 mM) in an aqueous solution under various pH conditions (pH values were adjusted with NaOH and H_2SO_4) (WE: GC; CE: Pt wire; RE: SCE; scan rate: 50 mV s^{-1}).

The first oxidation process starting from the Ru(II) complex is ascribed to the Ru(III)/Ru(II) redox couple. In the pH range of 3.0 to 6.3, a plot of the potential versus pH was linear with a slope of –0.059 V/pH (Fig. 11), indicating that the redox couple has been assigned to one electron, one proton transfer in this pH range:

$$[Ru^{II}(trpy)(H_2bim)(OH_2)]^{2+} \leftrightarrows [Ru^{III}(trpy)(H_2bim)(OH)]^{2+} + H^+ + e^-$$

At low pH values (pH < 3), the first oxidation potentials do not depend on pH, indicating that this process involves no proton transfer:

$$[Ru^{II}(trpy)(H_2bim)(OH_2)]^{2+} \leftrightarrows [Ru^{III}(trpy)(H_2bim)(OH_2)]^{3+} + e^-$$

On the other hand, the slope in the pH range of 6.3 to 8.8 was found to be –0.10 V/pH. This clearly indicates the redox process is a one-electron process coupled with two proton transfer:

$[Ru^{II}(trpy)(H_2bim)(OH_2)]^{2+} \leftrightarrows [Ru^{III}(trpy)(Hbim)(OH)]^{+} + 2H^{+} + e^{-}$

The pK_a values found from the diagram agree well with those determined spectrophotometrically (pK_{a1} = 9.0 and pK_{a2} = 11.3). The smaller peaks after the Ru(III)/Ru(II) redox couple (Fig. 10) are ascribed to the Ru(IV)/Ru(III), Hbim•/H_2bim, and bim/Hbim• couples. However, the Ru(IV)/Ru(III) couple was not clearly observable at low pH values (pH < 3). In SWV, the intensity of peak current depends on the reversibility of the corresponding redox couple.[32] The Ru^{IV}=O/Ru^{III}-OH_2 couple corresponds to a one-electron process coupled with two proton transfer, and thus tends to be less reversible. Similar behaviors have commonly been observed for other ruthenium complexes with an aqua ligand, such as $[Ru(trpy)(bpy)(OH_2)]^{2+}$ and $[Ru(tmtacn)(bpy)(OH_2)]^{2+}$.[27, 30, 33.]

Both M-OH_2 and H_2bim moieties are known to serve as PCET modules, as illustrated in Schemes 1 and 2. Indeed, the Pourbaix diagram of **2** clearly reveals that both the PCET modules in **2** show two-step PCET processes. As a result, **2** demonstrates four-step PCET reactions to give the four-electron oxidized species, $[Ru^{IV}(trpy)(bim)(O)]^{2+}$, without electrostatic charge buildup during the reactions (Scheme 4). The multiple PCET ability of **2** would be applicable to various multi-electron oxidation reactions.

In the initial attempt to demonstrate multi-electron oxidation reactions by **2**, catalysis of electrochemical water oxidation was evaluated. Cyclic voltammogram of **2** in aqueous 0.5 M H_2SO_4 (pH = 0.4) under Ar atmosphere (Fig. 12) exhibits a large irreversible anodic current at *ca*. 1.2 V *vs*. SCE, which is considered to be a catalytic current attributed to water oxidation.[3b,32] It is also found that the O_2-evolving potential (the potential at which the catalytic current for water oxidation starts to flow) for **2** (*E* = *ca*. 1.2 V) is largely shifted to the lower potential compared with the other analogous ruthenium complexes, $[Ru(trpy)(bpy)(OH_2)]^{2+}$ (*E* = *ca*. 1.35 V),[30] $[Ru(trpy)(bpm)(OH_2)]^{2+}$ (*E* = *ca*. 1.35 V),[28] and $[Ru(tmtacn)(bpy)(OH_2)]^{2+}$ (*E* = *ca*. 1.40 V),[33] which are known as an active catalyst for water oxidation. This may be due to the multi-electron storage ability of **2** as well as the stronger electron-donating character of H_2bim ligand than that of 2,2'-bpy, 2,2'-bpm.

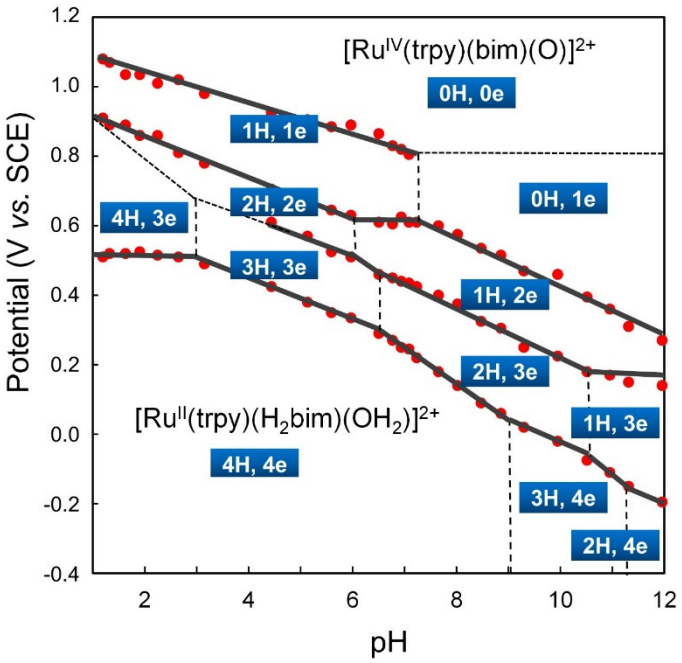

Figure 11. Plots of $E_{1/2}$ (V *vs*. SCE) vs. pH (Pourbaix diagram) for **2**. Blue squares with [mH, ne] are abbreviations for deprotonated/oxidized forms of **2**, where m and n are the numbers of removable protons and electrons, respectively, and $[Ru(trpy)(H_2bim)(OH_2)]^{2+}$ is defined as [4H, 4e].

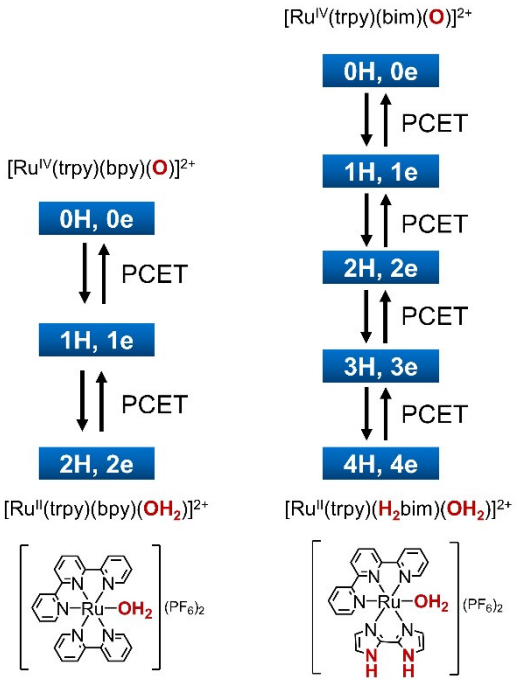

Scheme 4. Two-step and four-step PCET reactions of $[Ru(trpy)(bpy)(OH_2)]^{2+}$ (ref. 27) and $[Ru(trpy)(H_2bim)(OH_2)]^{2+}$ (**2**).

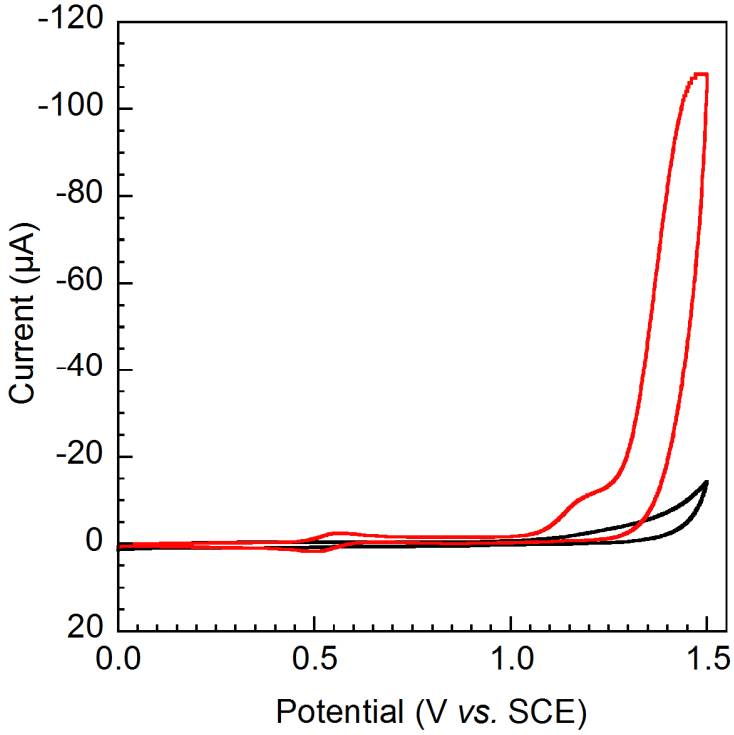

Figure 12. Cyclic voltammograms (0.5 mM) of **2** in an aqueous 1 N H_2SO_4 solution (red dotted line) and blank solution (black line) under Ar atmosphere (WE : GC, CE : Pt wire, RE : SCE ; Scan rate : 10 mV/s).

Conclusions

The author succeeded in the synthesis and characterization of a new ruthenium(II) complex showing multiple PCET properties by incorporating two kinds of PCET modules (H_2bim and M-OH_2) in a single molecule. This is the first example of study providing important new insights into the acid-base and redox properties of such complexes. The most significant result in this study is a realization of the four-step PCET reaction of the complex to give the four-electron oxidized species without electrostatic charge buildup during the reactions. Moreover, catalytic water oxidation reaction by the complex is also demonstrated. This would provide some new ideas for designing efficient catalysts for multi-electron oxidation/reduction reactions.

References

1 a) T. J. Meyer, M. H. V. Huynh and H. H. Thorp, *Angew. Chem. Int. Ed.* **2007**, *46*, 5284; b) J. P. McEvoy and G. W. Brudvig, *Phys. Chem. Chem. Phys.* **2004**, *6*, 4754; c) Tommos, C. and G. T. Babcock, *Biochim. Biophys. Acta, Bioenerg.* **2000**, *1458*, 199.

2 a) Per E. M. Siegbahn and J. Westerberg, *J. Phys. Chem. B* **1998**, *102*, 1615; b) W. N. Lanzilotta, J. Christiansen, D. R. Dean and L. C. Seefeldt, *Biochemistry* **1998**, *37*, 11376.

3 a) S. Romain, L. Vigara and A. Llobet, *Acc. Chem. Res*. **2009**, *42*, 1944; b) J. J. Concepcion, J. W. Jurss, M. K. Brennaman, P. G. Hoertz, A. O. T. Patrocinio, N. Y. M. Iha, J. L. Templeton, and T. J. Meyer, *Acc. Chem. Res*. **2009**, *42*, 1954; c) D. G. Nocera, *Acc. Chem. Res*. **2012**, *45*, 767.

4 a)M. H. Huynh and T. J. Meyer, *Chem. Rev.* **2007**, *107*, 5004; b) J. J. Warren, T. A. Tronic and J. M. Mayer, *Chem. Rev*. **2010**, *110*, 6961.

5 a) C. Costentin, M. Robert, J.-M. Savéant and A.-L.Teillout, *Proc. Natl Acad. Sci.* USA **2009**, *106*, 11829; b) T. Irebo, S. Y. Reece, M. Sjödin, D. G. Nocera and L. Hammarström, *J. Am. Chem. Soc.* **2007**, *129*, 15462; c) M. T. Irebo, O. Johansson and L. Hammarström, *J. Am. Chem. Soc.* **2011**, *133*, 13224; d) M. Sjödin, S. Styring, H. Wolpher, Y. Xu, L.Sun and L. Hammarström, *J. Am. Chem. Soc.* **2005**, *127*, 3855; e) E. A. Marder and J. M. Mayer, *Inorg. Chem.* **2010**, *49*, 3685; f) R. I. Cukier, *J.Phys. Chem.* **1996**, *100*, 15428; g) R.I. Cukier, *J. Phys. Chem. B* **2002**, *106*, 1746; h) J. H. Skone, A. V. Soudackov and S. Hammes-Schiffer, *J. Am. Chem. Soc.* **2006**, *128*, 16655; i) S. H.-Shiffer, *Acc. Chem. Res.* 2001, **34**, 273; j) O. S. Wenger, *Chem. Eur. J.* **2011**, *17*, 11692; k) R. I. Cukier and D. G. Nocera, *Annu. Rev. Phys. Chem*. **1998**, *49*, 337; l) S. J. Slattery, J. K. Blaho, J. Lehnes, and K. A. Goldsby, *Coord. Chem. Rev*. **1998**, *174*, 391; m) V. R. I. Kaila and G. Hummer, *J. Am. Chem. Soc*. **2011**, *133*, 47, 19040; n) C. Costentin, *Chem. Rev.* **2008**, *108*, 2145; o) S. Miyazaki, T. Kojima, J. M. Mayer and S. Fukuzumi, *J. Am. Chem. Soc*. **2009**, *131*, 11615; p) M. Haga, T. Ano, K. Kano and S. Yamabe, *Inorg. Chem.* **1991**, *30*, 3843; q) J. Rosenthal and D. G. Nocera, *Acc. Chem. Res.* **2007**, *40*, 543; r) Y. Georgievskii and A. A. Stuchebrukhov, *J. Chem. Phys.* **2000**, *113*, 10438.

6 a) M. Navarro, W. F. D. Giovani and J. R. Romero, *J. Mol. Catal. A* **1998**, *135*, 249; b) A. Moyer, M. S. Thompson and T. J. Meyer, *J. Am. Chem. Soc*. **1980**, *102*, 2310; c) M. S. Thompson, W. F. De Giovani. B. A. Moyer and T. J. Meyer, *J. Org. Chem.* **1984**, *49*, 4972; d) W. Nam, *Acc. Chem. Res.* **2007**, *40*, 522; e) R. H. Holm, *Chem. Rev*. **1987**, *87*, 1401.

7 a) D. L. Jenson and B. A. Barry, *J. Am. Chem. Soc.* **2009**, *131*, 10567; b) P. E. M. Siegbahn and M. R. A. Blomberg, *Chem. Rev*. **2010**, *110*, 7040; c) K. Saito, J.-R. Shen, T. Ishida and H. Ishikita, *Biochemistry* **2011**, *50*, 9836.

8 a) T. Akutagawa and G. Saito, *Bull. Chem. Soc. Jpn*. **1995**, *68*, 1753; b) T.Akutagawa, G.Saito, H.Yamochi, M.Kusunoki and K.Sakaguchi, *Synthetic Metals* **1995***, 69,* 591.

9 a) O. S. Wenger, *Chem. Eur. J*. **2011**, *17*, 11692; b) D. P. Rillema, R. Sahai, P. Matthews, A. K. Edwards, R. J. Shaver and L. Morgan, *Inorg. Chem*. **1990**, *29*, 167.

10 a) Y. Himeda, N. O.-Komatsuzaki, S. Miyazawa, H. Sugihara, T. Hirose and K. Kasuga, *Chem. Eur. J.* **2008**, *14*, 11076; b) S. Roeser, P. Farràs, F. Bozoglian, M. M.-Belmonte, J. B.-Buchholz and A. Llobet, *ChemSusChem* **2011**, *4*, 197; c) S. Maji, B. Sarkar, M. Patra, A. K. Das, S. M. Mobin, W. Kaim and G. K. Lahiri, *Inorg. Chem.* **2008**, *47*, 3218; d) N. Chanda, D. Paul, S. Kar, S. M. Mobin,A. Datta, V. G. Puranik, K. K. Rao and G. K. Lahiri, *Inorg. Chem.* **2005**, *44*, 3499.

11 B.P. Sullivan, J. M. Calver and T. J. Meyer, *Inorg. Chem.* **1980**, *19*, 1404.

12 R. Steffens and W. Schunack, *Arch. Pharm.* **1986**, *319*, 183.

13 Bruker. APEX2 and *SAINT*. Bruker AXS Inc., Madison, Wisconsin, USA, **2007**.

14 G. M. Sheldrick, *SADABS*, University of Gçttingen, Germany, **1996**.

15 G. M. Sheldrick, *Acta Crystallogr. Sect. A* **2008**, *64*, 112.

16 A. Altomare, G. Cascarano, C. Giacovazzo and A.J. Guagliardi, *J. Appl. Cryst.* **1993**, *26*, 343.

17 a) L. J. Farrugia, *J. Appl. Crystallogr*. **1997**, *30*, 565; b) T. D. Fenn, D. Ringe and G. A. Petsko, *J. Appl. Crystallogr*. **2003**, *36*, 944.

18 *Gaussian 03*, Revision E.01, M. J. Frisch, G. W. Trucks, H. B. Schl-egel, G. E. Scuseria, M. A. Robb, J. R. Cheeseman, J. A. Montgomery, Jr., T. Vreven, K. N. Kudin, J. C. Burant, J. M. Millam, S. S. Iyengar, J. Tomasi, V. Barone, B. Mennucci, M. Cossi, G. Scalmani, N. Rega, G. A. Petersson, H. Nakatsuji, M. Hada, M. Ehara, K. Toyota, R. Fukuda, J. Hasegawa, M. Ishida, N. Nakajima, Y. Honda, O. Kitao, H. Nakai, M. Klene, X. Li, J. E. Knox, H. P. Hratchian, J. B. Cross, V. Bakken, C. Adamo, J. Jaramillo, R. Gomperts, R. E. Stratmann, O. Yazyev,A. Austin, R. Cammi, C. Pomelli, J. W. Ochterski, P. Y. Ayala, K. Morokuma, G. A. Voth, P. Salvador, J. J. Dannenberg, V. G. Zakrzewski, S. Dapprich, A. D. Daniels, M. C. Strain, O. Farkas, D. K. Malick, A. D. Rabuck, K. Raghavachari, J. B. Foresman, J. V. Ortiz, Q. Cui, A. G. Baboul, S. Clifford, J. Cioslowski, B. B. Stefanov, G. Liu, A. Liashenko, P. Piskorz, I. Komaromi, R. L. Martin, D. J. Fox, T. Keith, M. A. Al-Laham, C. Y. Peng, A. Nanayakkara, M. Challacombe, P. M. W. Gill, B. Johnson, W. Chen, M. W. Wong, C. Gonzalez and J. A. Pople, Gaussian, Inc., Wallingford CT, **2004**.

19 A. D. Becke, *J. Chem. Phys*. **1993**, *98*, 5648.

20 C. Lee, W. Yang and R. G. Parr, *Phys. Rev. B* **1988**, *37*, 785.

21 a) T. H. Dunning, Jr. and P. J. Hay, in *Modern Theoretical Chemistry*, ed. H. F. Schaefer, III, Plenum, New York, **1976**; b) P. J. Hay and W. R. Wadt, *J. Chem. Phys*. **1985**, *82*, 270; c) P. J. Hay and W. R. Wadt, *J. Chem. Phys*. **1985**, *82*, 299.

22 M. Cossi, G. Scalmani, N. Rega, V. Barone, *J. Chem. Phys*. **2002**, *117*, 43.

23 a) M. E. Casida, C. Jamorski, K. C. Casida, D. R. Salahub, *J. Chem. Phys*. **1998**, *108*, 4439; b) R. E. Statmann, G. E. J. Scuseria, *Chem. Phys*. **1998**, *109*, 8218; c) R. Bauernschmitt, R. Ahlrichs, *Chem. Phys. Lett*. **1996**, *256*, 454.

24 A. Taketoshi, T. Koizumi and T. Kanbara, *Tetrahedron Lett.* **2010**, *51*, 6457.

25 X.-J. Yang, F. Drepper, B. Wu, W.-H. Sun, W.Haehnel and C. Janiak, *Dalton Trans*. **2005**, *26*, 256.

26 a) B.-Hui Ye, B.-B. Ding, Y.-Q. Weng and X.-M. Chen, *Inorg. Chem*. **2004**, *43*, 6866; b) B.-B. Ding, Y.-Q. Weng, Z.-W. Mao, C.-K. Lam, X.-M. Chen and B.-H. Ye, *Inorg. Chem*. **2005**, *44*, 8836; c) M. Tadokoro, H. Kanno, T. Kitajima, H. S.-Umemoto, N. Nakanishi, K. Isobe and K. Nakasuji, *Proc. Natl Acad. Sci. USA* **2002**, *99*, 4950; d) M. A. M. Lorente, F. Dahan, Y. Sanakis, V. Petrouleas, A. Bousseksou, and J.-P. Tuchagues, *Inorg. Chem*. **1995**, *34*, 5346; e) R. Atencio, K. Ramírez, J. A. Reyes, T. González and P. Silva, *Inorg. Chim. Acta* **2005**, *358*, 520; f) S. Fortin, P.-L. Fabre, M. Dartiguenave and A. L. Beauchamp, *J. Chem. Soc. Dalton Trans.* **2001**, 3520; g) T. Kundu, S. M. Mobin and G. K. Lahiri, *Dalton Trans.* **2010**, *39*, 4232.

27 K. J. Takeuchi, M. S. Thompson, D. W. Pipes and T. J. Meyer, *Inorg. Chem*. **1984**, *23*, 1845.

28 J. J. Concepcion, J. W. Jurss, J. L. Templeton and T. J. Meyer, *J. Am. Chem. Soc.* **2008**, *130*, 16462

29 N. Grover, N. Gupta, P. Singh and H. H. Thorp, *Inorg. Chem.* **1992**, *31*, 2014.

30 S. Masaoka and K. Sakai, *Chem. Lett*. **2009**, *38*, 182.

31 T. Kundu, S. M. Mobin and G. K. Lahiri, *Dalton Trans.* **2010**, *39*, 4232.

32 A. J. Bard and L. R. Faulkner, *Electrochemical Methods*, John Wiley & Sons, New York, **1980**.

33 a) M. Yoshida, S. Masaoka and K. Sakai, *Chem. Lett.* **2009**, *38*, 702; b) M. Yoshida, S. Masaoka, J. Abe and K. Sakai, *Chem. Asian J*. **2010**, *5*, 2369.

Chapter 2

Section 1.

A pentanuclear iron catalyst designed for water oxidation

Introduction

Water oxidation catalysts[1-17] have attracted increasing interest motivated by the recent elucidation of the OEC[18] structure and driven by the urgent need to develop efficient catalysts for energy conversion systems. There are two primary approaches to developing water oxidation catalysts, homogeneous[1-15] and heterogeneous systems[16,17]. Homogeneous molecular catalysts have an advantage in catalyst design at the molecular level based on the detailed mechanistic study. One of the important long-standing goals is the development of efficient molecular catalysts based on abundant, inexpensive and environmentally benign metal ions. Iron, the most abundant transition metal element in the earth's crust, is an attractive candidate as a constituent element of water oxidation catalysts, and iron complexes are often employed as catalysts for various oxidation reactions in both natural[19,20] and artificial systems[21]. A few examples of artificial iron-based water oxidation catalysts have recently been reported, focusing on mononuclear iron complexes[5,8,12,14]. However, in most cases, the catalysts are rapidly deactivated owing to their decomposition during reaction[5,12]. In addition, their catalytic activities are much lower than those of the reported molecular catalysts based on other metal ions (see Table 5, P. 75,76). These limitations of the reported iron-based water oxidation catalysts have prompted us to explore a new molecular design to create iron-based catalysts with high performance.

Efficient iron-based molecular catalysts for water oxidation should include the following key elements: (i) the catalysts should have multinuclear structures. Redox flexibility arising from the multinuclear core is expected to be advantageous in reactions involving multi-electron transfer (Fig. 1a). Indeed, multinuclear clusters have been selected as active centers for such reactions in nature; *e.g.*, the Mn_4Ca cluster in PSII for the four-electron oxidation of water[18,22] and the Fe_7Mo cluster in nitrogenase for the six-

electron reduction of nitrogen[23]. And (ii) two water-activation sites separated by an appropriate distance must exist to promote intramolecular O-O bond formation (Fig. 1b). *Inter*molecular O-O bond formation, which involves the association of two molecules, is often very slow, and can be the rate-determining step of the reaction[7,10,11,13]. The intramolecular O-O bond formation may accelerate the catalytic reactions because the slow association step can be avoided by going through the intramolecular process. Note that dinuclear iron cores are known to serve as the active sites for O-O bond formation and/or scission[24, 25].

As a candidate for water oxidation catalysts, we employed a pentanuclear iron complex with open-coordination sites, $[Fe^{II}_4Fe^{III}(\mu_3\text{-}O)(\mu\text{-}\mathbf{L})_6]^{3+}$ (**1**; **L**H = 3,5-bis(2-pyridyl)pyrazole; Fig. 1c). **1** has quasi-D_3 symmetry and consists of a $[Fe_3(\mu_3\text{-}O)]$ core wrapped by two $[Fe(\mu\text{-}\mathbf{L})_3]$ units. The two iron ions at the apical positions are hexa-coordinated by three $\mathbf{L}^-$ to form $[Fe(\mu\text{-}\mathbf{L})_3]$ units with distorted octahedral geometries, whereas the three iron ions at the triangle $[Fe_3(\mu_3\text{-}O)]$ core are penta-coordinated by two $\mathbf{L}^-$ and an O^{2-} anion with distorted trigonal bipyramidal geometries. These penta-coordinated, or coordinatively unsaturated, iron ions in the triangle core are expected to serve as the active sites for O-O bond formation.

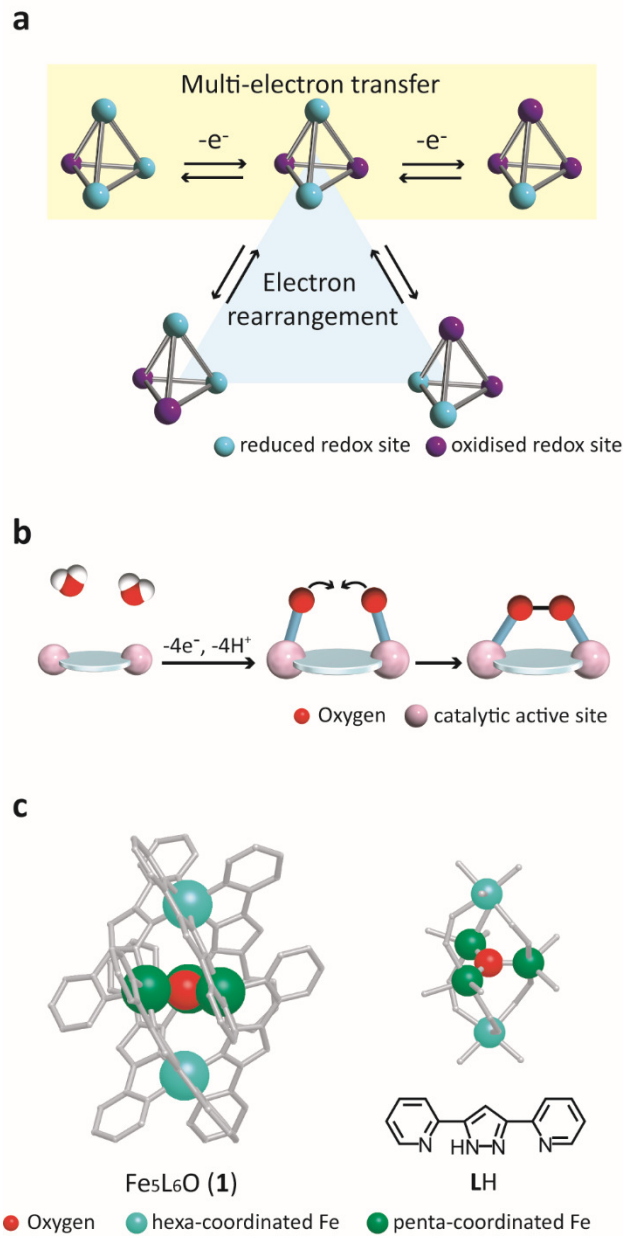

Figure 1. Design of molecular catalysts for water oxidation. (a) Redox flexibility arising from a multinuclear core. (b) Adjacent water-activation sites to promote intramolecular O-O bond formation. (c) The molecular structure and the Fe_5O core structure of $[Fe^{II}_4Fe^{III}(\mu_3\text{-}O)(\mu\text{-}\mathbf{L})_6]^{3+}$ (**1**). Three penta-coordinated iron centers are bridged by oxygen atoms in μ_3-fashion to form a triangle structure, and two hexa-coordinated iron centers are connected to the triangle structure by six **L**s.

Single Crystal X-ray Structure Determination

We synthesized complex **1** by mixing stoichiometric amounts of $Fe(SO_4)_2 \cdot 7H_2O$ and **L**H in the presence of base in MeOH at room temperature under aerobic conditions[26]. Single crystal X-ray structural analysis, elemental analysis, electrospray-ionisation time-of-flight mass spectrometry (ESI-TOF-MS) and ^{57}Fe Mössbauer spectroscopy revealed that one iron ion at the triangle core of **1** is oxidized to Fe^{III}, leading to the isolation of the $Fe^{II}_4Fe^{III}$ oxidation state (Figs. 2,3 and Table 1,2).

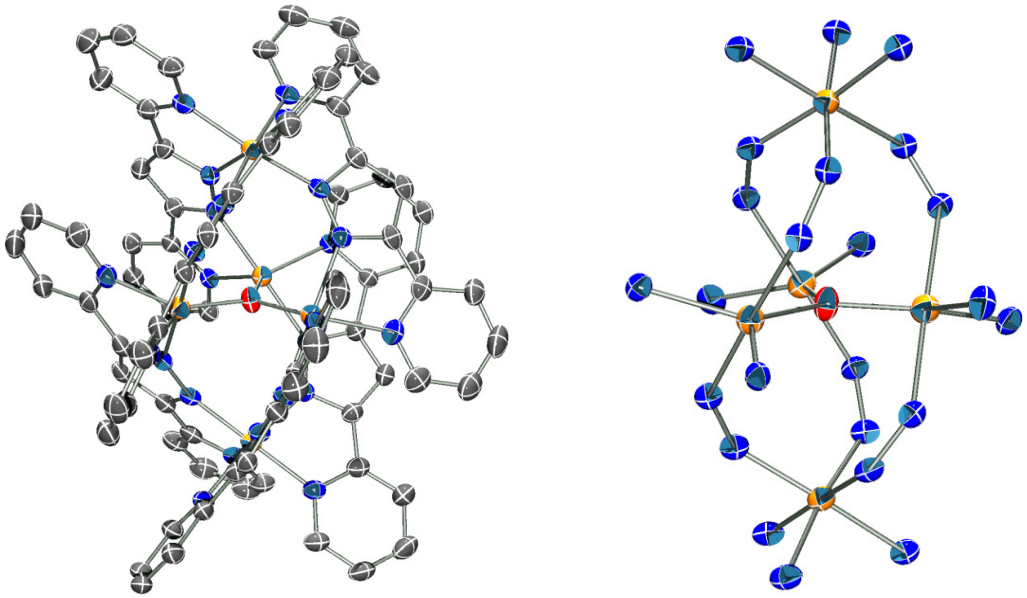

Figure 2. ORTEP drawings (50% probability ellipsoids) of the structure of cationic moiety of **1**$(BF_4)_3$ (left, hydrogen atoms are omitted for clarity) and the core structure (right, noncoordinated atoms of the $\mathbf{L}^-$ ligands omitted for clarity). O = red, C = grey N = blue, Fe = orange.

Table 1. Summary of the crystallographic data for **1**$(BF_4)_3$.

Formula	$C_{78}H_{54}N_{24}OFe_5B_3F_{12}$
Fw	1883.13
Crystal color, habit	red, block
Crystal size, mm^3	0.22 × 0.1 × 0.08
Crystal system	tetragonal
Space group	*I* -4
a, Å	16.6876(3)
c, Å	30.1763(7)
Z	4
F(000)	3804
d_{calc}, g/cm^3	1.488
μ(MoKα), mm^{-1}	0.929
T, K	123(2)
R_1	0.0526
wR_2	0.1503
GOF	1.099

^{57}Fe Mössbauer spectroscopy

A ^{57}Fe Mössbauer spectrum was measured to characterize the electronic states of the Fe centers in the catalyst. The measurement of **1**$(BF_4)_3 \cdot 7H_2O$ was carried out at 100 K. The spectrum consists of three quadrupole doublets with relative peak areas of 2:2:1, which correspond to low-spin Fe^{II} ions (IS = 0.33 mm s^{-1}, QS = 0.25 mm s^{-1}), high-spin Fe^{II} ions (isomer shift (IS) = 0.82 mm s^{-1}, quadrupole splitting (QS) = 3.16 mm s^{-1}), and high-spin Fe^{III} ion (IS = 0.49 mm s^{-1}, QS = 1.85 mm s^{-1}), respectively (Fig. 3, and Table 2). These results suggest that two iron centers at the apical positions are low-spin Fe^{II} ions and that the [$Fe_3(\mu_3$-O)] core is composed of two high-spin Fe^{II} ions and one high-spin Fe^{III} ion.

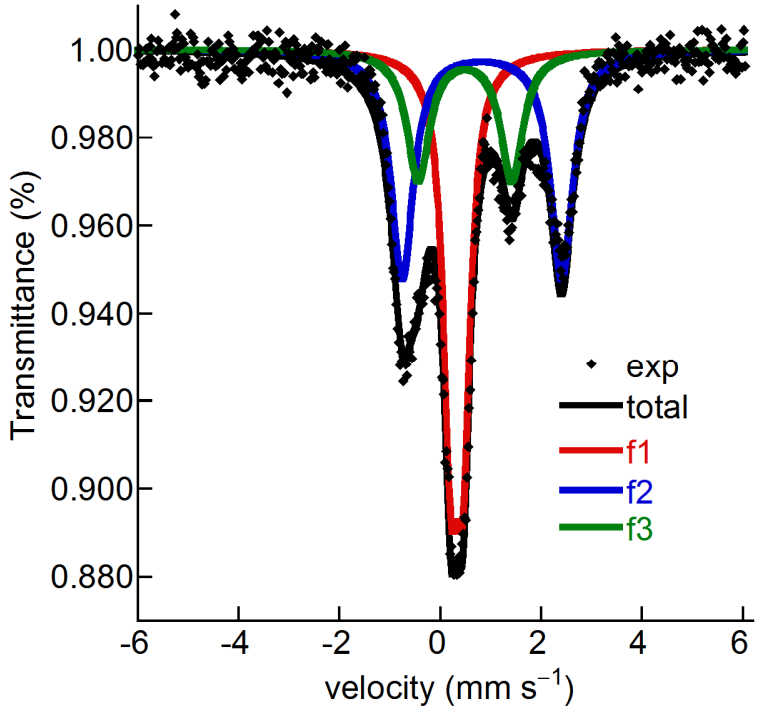

Figure 3. A ^{57}Fe Mössbauer spectrum of **1**$(BF_4)_3 \cdot 7H_2O$ at 100 K.

Table 2. ^{57}Fe Mössbauer least-squares fitting parameters for **1**$(BF_4)_3 \cdot 7H_2O$ at 100 K.

	f1	f2	f3
IS (mm s^{-1})	0.33	0.82	0.49
QS (mm s^{-1})	0.25	3.16	1.85
ratio (%)	39.2	38.6	22.2
assignment	Fe(II) LS	Fe(II) HS	Fe(III) HS

Cyclic Voltammetry

The cyclic voltammogram (CV) of **1** (0.2 mM) in an acetonitrile solution containing Et_4NClO_4 (0.1 M) at a scan rate of 10 mV s^{-1} (Fig. 4) revealed one reversible reduction wave at $E_{1/2}$ = –0.55 V *vs.* ferrocene/ferrocenium (Fc/Fc^+) and four reversible oxidation waves at $E_{1/2}$ = 0.13, 0.30, 0.68 and 1.08 V. The five reversible redox waves were assigned to the sequential one-electron redox couple of each iron ion between Fe^{II} and Fe^{III}. Thus, **1** possesses high redox flexibility with six different redox states that are accessible under electrochemical conditions. The open-circuit potential of **1** was determined to be –0.26 V, indicating that **1** possesses the $Fe^{II}_4Fe^{III}$ state in both the solution and solid states (*vide supra*). Importantly, the profile of the cyclic voltammogram of **1** changed dramatically upon the addition of water, as shown in Figure 5. Large irreversible anodic currents were observed at the potential corresponding to the $Fe^{III}_5/Fe^{II}Fe^{III}_4$ redox couple, suggesting electrocatalytic O_2 evolution from water.

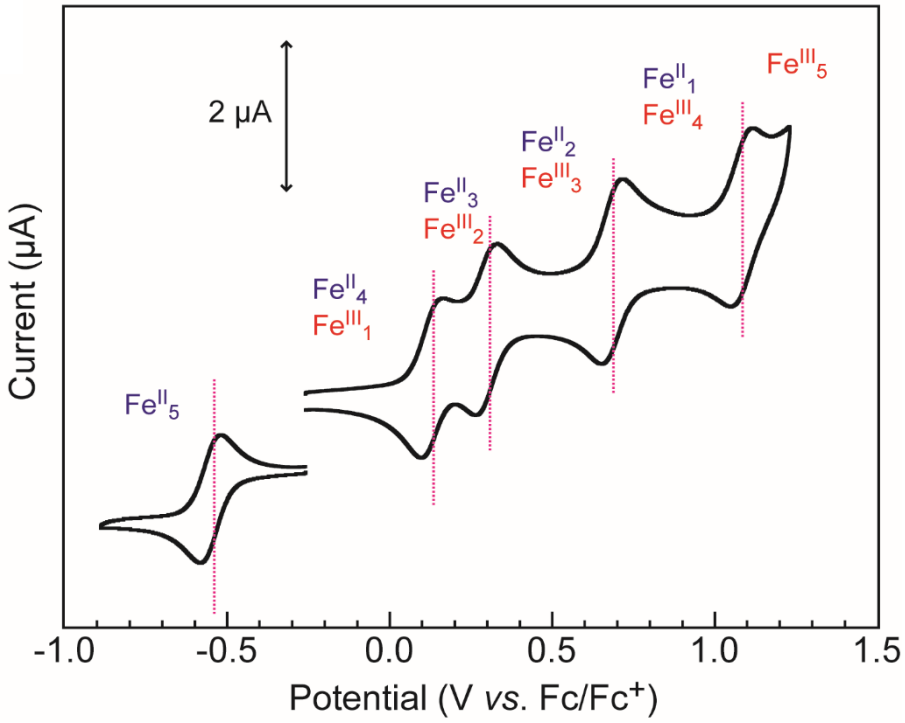

Figure 4. CV of **1** (0.2 mM) in an acetonitrile solution with Et_4NClO_4 (0.1 M) at a scan rate of 10 mV s^{-1}.

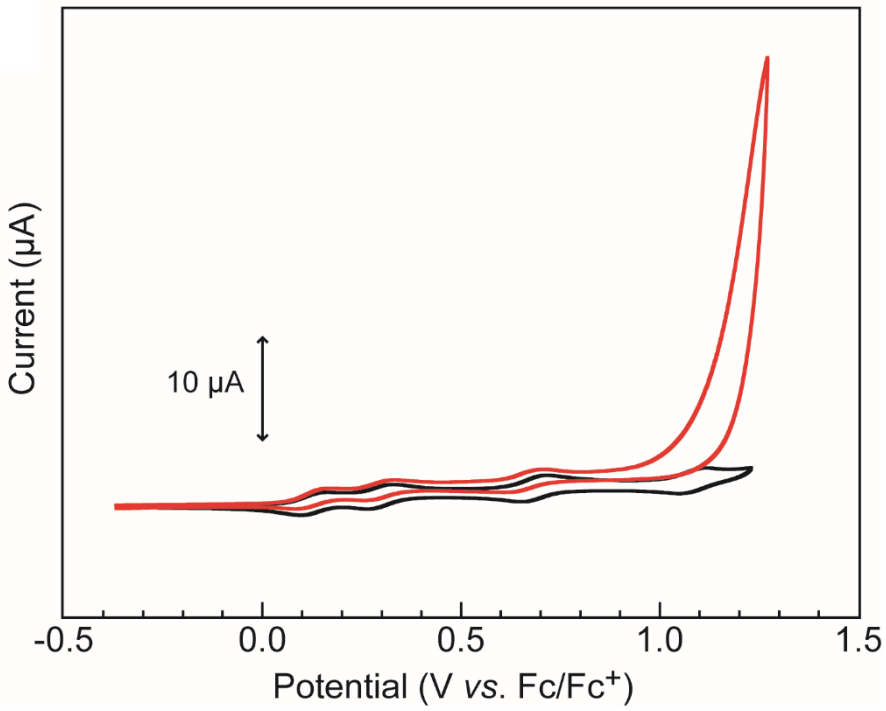

Figure 5. CVs of **1** (0.2 mM) in acetonitrile solutions with Et_4NClO_4 (0.1 M) at a scan rate of 10 mV s^{-1} with 5 M of H_2O (red line) and without water (black line).

Controlled Potential Electrolysis

To quantitatively evaluate the evolution of O_2 from water, controlled potential electrolysis was conducted in a two-compartment cell separated by an anion-exchange membrane (Fig. 6). The solution of **1** (0.2 mM) in an acetonitrile/water (10 : 1) mixed solution containing Et_4NClO_4 (0.1 M) was electrolysed at the ITO electrode with a cell operating potential of 1.42 V *vs*. Fc/Fc^+, and the evolved O_2 was quantified by gas chromatography. As shown in Figure 7, the total amount of charge passed was confirmed to be 41.0 coulombs over a period of 120 min, and the amount of evolved O_2 was determined to be 2.5 mL, showing a Faradaic efficiency of 96% based on a $4e^-$ process. The profile of the water oxidation curve was nearly linear, indicating that the steady-state intermediate of the catalyst remained stable throughout the catalytic cycles in solution. Several experiments were performed to check for the reproducibility and the similar Faradaic efficiency (95-97%) were obtained for all entries (Table 3).

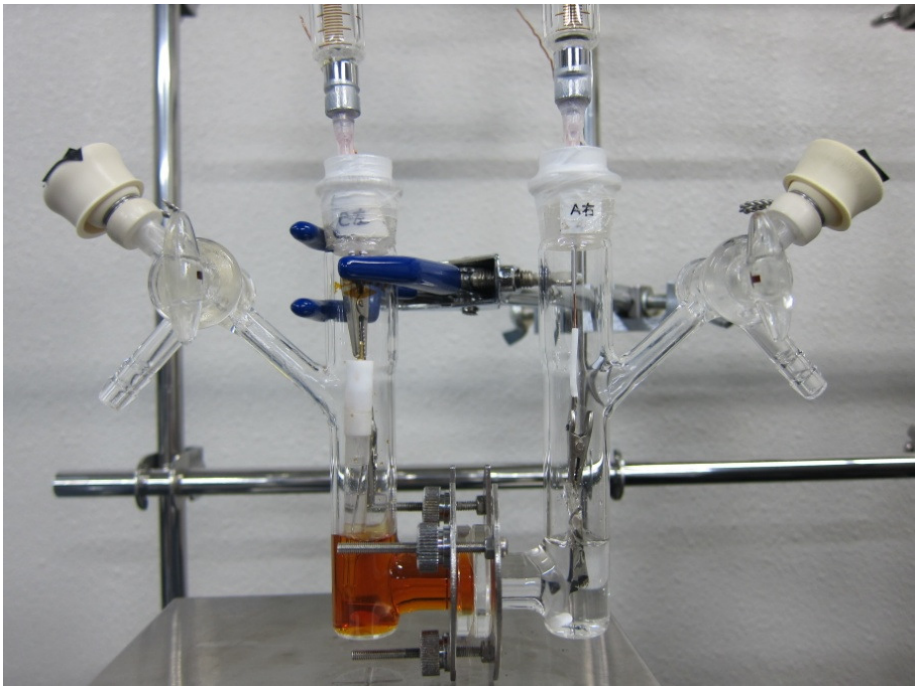

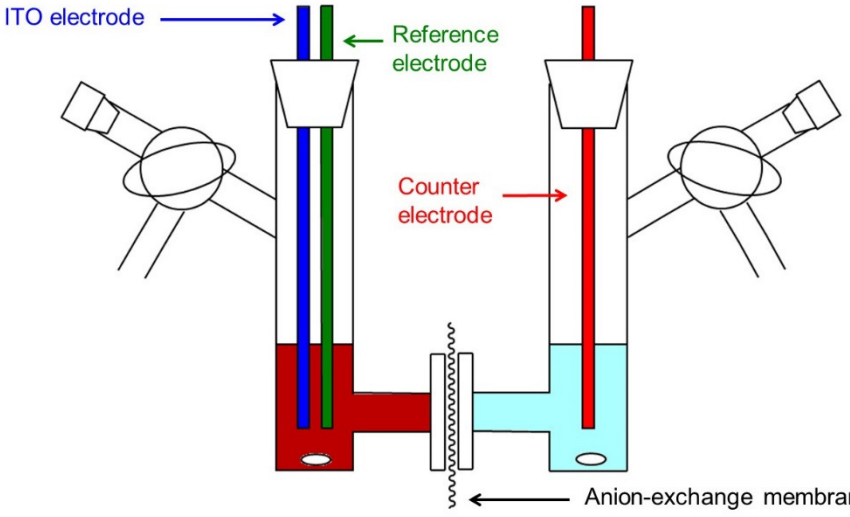

Figure 6. Photograph (top) and schematic illustration (bottom) of a custom-designed two compartment cell used in the controlled potential electrolysis.

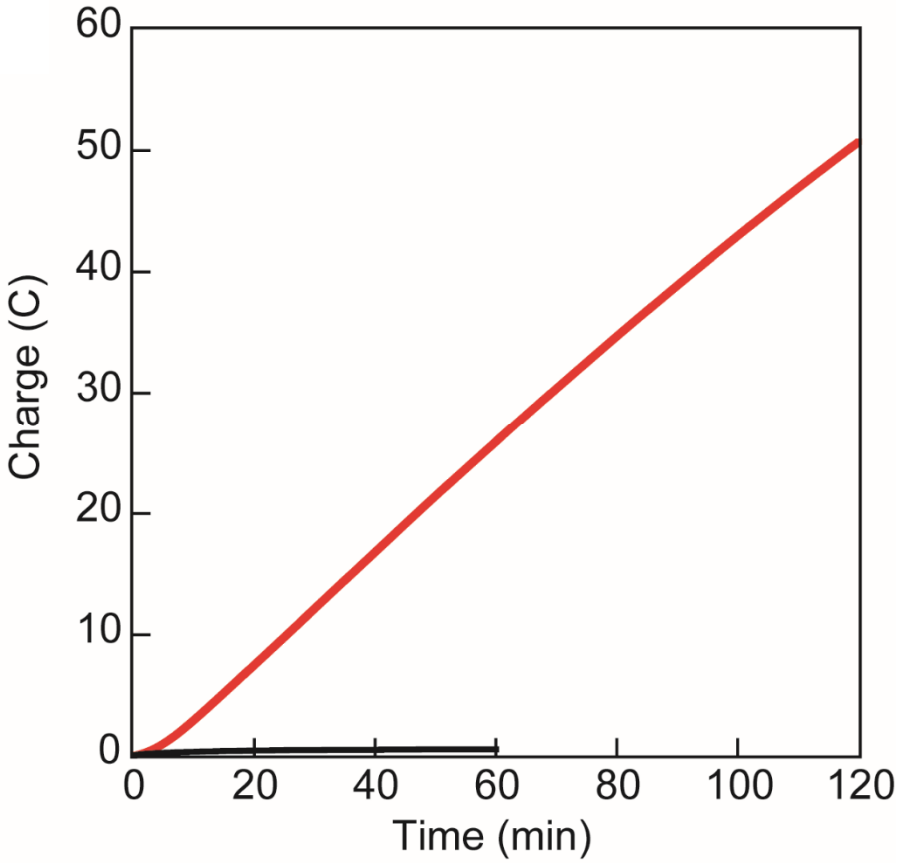

Figure 7. Electrolysis data in acetonitrile/water (10 : 1) mixed solutions with Et_4NClO_4 (0.1 M) at a potential of 1.42 V *vs.* Fc/Fc^+ with 0.2 mM of **1** (red line) and without the catalyst (black line).

Table 3. Summary of the controlled potential electrolysis for **1**. The pH of the solution was 4.8 before electrolysis and decreased to less than 0.5 after 2 hours of electrolysis.

	Electrolysis Time (min)	Charge (C)	O_2 Evolved (ml)	Faradaic Efficiency (%)
Entry 1[a)]	120	41.0	2.45	96
Entry 2	120	50.7	3.07	97
Entry 3	90	31.0	1.84	95
Entry 4	60	25.9	1.57	97

[a)] The plot of charge (C) *vs.* time (min) is shown in Figure 7.

Evidence for a Homogeneous Electrocatalyst

The stability of **1** during the catalysis was confirmed by the following several analyses. First, multiple scans of CVs of **1** showed that Both the wave shape of each Fe^{III}/Fe^{II} process and the catalytic current for water oxidation were maintained over 100 scans of the CVs for 9 h (Fig. 8), indicating that the decomposition and deposition of **1** do not generally occur under electrochemical conditions.

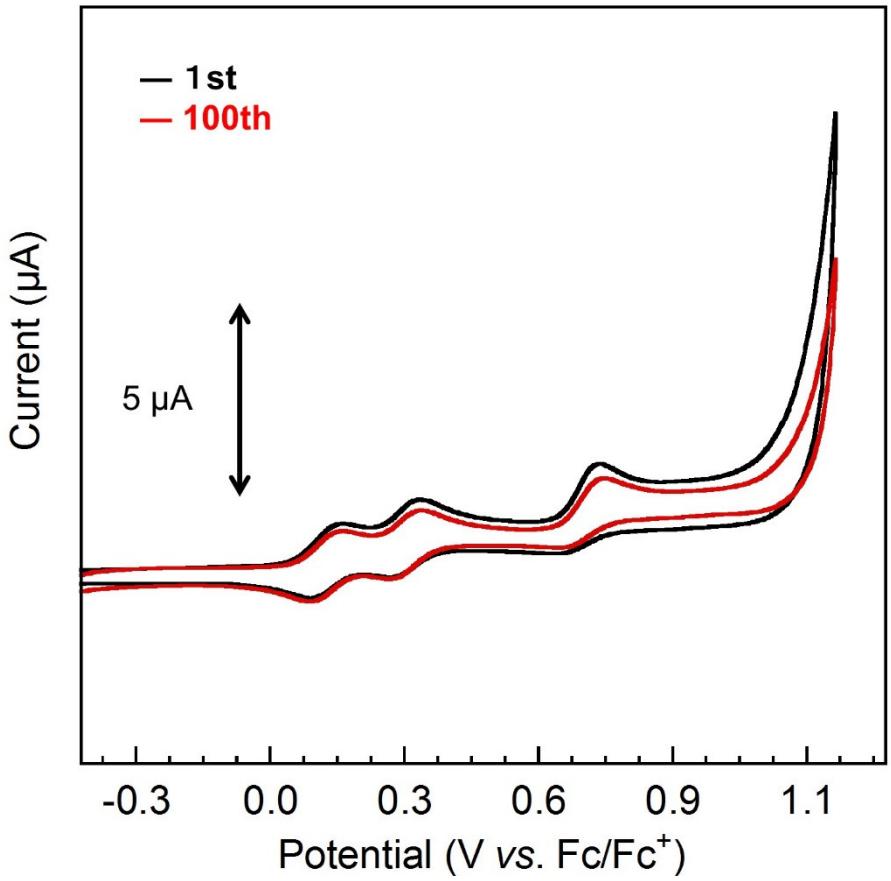

Figure 8. CVs of **1** (0.2 mM) with 0.1 M Et_4NClO_4 as the supporting electrolyte at a scan rate of 10 mV s^{-1} in an acetonitrile/water (10 : 1) mixed solution. The potential sweep in the range from -0.44 to 1.19 V was repeatedly carried out 100 times without pause. Electrodes: working, GC; auxiliary, Pt; reference, Ag/Ag^+; reported *vs.* Fc/Fc^+.

Second, both the wave shapes of the Fe(II/III) processes and the catalytic current for water oxidation were maintained after the controlled potential electrolysis for 1 h (Fig 9). The controlled potential electrolysis was performed at 1.19 V *vs.* Fc/Fc^+ with 0.2 mM of **1** for an hour. After the electrode was polished with alumina paste, the CV was recorded in the range from -0.50 to 1.19 V (red line).

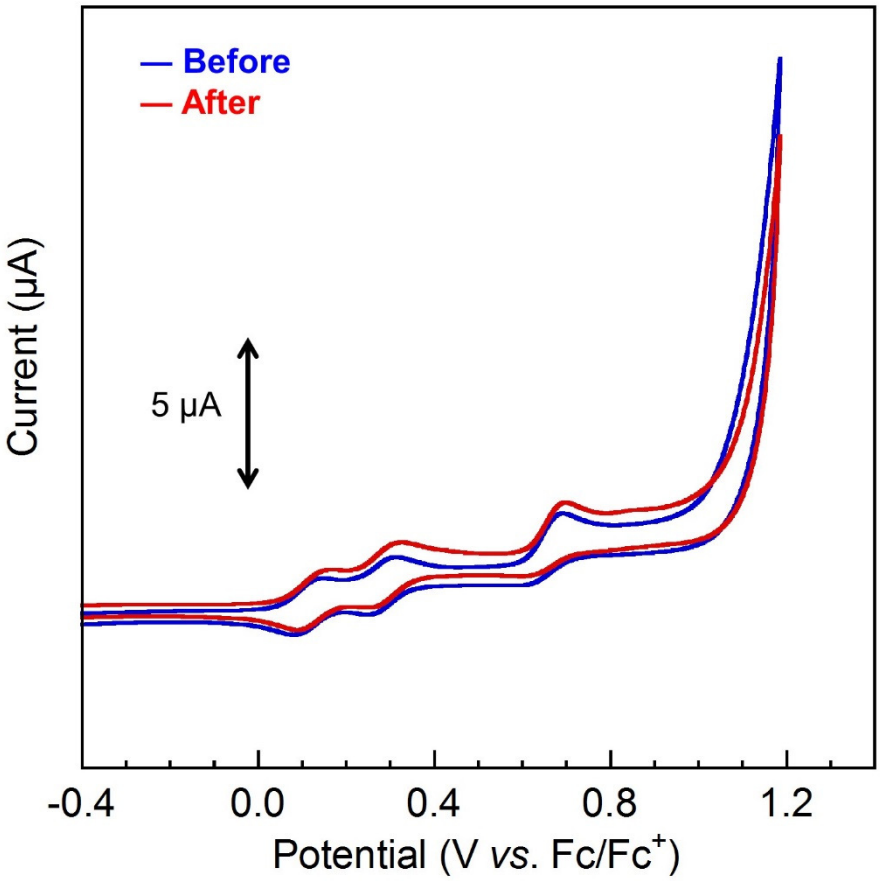

Figure 9. CVs of **1** (0.2 mM) before (blue line) and after (red line) the electrolysis. The measurements were performed in an acetonitrile/water (10 : 1) mixed solution with 0.1 M Et_4NClO_4 as the supporting electrolyte at a scan rate of 10 mV s^{-1}. Electrodes: working, GC; auxiliary, Pt; reference, Ag/Ag^+; reported *vs*. Fc/Fc^+.

Third, the catalytic ability of the electrode after the controlled potential electrolysis was examined (Fig. 10). In this experiment, the electrolysis was initially performed in acetonitrile/water (10 : 1) mixed solutions with Et_4NClO_4 (0.1 M) at a potential of 1.42 V *vs.* Fc/Fc^+ with 0.2 mM of **1** (red line). The ITO working electrode was gently rinsed with small amounts of water and acetonitrile, and then, a second round of electrolysis was performed using the solution without the catalyst (black line). A small current was observed in the second electrolysis compared to the first electrolysis, which indicates that the homogeneous species dissolved in the solution is a catalytic active species.

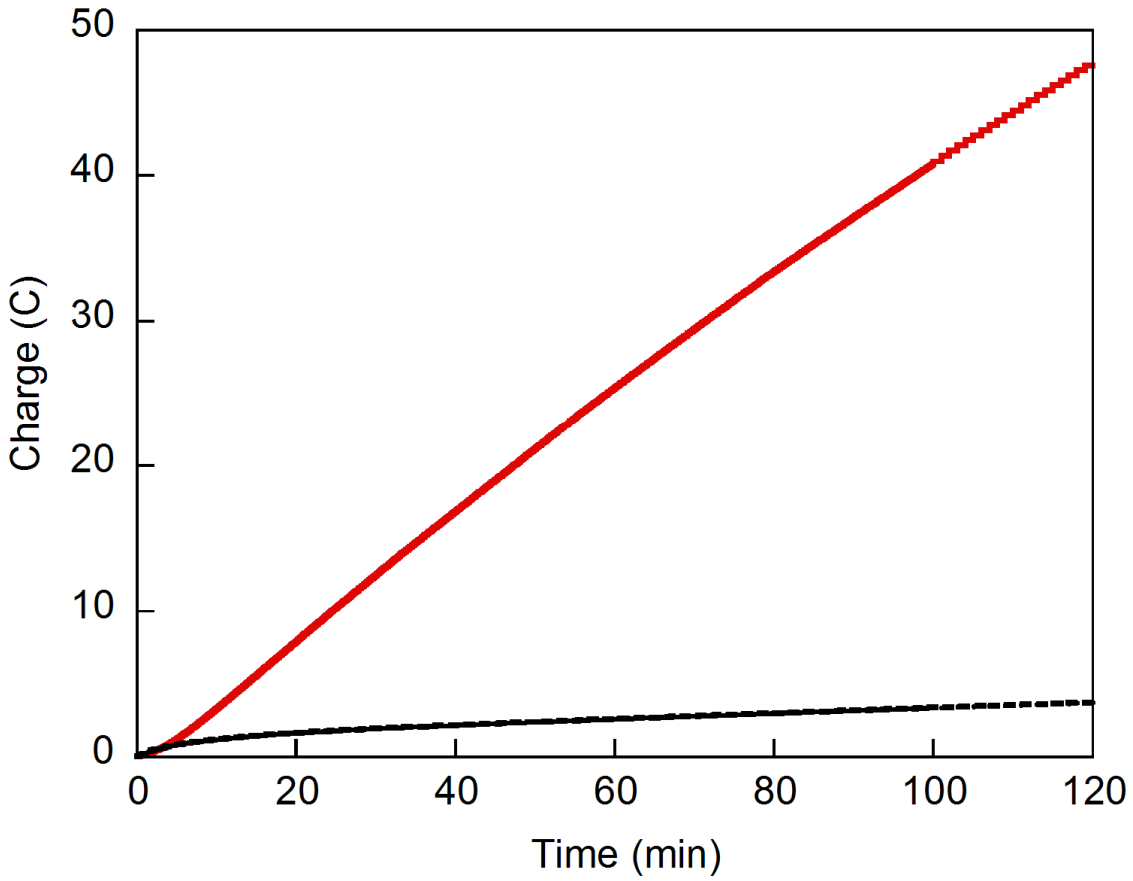

Figure 10. The result of the first electrolysis using fresh ITO electrode in 0.2 mM of **1** (red line) and that of second round of electrolysis using ITO electrode after first electrolysis in electrolyte solution without **1** (black line). Condition: acetonitrile/water (10 : 1) mixed solution with Et_4NClO_4 (0.1 M) at a potential of 1.42 V *vs.* Fc/Fc^+.

Finally, X-ray photoelectron spectra and UV-vis absorption spectra of the ITO electrode used for the controlled potential electrolysis exactly match with those from before the electrolysis (Figs. 11 and 12). These results suggest that heterogeneous deposits did not form during the catalytic reaction. Thus, the data overall strongly indicates that **1** dissolved in the solution is the catalytic species in this system.

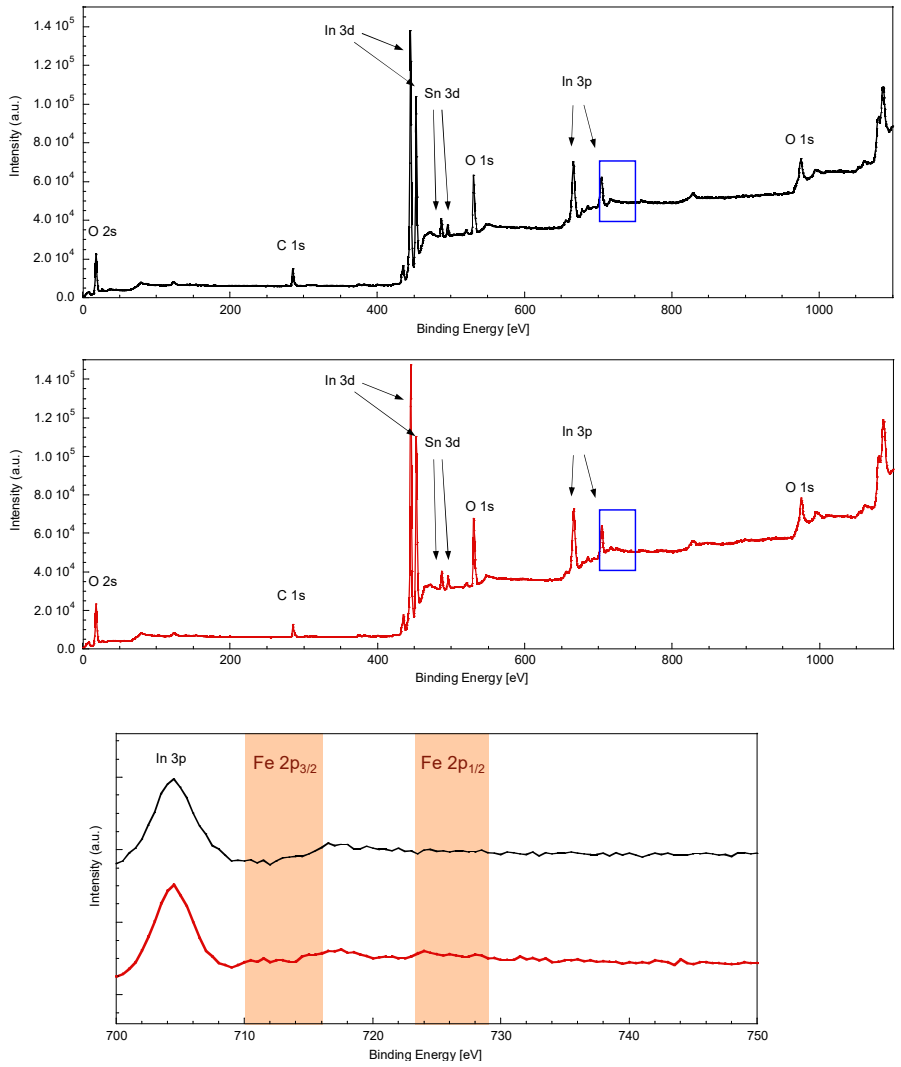

Figure 11. XPS spectra of the ITO electrode before (top, black line) and after (middle, red line) the electrolysis. The bottom graph shows the magnified spectra for typical Fe 2p region of iron oxide species.

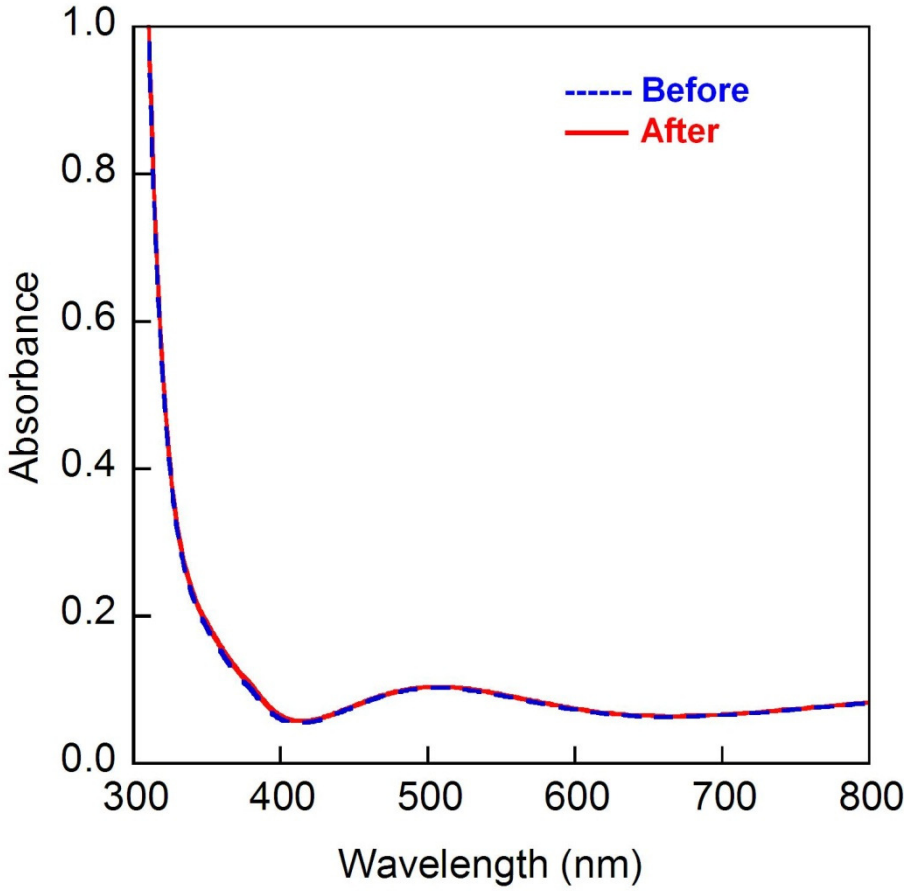

Figure 12. UV-vis absorption spectra of the ITO electrode before (blue dashed line) and after (red solid line) the electrolysis.

TOF Calculation from Cyclic Voltammetric Measurements

The catalytic activity of **1** was evaluated in terms of turnover frequency (TOF) under electrochemical conditions. When the electron transfer rate of the catalyst and the amount of the substrate are sufficiently high and when the catalytic current is limited only by the chemical reaction in solution, *i.e.*, under purely kinetic conditions[12,27-29], Eq. 1 can be used to calculate the pseudo-first-order rate constant, k_{cat}, which correspond to the TOF value for O_2 evolution.

$$\frac{i_{cat}}{i_p} = 2.242 n_{cat} \left(\frac{k_{cat} RT}{F}\right)^{\frac{1}{2}} \nu^{-\frac{1}{2}} \cdots\cdots (Eq.\ 1)$$

In this equation, i_{cat} is the catalytic current, i_p is the peak current measured in the absence of the substrate, n_{cat} is the number of electrons involved in the catalytic reaction, F is Faraday's constant, k_{cat} is the effective first-order rate constant, R is the universal gas constant, T is the temperature in Kelvin, and ν is the scan rate.

Detailes of the calculations is shown below.

(i) General Procedure [Ref. 27-29]

In the catalytic reaction scheme, a substrate, usually nonelectroactive, reacts in the following chemical reaction to regenerate starting material. The rate low of the reaction can be defined as d[P]/dt = k[cat][S].

$$R \rightleftarrows O + ne^-$$

$$O + S \xrightarrow{k} R + P$$

(R: reduced form of a catalyst, O: oxidized form of a catalyst, S: substrate, P: product)

In this case, under purely kinetic conditions, when the current is limited only by catalytic steps in solution, CVs are predicted to be S-shaped and reach a limiting catalytic current, i_{cat}, which can be expressed by the following equation (Eq. S1) and is independent of the scan rate.

$$i_{cat} = n_{cat} F A [cat]_0 \sqrt{D(k[S])} \cdots\cdots\cdots\cdots\cdots\cdots Eq.\ S1$$

where n_{cat} is the number of electrons transferred during the catalytic event, F is the Faraday's constant, A is the surface area of electrode [cm^2], $[cat]_0$ is the concentration of the catalyst, [S] is the concentration of the substrate, k is the second-order rate constant and D [$cm^2 \cdot s^{-1}$] is the diffusion coefficient of the catalyst.

Assume that the concentration of substrate does not change significantly during the course of the measurement, the catalytic turnover frequency (TOF) can be expressed as a pseudo first-order rate constant, k_{cat} ($k_{cat} = k[S]$ = TOF). Therefore i_{cat} can be expressed as follows.

$$i_{\mathrm{cat}} = n_{\mathrm{cat}} \mathrm{F} A [\mathrm{cat}]_0 \sqrt{k_{cat} D} \cdots\cdots\cdots\cdots\cdots\cdots \mathrm{Eq.\,S2}$$

On the other hand, the peak current for reversible electrochemical couples, i_p, is governed by Randles-Sevcik equation (Eq. S3) as follows,

$$i_{\mathrm{p}} = 0.4463 n_{\mathrm{p}} \mathrm{F} A [\mathrm{cat}]_0 \sqrt{\frac{n_p \mathrm{F} D v}{\mathrm{R} T}} \cdots\cdots\cdots\cdots\cdots\cdots \mathrm{Eq.\,S3}$$

where n_p is the number of electrons transferred associated with reversible electrochemical couples, R is the universal gas constant, T is the temperature, and v is the scan rate.

The ratio of i_{cat} (Eq. S2) to i_p (Eq. S3) is given by Eq. S4.

$$\frac{i_{\mathrm{cat}}}{i_{\mathrm{p}}} = \frac{n_{cat}}{0.4463 n_p} \sqrt{\frac{k_{cat} \mathrm{R} T}{n_p \mathrm{F} v}} \cdots\cdots\cdots\cdots\cdots\cdots \mathrm{Eq.\,S4}$$

In the present study, i_p values were estimated from the one-electron redox process of $Fe^{III}_5/Fe^{II}Fe^{III}_4$ and four electrons were assumed to pass for each O_2 molecule produced. Therefore, n_p and n_{cat} values were determined to be 1 and 4, respectively.

The turnover frequency (k_{cat}) can be calculated from the slope of a plot of i_{cat}/i_p against $v^{-1/2}$, C, using equation Eq. S5.

$$k_{cat} = 1.245 \times 10^{-2} \frac{\mathrm{F} C^2}{\mathrm{R} T} \cdots\cdots\cdots\cdots\cdots\cdots \mathrm{Eq.\,S5}$$

Therefore, the requirements to obtain TOF values using Eq. S5 are as follows:

(1) The rate constant of the reaction should be first-order to the concentration of the catalyst.

(2) i_p and $v^{1/2}$ should have a linear relationship to follow the Randles-Sevcik equation.
(3) i_{cat} should be independent to scan rates to obtain a purely kinetic condition.
(4) The amount of the substrate should be large enough to obtain a TOF (k_{cat}) value as a pseudo first-order rate constant.

The condition to satisfy these requirements for the catalyst was determined by several electrochemical measurements shown below.
(ii) Determination of a Rate Law
As mentioned in the previous section, the determination of a rate law is required for the calculation of the k_{cat}. i_{cat} values were measured at various concentrations of **1** in the presence of excess amount of water. As depicted in Figure 13, i_{cat} values exhibit a linear relationship with [cat] when [cat] is in the range of 0.05-0.2 mM, indicating that the rate law for O_2 evolution catalysed by **1** can be expressed by using a pseudo first-order rate constant, k_{cat}, as $d[O_2]/dt = k_{cat}$ [cat]. Therefore, Eq. S5 is applicable to obtain the TOF (k_{cat}) value of this system.

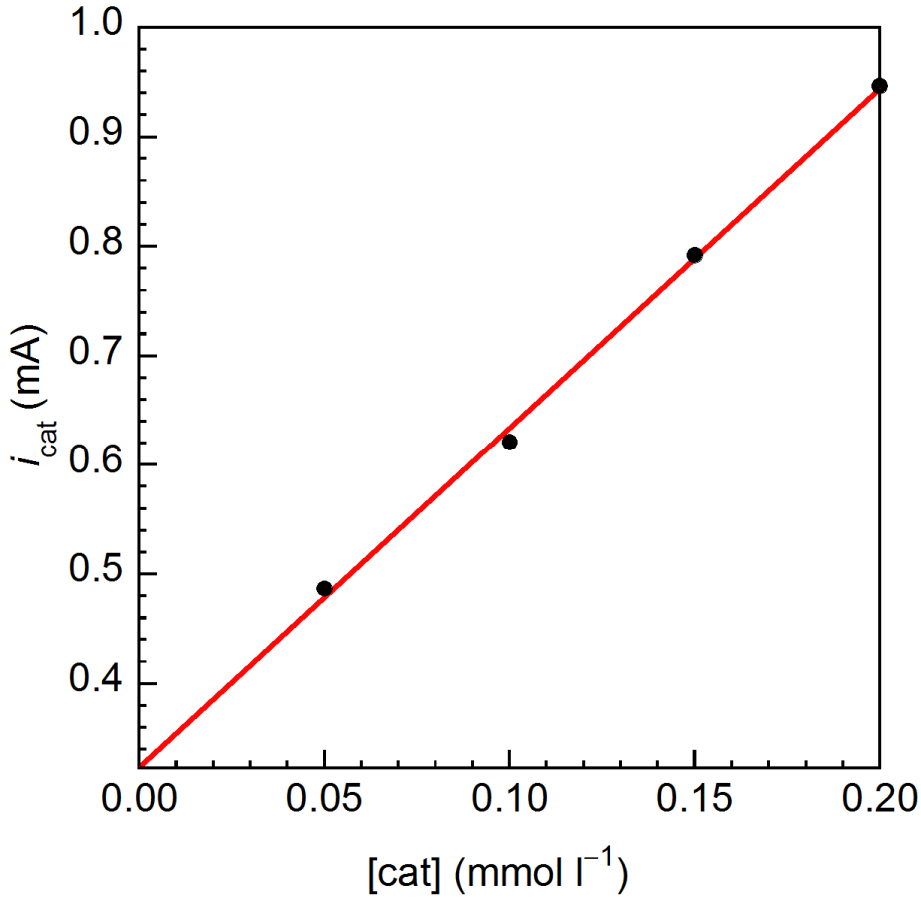

Figure 13. A plot of i_{cat} *vs.* [cat]. Measurements were performed in acetonitrile with 0.1 M Et_4NClO_4 as the supporting electrolyte at a scan rate of 2.0 V s^{-1} in an acetonitrile/water (10 : 1) mixed solution under Ar atmosphere. Electrodes: working, GC; auxiliary, Pt; reference, Ag/Ag^+.

(iii) Electrochemical Analysis of **1** in the Absence of Substrate

Calculations for k_{cat} require the measurement of i_p for the catalyst in the absence of substrate to confirm the reversibility of the redox process. As shown in Eq. S3, i_p has a linear relationship with $v^{½}$ when the redox process is reversible. In this study, the i_p values of the one-electron redox process of $Fe^{III}_5/Fe^{II}Fe^{III}_4$ were plotted against $v^{½}$, as shown in Figure 14. A linear relationship between i_p and $v^{½}$ was obtained when v is in the range of 0.2-2.6 V s^{-1}, indicating that the electron transfer rate of the redox couple is rapid enough to exhibit reversibility.

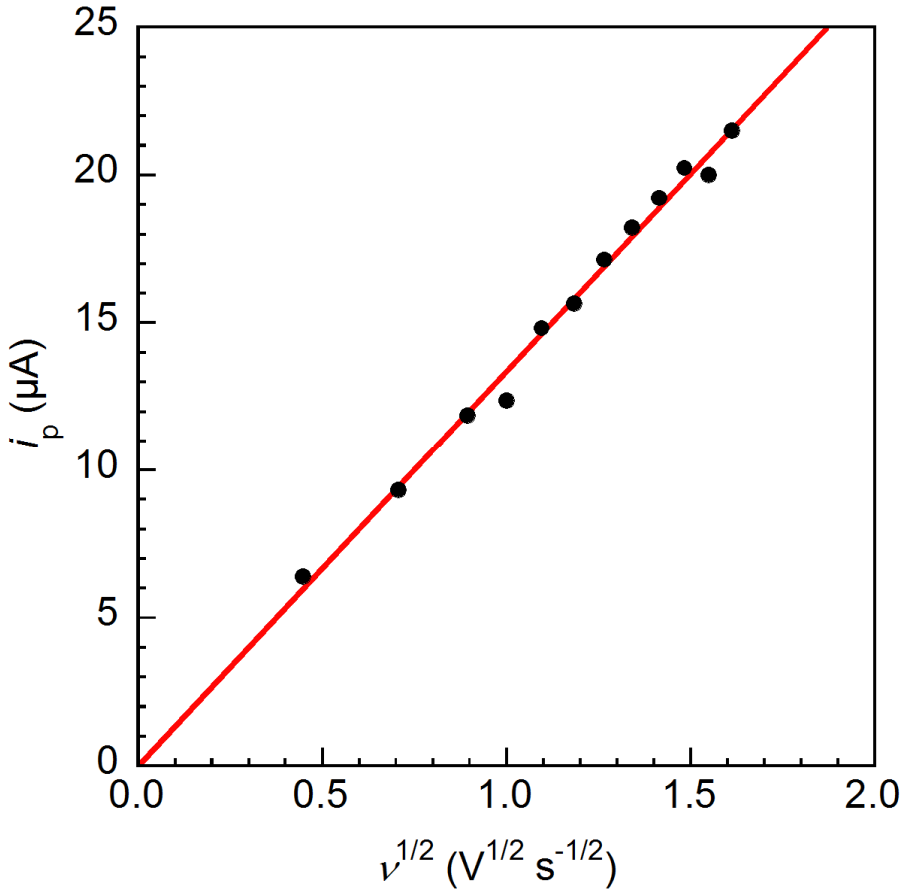

Figure 14. A plot of i_p *vs.* $v^{½}$. Measurements were performed in acetonitrile solution of **1** (0.2 mM) with Et_4NClO_4 (0.1 M) as the supporting electrolyte under Ar atmosphere. Electrodes: working, GC; auxiliary, Pt; reference, Ag/Ag^+. The original voltammograms are shown in Figure 15 and the numerical data are listed in Table 4.

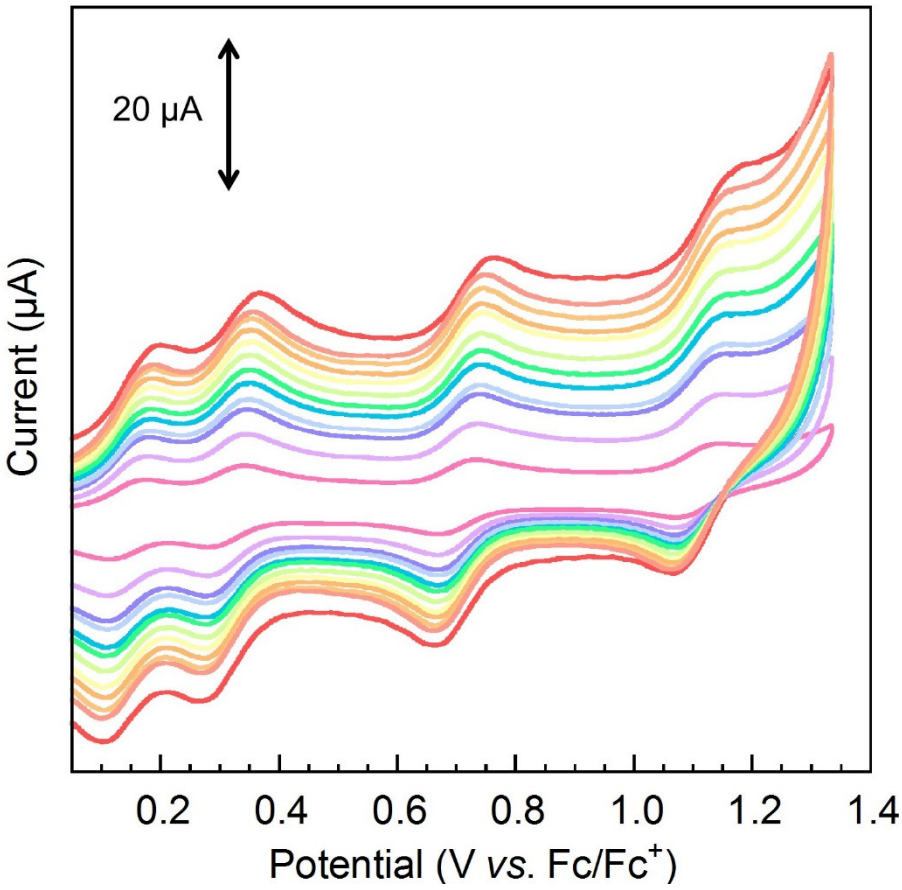

Figure 15. Cyclic voltammograms of **1** in the absence of water at various scan rates**.** Measurements were performed in acetonitrile solution of **1** (0.2 mM) with Et_4NClO_4 (0.1 M) as the supporting electrolyte under Ar atmosphere. Electrodes: working, GC; auxiliary, Pt; reference, Ag/Ag^+. A plot of i_p *vs.* $v^{½}$ is shown in Figure 14 and the numerical data are listed in Table 4.

(iv) Electrochemical Analysis of **1** in the Presence of Substrate

The scan rates to obtain the purely kinetic condition were determined by cyclic voltammetry at various scan rates. As shown in Figure 16 and Figure 17, constant limiting currents were observed when the scan rate is in the range of 1.6-2.6 V s^{-1}.

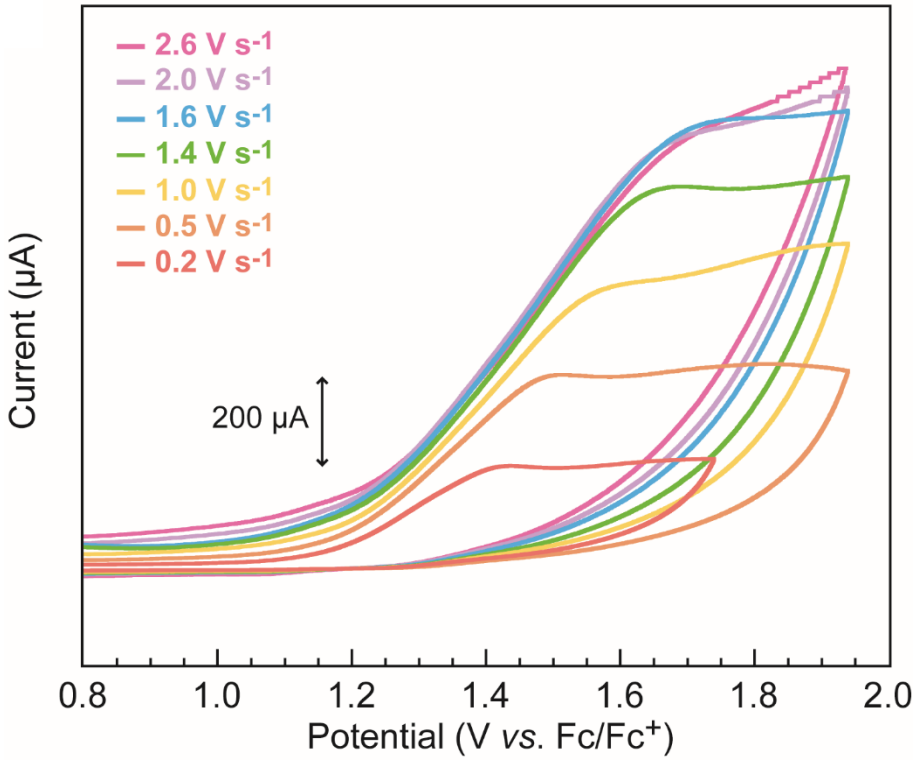

Figure 16. CV of **1** (0.2 mM) in acetonitrile/water (10 : 1) mixed solution with Et_4NClO_4 (0.1 M) at scan rates of 0.2 to 2.6 V s^{-1}. For the numerical data, see Table 4.

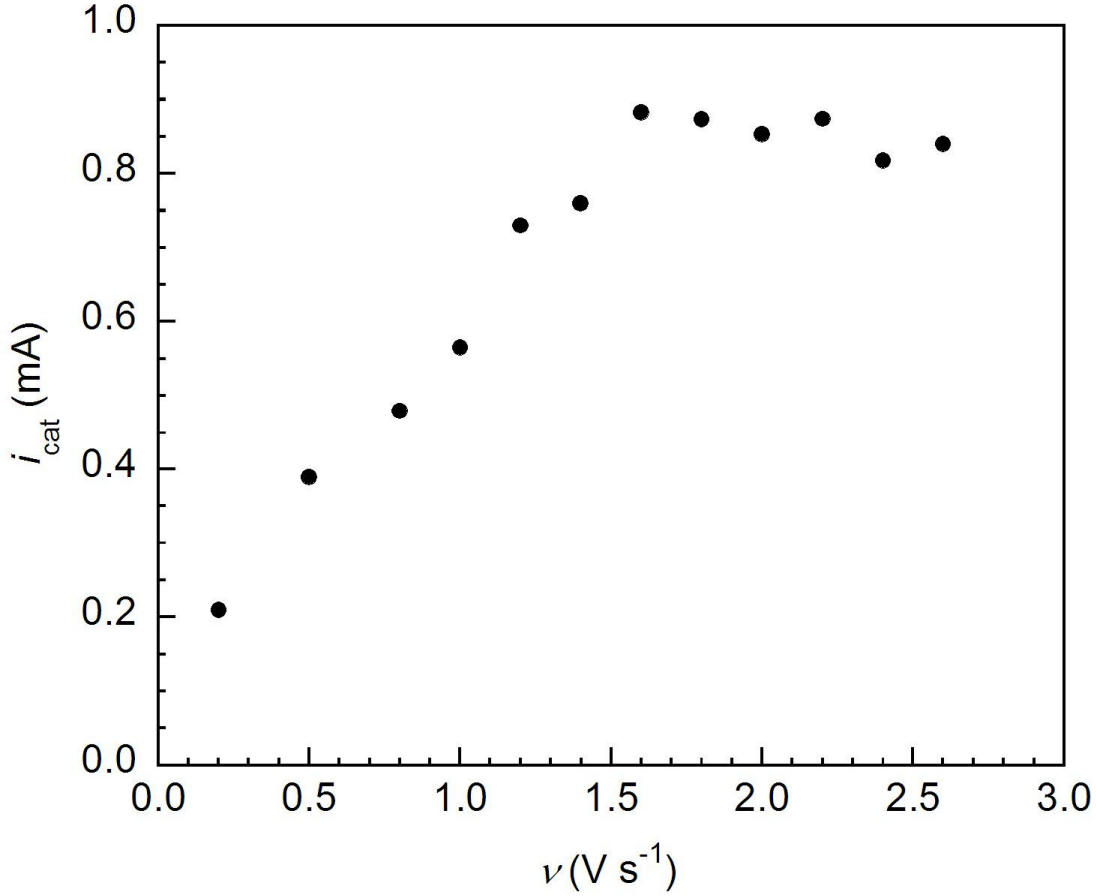

Figure 17. A plot of i_{cat} *vs.* ν. Measurements were performed in acetonitrile/water (10 : 1) mixed solution of **1** (0.2 mM) with Et_4NClO_4 (0.1 M) as the supporting electrolyte under Ar atmosphere. Electrodes: working, GC; auxiliary, Pt; reference, Ag/Ag^+. The numerical data are listed in Table 4.

Similarly, the constant limiting currents were observed when the concentration of water is higher than 2.6 mM, indicating that the amount of the substrate is large enough to reach the purely kinetic condition (Fig. 18).

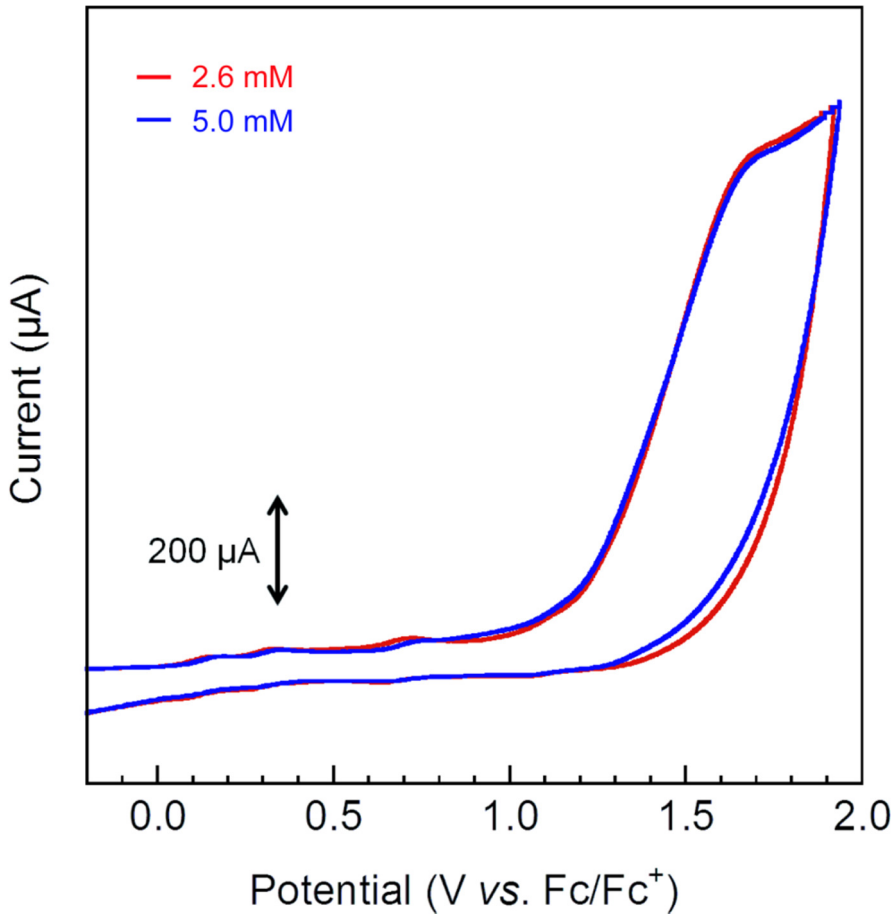

Figure 18. Cyclic voltammograms of **1** in acetonitrile (0.2 mM) with 0.1 M Et_4NClO_4 as the supporting electrolyte in the presence of H_2O at a scan rate of 2.0 V s^{-1} under Ar atmosphere. The CVs measured in acetonitrile/water (20 : 1, the concentration of water : 2.6 mM, red line) and acetonitrile/water (10 : 1, the concentration of water : 5.0 mM, blue line), respectively.

(v) Determination of TOF Value for **1**

Under the conditions in which **1** exhibits the purely kinetic behaviours, a TOF value was determined. As shown in Figure 19, the plot of i_{cat}/i_p against $v^{-½}$ shows a linear relationship and the slope was found to be 62.4. The TOF value of the reaction was determined to be 1,900 s^{-1} using Eq. S5. The values of scan rate, i_{cat}/i_p and $v^{-½}$ at each point are listed in Table 4.

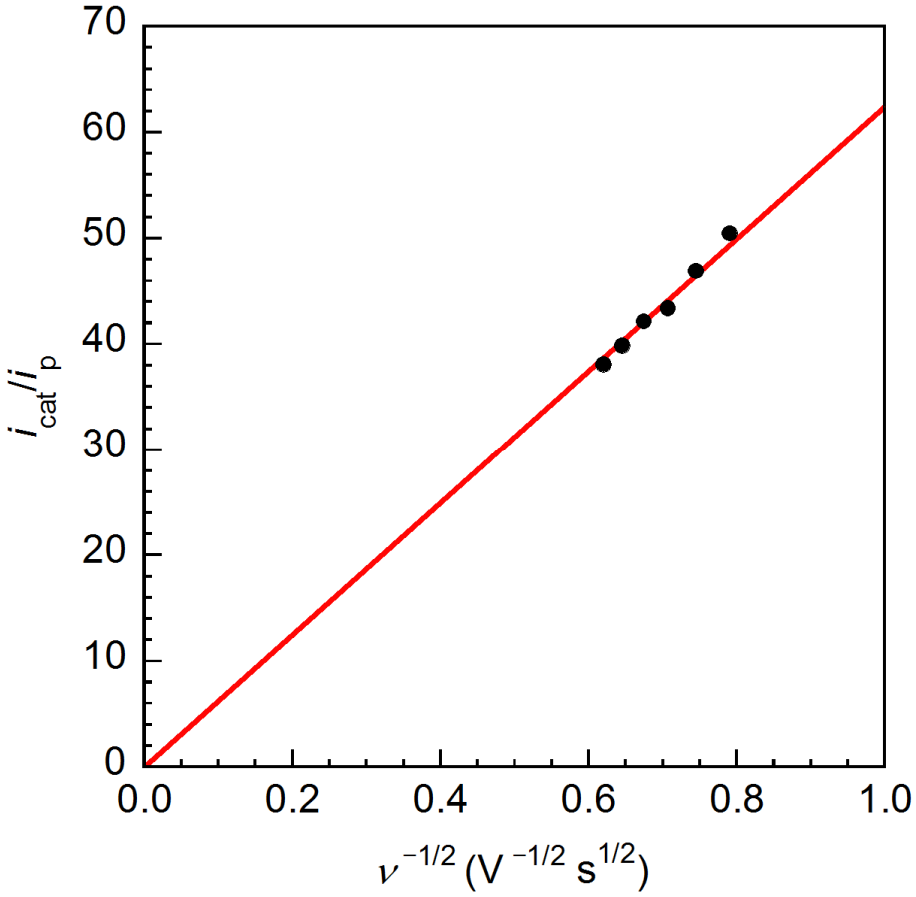

Figure 19. A plot of the ratio of i_{cat} to i_p as a function of the negative root of the scan rate. Measurements were performed in acetonitrile (for i_p) or in acetonitrile/water (10 : 1) mixed solution (for i_{cat}), in the presence of 0.1 M Et_4NClO_4 as the supporting electrolyte under Ar atmosphere. Electrodes: working, GC; auxiliary, Pt; reference, Ag/Ag^+. The numerical data are listed in Table 4.

The TOF value determined according to Eq. 1 was also supported by the rough estimation of the amount of O_2 evolved in the controlled potential electrolysis (Fig. 7). Based on the assumption that the thickness of the reaction-diffusion layer adjacent to the electrode surface (μ) is on the order $\mu \approx \sqrt{D/k_{\mathrm{cat}}}$ (ref 30), the TOF value was estimated to be *ca.* 140 to 1,400 s^{-1}, and the TON value was estimated to be *ca.* 1,000,000 to 10,000,000 for 120 min. These TOF and TON values indicate the substantial efficiency and robustness of **1** as a molecular catalyst for water oxidation.

Table 4. Summary of the numerical data in the electrochemical measurements. Plots of i_p *vs.* $v^{½}$, i_{cat} *vs.* v, and i_{cat}/i_p *vs.* $v^{-½}$ are shown in Figure 14, Figure 17, and Figure 19, respectively.

v (V s^{-1})	$v^{1/2}$ ($V^{1/2}$ $s^{-1/2}$)	$v^{-1/2}$ ($V^{-1/2}$ $s^{1/2}$)	i_{cat} (μA)	i_p (μA)	i_{cat}/i_p
0.20	0.447	2.236	202.81	6.39	–
0.50	0.707	1.414	380.28	9.32	–
0.80	0.894	1.118	468.34	11.86	–
1.00	1.000	1.000	553.44	12.36	–
1.20	1.095	0.913	715.38	14.82	–
1.40	1.183	0.845	743.95	15.65	–
1.60	1.265	0.791	865.06	17.14	50.47
1.80	1.342	0.745	855.07	18.23	46.90
2.00	1.414	0.707	834.07	19.23	43.37
2.20	1.483	0.674	853.46	20.24	42.17
2.40	1.549	0.645	797.90	20.00	39.90
2.60	1.612	0.620	818.51	21.49	38.09

Table 5. Comparison of TOF values between molecular catalysts for water oxidation

Catalyst	TOF (s^{-1})[a]	Oxidant	Reference
Fe catalysts			
1	1,900	electrochemical[b]	This work
1	140-1,400	electrochemical[c]	This work
$Fe(TAML\text{-}F_2\text{-}Cl_2)OH_2$	>1.3	Ce^{IV}	5
$[Fe(OTf)_2(mcp)]$	0.06 (0.23)	$NaIO_4$ (Ce^{IV})	8
$[Fe^{III}(dpaq)(H_2O)]^{2+}$	0.15	electrochemical[b]	14
Ru catalysts			
$[Ru_4(\mu\text{-}O)_4(\mu\text{-}OH)_2(H_2O)_4(\gamma\text{-}SiW_{10}O_{36})_2]^{10-}$	0.13	Ce^{IV}	31
$[Ru(EtO\text{-}terpy)(bpy)OH_2]^{2+}$	0.11	Ce^{IV}	32
$[\{[4,4'\text{-}(HO)_2OPCH_2]_2bpy\}_2\text{-}Ru^{II}(bpm)Ru^{II}(Mebimpy)(OH_2)]^{4+}$	0.6	electrochemical[d]	33
$RuL(pic)_2$	0.36	$h\nu$, $[Ru(bpy)_3]^{2+}$	34
dinuclear Ru complex	0.26	$h\nu$, $[Ru(dcbpy)_2(bpy)]^{2+}$	35
dinuclear Ru complex	1.2	Ce^{IV}	36
$[Ru(Mebimpy)(bpy)(OH_2)]^{2+}$	~1	electrochemical[b]	37
$[Ru(tpy)(Mebim\text{-}py)(OH_2)]^{2+}$	~3.6	electrochemical[b]	38
$[Ru(bda)(isoq)_2]$	303	Ce^{IV}	9
$[Ru_4(\mu\text{-}O)_4(\mu\text{-}OH)_2(H_2O)_4(\gamma\text{-}SiW_{10}O_{36})_2]^{10-}$	280	flash photolysis, $[Ru(bpy)_3]^{2+}$	39
$Ru(L1)_2(pic)_3$	7.4	$[Ru(bpy)_3]^{3+}$	40
$Ru^{II}(\kappa^3\text{-}bda)(DMSO)(L2)_2$	176.5	Ce^{IV}	41
$[Ru(bpb)(pic)_2]^+$	0.12	$[Ru(bpy)_3]^{3+}$	42
$Ru(bda)(isoq)_2$	14,000[e]	electrochemical[b]	43
mixture of $[Ru(tda)(py)_2]^{2+}$ and $[Ru(O)(tda)(py)_2]$	50,000	electrochemical[b]	15
Co catalysts			
$[Co_4(H_2O)_2(PW_9O_{34})_2]^{10-}$	>5	$[Ru(bpy)_3]^{3+}$	6
$[Co^{II}(Py5)(OH_2)]^{2+}$	~79	electrochemical[b]	44
$CoH^{\beta F}CX\text{-}CO_2H$	0.81	electrochemical[d]	45
$[Co_2Mo_{10}O_{38}H_4]^{6-}$	0.16	$h\nu$, $[Ru(bpy)_3]$	46
CoTPPS	0.17	$h\nu$, $[Ru(bpy)_3]$	47
$Co(TDMImP)(OH_2)(OH)$	1,400	electrochemical[b]	13

Table 4 (Continued)

Catalyst	TOF (s^{-1})	Oxidant	Reference
Cu catalysts			
$Cu(bpy)_2(OH)_2$	~100	electrochemical[b]	10
$[(TGG^{4-})Cu^{II}–OH_2]^{2-}$	33	electrochemical[b]	48
Ir catalysts			
$[\{(4,4'\text{-}HOOC)_2bpy\}Ir^{III}Cp^*(OH_2)]^{2+}$	6.7	electrochemical[d]	49
$Cp^*Ir(NHC)Cl_2$	0.31	$NaIO_4$	50
Mn catalysts			
$[(terpy)(H_2O)Mn(O)_2Mn(H_2O)(terpy)]^{3+}$	0.67	HSO^{5-}	51

[a] TOF values cannot be directly compared without recognising that reaction conditions such as solvent, oxidant and applied potential differ. [b] estimated from cyclic voltammograms, [c] obtained as a roughly estimated value by considering the thickness of the reaction-diffusion layer during the controlled potential electrolysis. [d] bulk electrolysis [e] obtained based on $[OH]^-$ at pH 12.2

TAML = -tetraamido macrocyclic ligand, mcp = *N,N'*-dimethyl-*N,N'*-bis(2-pyridylmethyl)-cyclohexane-1,2-diamine, dpaq = 2-[bis(pyridine-2-ylmethyl)]amino-*N*-quinolin-8-yl-acetamido, terpy = 2,2':6',2"-terpyridine, bpy = 2,2'-bipyridine, bpm = 2,2'-bipyrimidine, Mebimpy = 2,6-bis(1-methylbenzimidazol-2-yl)pyridine, H_2L = 2,2'-bipyridine-6,6'-dicarboxylic acid, pic = 4-picoline, dcbpy = 2,2'-bipyridine-4,4'-diethylcarboxylate, Mebim-py = 3-methyl-1-pyridyl benzimidazol-2-ylidene, bda = 2,2'-bipyridine-6,6'-dicarboxylate, isoq = isoquinoline, L1 = 2-(2-hydroxyphenyl)- 1H-benzo[d]imidazol-7-ol, L2 = 5-bromo-*N*-methylimidazole, H_2bpb= *N,N'*-1,2-phenylene-bis(2-pyridine-carboxamide), Py5 = 2,6-(bis(bis-2-pyridyl)-methoxymethane)pyridine, tda = [2,2':6',2"-terpyridine]-6,6"-dicarboxylate, $H^{\beta F}CX\text{-}CO_2H$ = 2,3,7,8,12,13,17,18-Octafluoro-10-(4-(5-Hydroxycarbonyl-2,7-di-tert-butyl-9,9-dimethyl-xanthene))-5,15-bis(pentafluorophenyl)corrole, TPPS = meso-tetra(4-sulfonatophenyl)porphyrinato, TDMImP = 5,10,15,20-tetrakis-(1,3-dimethylimidazolium-2-yl), TCG = triglycylglycine, Cp* = pentamethylcyclo pentadiene, NHC = 3-methyl-1-(1-phenylethyl)-imdazoline-2-ylidene, H_2bpb = *N,N'*-1,2-phenylene-bis(2-pyridine-carboxamide)

Section 2.

Water oxidation mechanism of the pentanuclear iron catalyst

In this section, the reaction mechanism leading to O_2 from water is discussed based on the combination of DFT calculations and experimental results (Spectroscopic Characterization, Electrochemical mesurments and Mössbauer spectroscopy). Figure 20 illustrates a possible catalytic cycle for the generation of O_2 mediated by **1**. The electrochemical measurement revealed a four-step, one-electron oxidation from the initial $Fe^{II}_4Fe^{III}$ state (**S0** in Fig. 20) to provide the Fe^{III}_5 state (**S4**). Note that water attack to the $Fe^{II}_4Fe^{III}$ (**S0**), $Fe^{II}_3Fe^{III}_2$ (**S1**), $Fe^{II}_2Fe^{III}_3$ (**S2**), and $Fe^{II}Fe^{III}_4$ states (**S3**) can be excluded because the oxidation potentials for these states remained unchanged upon the addition of water (Fig. 5, P. 54). The pH dependence of the CVs showed no change in the onset potential of water oxidation (Fig. 21), indicating that the water attack of the **S4** state does not involve proton-coupled electron transfer. Therefore, subsequent insertion of a water molecule to the **S4** state results in the formation of the $Fe^{III}_5(OH_2)$ species with a hexa-coordinated Fe^{III} ion at the triangle core (**A** in Fig. 20).

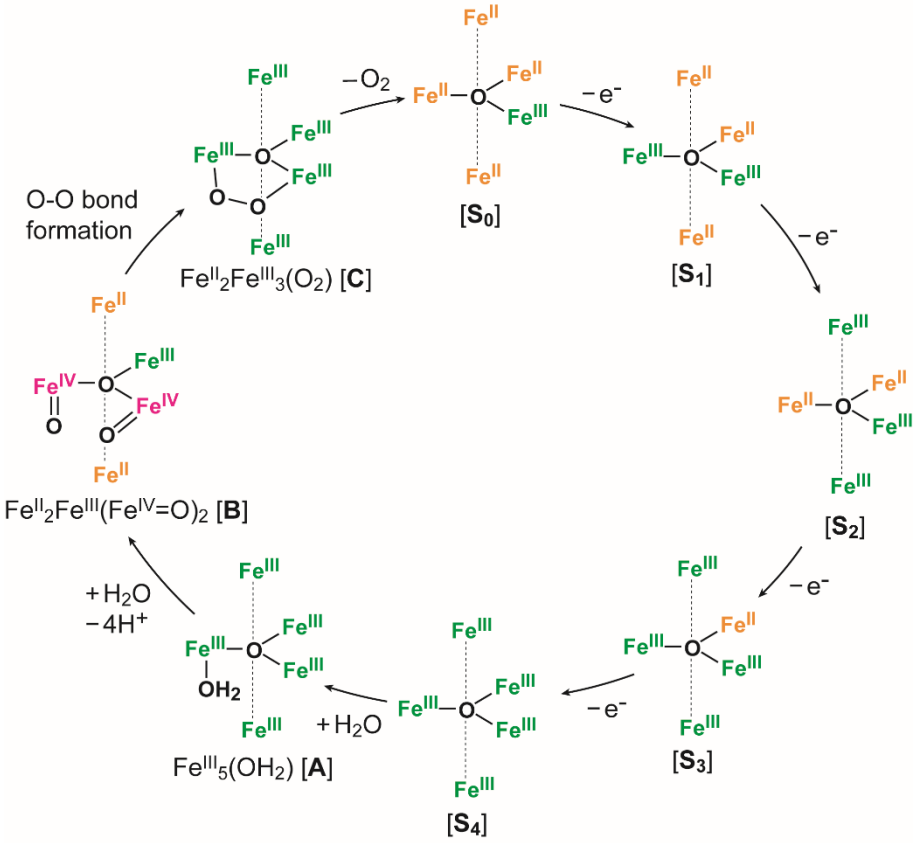

Figure 20. Mechanism of O_2 evolution from water catalyzed by **1**. One water molecule reacts with the **S**$_4$ state formed by the four-electron oxidation of the **S**$_0$ state. Further reaction with an additional water molecule and the deprotonation of the coordinated water molecules afford the adjacent two metal-oxo moieties in one molecule, which promotes rapid intramolecular O-O bond formation to evolve O_2.

Electrochemical Measurements at Various pH

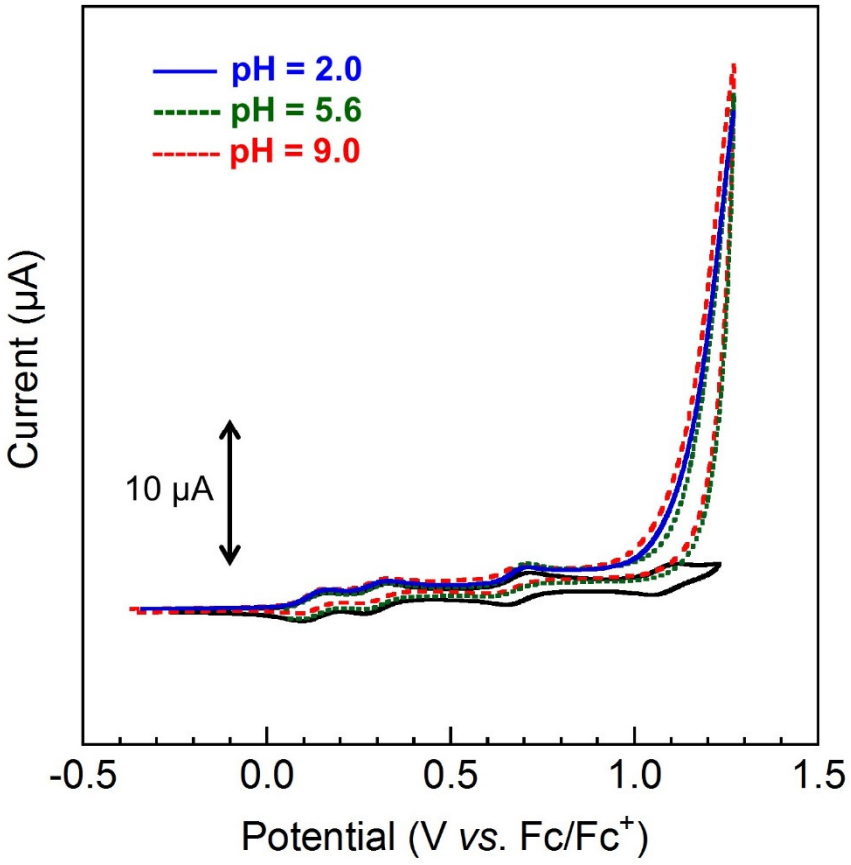

Figure 21. CVs of **1** (0.2 mM) in acetonitrile solutions with Et_4NClO_4 (0.1 M) at a scan rate of 10 mV s^{-1}, in the presence of 5 M of H_2O at various pH. The CVs at various pH showed no change of the onset potential of water oxidation. Overpotentials for water oxidation mediated by **1** are estimated to be 0.52 V at pH = 2.0 and 0.93 V at pH = 9.0.

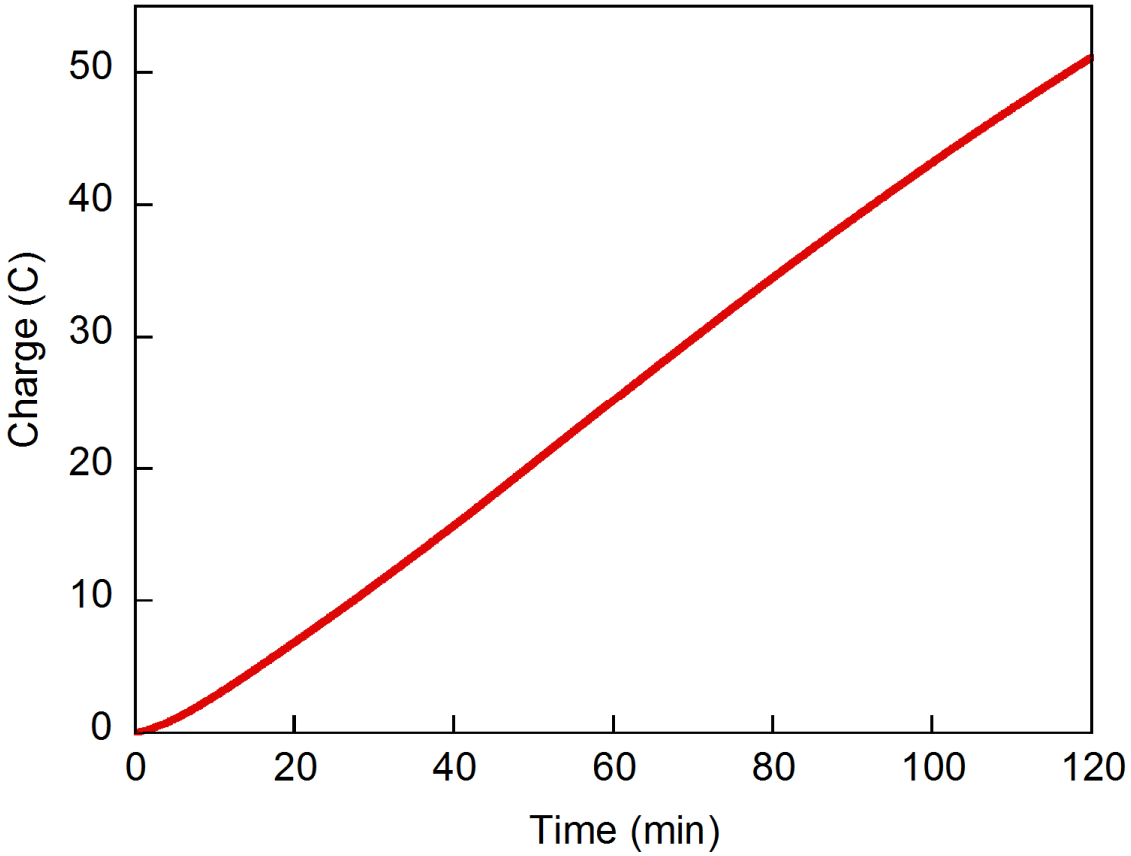

Figure 22. The result of the electrolysis in 0.2 mM of **1** with borate buffer (the initial pH was 7.8). Condition: acetonitrile/water (10 : 1) mixed solution with borate buffer (0.14 mM) and Et_4NClO_4 (0.1 M) at a potential of 1.42 V *vs.* Fc/Fc^+. The linear profile of the charge *vs*. time plot was obtained and is similar to the result of electrolysis without buffer (Fig. 7, P. 57). The Faradaic efficiency was 97%, which was comparable to the result obtained by the electrolysis with the initial pH of 4.8 (without borate buffer, see also Table 3, P. 57). These results indicate that the pH of the solution does not affect the catalytic activity.

Spectroscopic Characterisation of 1 in Various Oxidation States

(i) UV-vis Absorption Spectroscopy

The oxidized species of the iron catalyst were generated by electrochemical and chemical oxidation and characterized spectroscopically. The reaction conditions of the experiments are as follows.

(a) Spectro-electrolysis: UV-Vis absorption spectral changes before and after the electrolysis of a 0.5 mM solution of **1**$(BF_4)_3$ were measured in CH_3CN containing 0.1 M TBAP at 293 K.

(b) Chemical Oxidation: UV-Vis absorption spectral changes upon the chemical oxidation of a 0.05 mM solution of **1**$(BF_4)_3$ were measured in CH_3CN at 293 K using tris(4-bromophenyl)ammoniumyl hexachloroantimonate (Magic blue (**MB**), E_{ox} = 0.67 V *vs*. Fc/Fc^+ [52]) and tris(2,4-dibromophenyl) ammoniumyl hexachloroantimonate (Magic green (**MG**), E_{ox} = 1.14 V *vs*. Fc/Fc^+ [52]) as chemical oxidants.

Upon the electrochemical oxidation of **1**$(BF_4)_3$, the UV-vis absorption spectra exhibited a four-step change, and successive oxidation of the complex from the **S_0** to the **S_4** state (Figs 23a-25a, 26) was observed. The changes in the UV-vis absorption spectra upon the step-wise addition of the chemical oxidants (**MB** or **MG**) were also measured. As shown in Figures 23b-25b, the three-step change with isosbestic points was observed. This result indicates the sequential formation of the **S_1-S_3** states by chemical oxidation. The spectra of the **S_1-S_3** states obtained by electrochemical and chemical oxidation are consistent with each other, whereas the formation of **S_4** was not confirmed by the chemical oxidation.
As shown in Figure. 23, the complex in **S_0** state exhibits the intense band around 400 nm, which attributes to the MLCT transition of the Fe(II) ion in low spin state. Upon the oxidation from **S_0** to **S_1**, only the slight change in the UV-vis spectra was observed, which indicates the oxidation of the high-spin Fe^{II} ion in the first step. In contrast, the large decrease of the band around 400 nm, was observed upon the oxidation from **S_1** to **S_2** (Fig. 24), suggesting the oxidation of the low-spin Fe^{II} ion in the second step. Third oxidation step from **S_2** to **S_3** resulted in the increase in the band around 550 nm (Fig. 25), and the decrease in the band around 550 nm was observed in the final oxidation step to generate **S_4** state (Fig. 26).

$S_0 \rightarrow S_1$

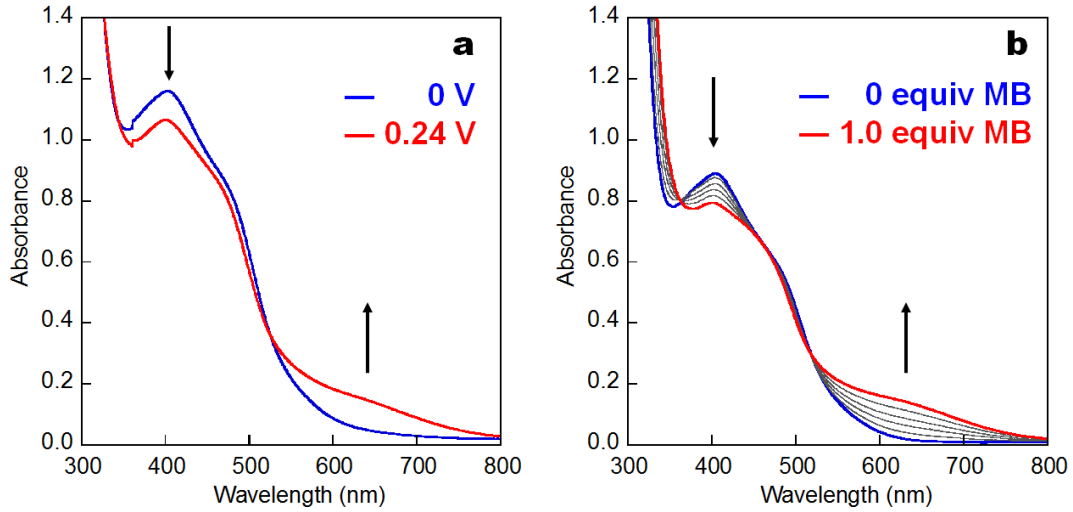

Figure 23. UV-vis absorption spectra changes from **S₀** (blue line) to **S₁** (red line) state of **1**: a) generation of **S₁** state after the electrolysis at 0.24 V (*vs*. Fc/Fc^+); b) conversion of **S₀** to **S₁** upon sequential addition of **MB** (total 1 equiv.).

$S_1 \rightarrow S_2$

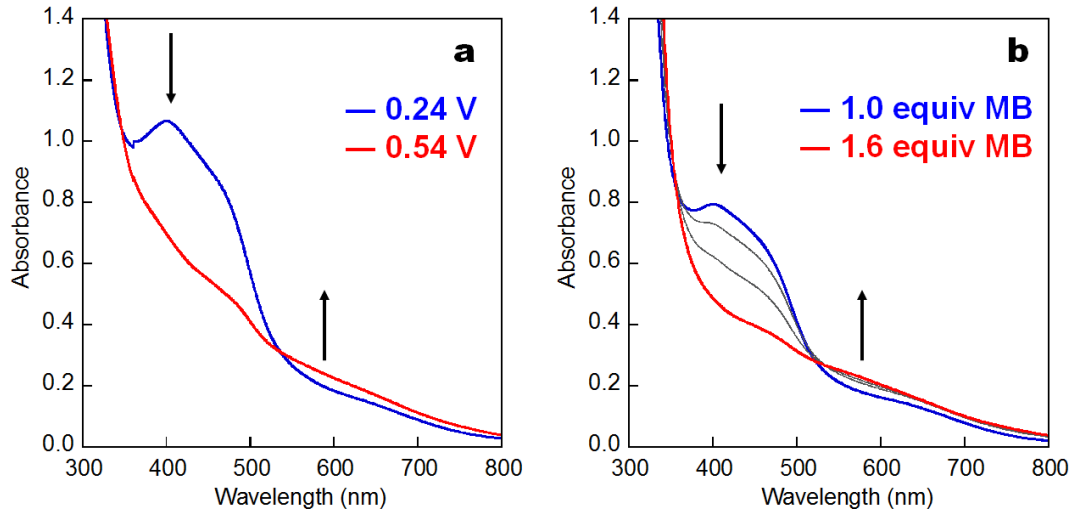

Figure 24. UV-vis absorption spectra changes from **S₁** (blue line) to **S₂** (red line) state of **1**: a) generation of **S₂** state after the electrolysis at 0.54 V (*vs*. Fc/Fc^+); b) conversion of **S₁** to **S₂** using further addition of **MB**.

$S_2 \rightarrow S_3$

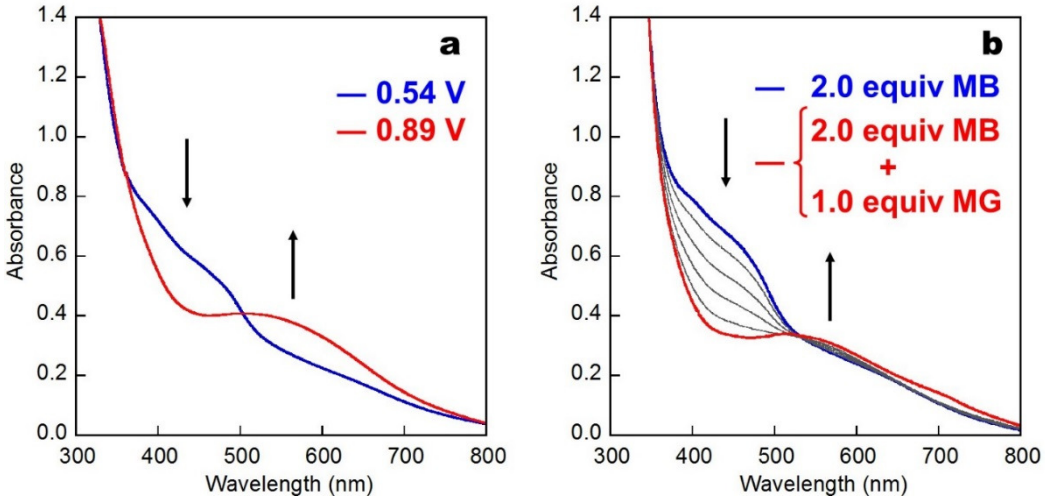

Figure 25. UV-vis absorption spectra changes from **S2** (blue line) to **S3** (red line) state of **1**: a) generation of **S3** state after the electrolysis at 0.89 V (*vs*. Fc/Fc^+); b) conversion of **S2** to **S3** using 1 equiv. of **MG** after the formation of **S2** by **MB**.

$S_3 \rightarrow S_4$

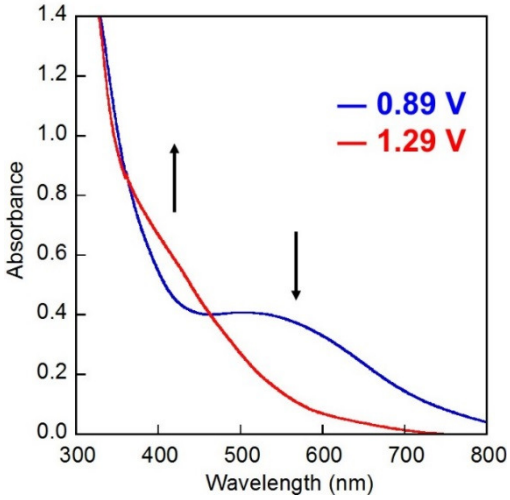

Figure 26. UV-vis absorption spectra changes from **S3** (blue line) to **S4** (red line) state of **1**: generation of **S4** state after the electrolysis at 1.29 V (*vs*. Fc/Fc^+).

(ii) Isolation of the Oxidized Species of **1**

The oxidized species of **1** (**S1** and **S2** states) were successfully isolated by the following procedure.

Synthesis of [{Fe^{II}(μ-L)$_3$}$_2$ Fe^{II}Fe$^{III}_2$ (μ-O)](BF$_4$)$_4$·9H$_2$O (S$_1$).

To a solution of **1**$(BF_4)_3$·$7H_2O$ (0.007 mmol, 15 mg) in acetonitrile (4 mL) was added 1 equiv of tris(4-bromophenyl)ammoniumyl hexachloroantimonate (**MB**, 0.007 mmol, 6.1 mg). The reaction mixture was stirred at room temperature for 20 min, followed by the addition of saturated aqueous solution of $NaBF_4$ (0.3 mL) and stirred further for another 10 min. The resulting dark brown solution was subjected to slow vapour diffusion in diethyl-ether to provide black crystals of **1**$(BF_4)_4$·$9H_2O$. The crystals were collected by filtration and dried under vacuum. Yield 12.5 mg (78 %). Elemental analysis Calcd. for **1**$(BF_4)_4$·$9H_2O$: $C_{78}H_{72}F_{16}Fe_5N_{24}O_{10}B_4$: C, 43.94; H, 3.40; N, 15.77%. Found: C, 43.65; H 3.11; N 15.76%. ESI-TOF MS (positive ion, acetonitrile): m/z: 404.5 [{Fe^{II}(μ-**L**)$_3$}$_2$Fe^{II}Fe$^{III}_2$(μ-O)]$^{4+}$.

Synthesis of [{Fe^{III}(μ-L)$_3$}$_2$ Fe$^{II}_2$Fe^{III} (μ-O)](BF$_4$)$_5$·10H$_2$O (S$_2$)

To a solution of **1**$(BF_4)_3$·$7H_2O$ (0.01 mmol, 20 mg) in acetonitrile (5 mL) was added tris(4-bromophenyl)ammoniumyl hexachloroantimonate (**MB**, 0.022 mmol, 17.85 mg). The reaction mixture was stirred for 30 min at room temperature, followed by the addition of saturated aqueous solution of $NaBF_4$ (0.5 mL) and stirred further for another 10 min. The resulting dark brown solution was subjected to slow vapour diffusion in diethyl-ether to provide black crystals of **1**$(BF_4)_5$·$10H_2O$. The crystals were collected by filtration and dried under vacuum. Yield 14.2 mg (65 %). Elemental analysis Calcd. for **1**$(BF_4)_5$·$10H_2O$: $C_{78}H_{74}F_{20}Fe_5N_{24}O_{11}B_5$: C, 41.88; H, 3.33; N, 15.03%. Found: C, 41.64; H 3.03; N 14.82%. ESI-TOF MS (positive ion, acetonitrile): m/z: 324.4 [{Fe^{III}(μ-**L**)$_3$}$_2$Fe$^{II}_2$Fe^{III}(μ-O)]$^{5+}$.

(iii) ^{57}Fe Mössbauer spectra of S_1 and S_2 states

The isolated oxidized complexes of **1** were characterized by ^{57}Fe Mössbauer spectroscopy. The spectrum of $\mathbf{S_1}$ consists of three quadrupole doublets with relative peak areas of 2:2:1, which correspond to low-spin Fe^{II} ions (isomer shift (IS) = 0.43 mm s^{-1}, quadrupole splitting (QS) = 0.28 mm s^{-1}), high-spin Fe^{III} ions (IS = 0.49 mm s^{-1}, QS = 1.72 mm s^{-1}) and high-spin Fe^{II} ion (IS = 0.83 mm s^{-1}, QS = 2.89 mm s^{-1}), respectively (Fig. 27, and Table 6). These results suggest that the two iron centers at the apical positions are low-spin Fe^{II} ions and that the [$Fe_3(\mu_3$-O)] core is composed of two high-spin Fe^{III} ions and one high-spin Fe^{II} ion (Fig. 29b). In other words, the one-electron oxidation of the [$Fe_3(\mu_3$-O)] core of $\mathbf{S_0}$ affords $\mathbf{S_1}$ (Scheme 1). This result is consistent with the result of UV-vis absorption measurement (Fig. 23), which indicates the oxidation of the high-spin Fe^{II} ion in the first oxidation step.

The spectrum of $\mathbf{S_2}$ consists of three quadrupole doublets with relative peak areas of 2:2:1, which correspond to low-spin Fe^{III} ions (IS = 0.11 mm s^{-1}, QS = 1.37 mm s^{-1}), high-spin Fe^{II} ions IS = 0.81 mm s^{-1}, QS = 3.04 mm s^{-1}) and high-spin Fe^{III} ion (IS = 0.85 mm s^{-1}, QS = 1.18 mm s^{-1}), respectively (Fig. 28 and Table 7). These results suggest that the two iron centers at the apical positions are low-spin Fe^{III} ions and that the [$Fe_3(\mu_3$-O)] core is composed of two high-spin Fe^{II} ions and one high-spin Fe^{III} ion (Fig. 29c). Therefore, upon oxidation from $\mathbf{S_1}$ to $\mathbf{S_2}$, the two apical Fe^{II} ions are oxidized and the Fe^{III} ion in the [$Fe_3(\mu_3$-O)] core is reduced (Scheme 1). In other words, intramolecular electron transfer from the iron center at the apical position to the [$Fe_3(\mu_3$-O)] core proceeds during the oxidation process from $\mathbf{S_1}$ to $\mathbf{S_2}$. This result is also consistent with the result of UV-vis absorption measurement (Fig. 24), which indicates the oxidation of the low-spin Fe^{II} ion in the second oxidation step.

Scheme 1. Schematic illustration of $\mathbf{S_0}$-$\mathbf{S_2}$ states. The iron ions that undergo electron transfer in the first and second oxidation steps are marked with circles.

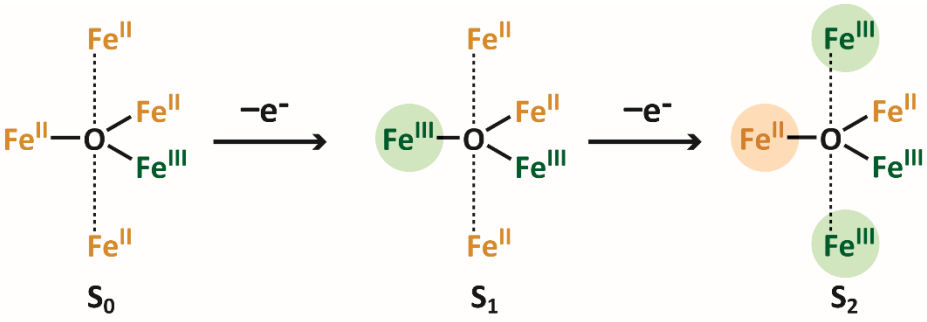

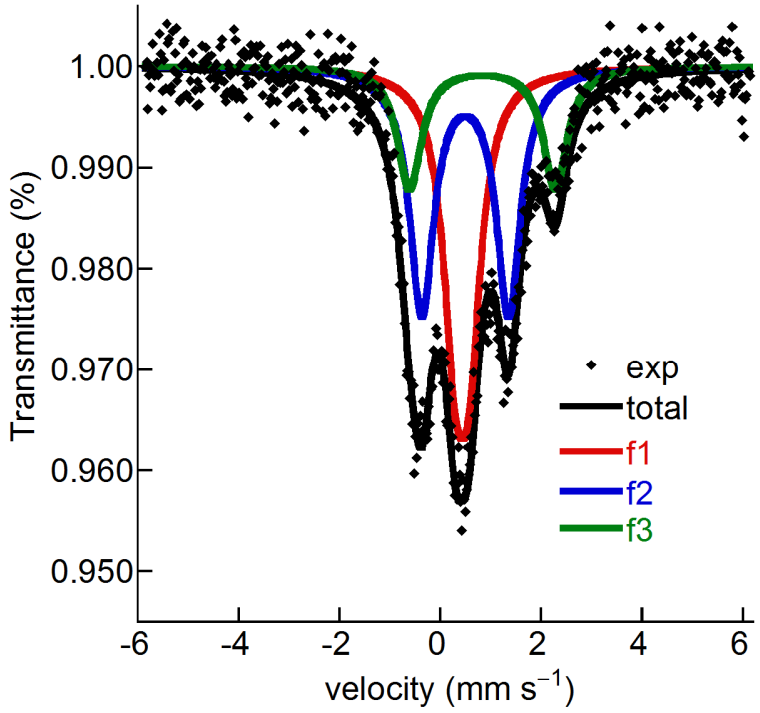

Figure 27. A ^{57}Fe Mössbauer spectrum of **S1** at 20 K.

Table 6. ^{57}Fe Mössbauer least-squares fitting parameters for **S1** at 20 K.

	f1	f2	f3
IS (mm s^{-1})	0.43	0.49	0.83
QS (mm s^{-1})	0.28	1.72	2.89
ratio (%)	38.6	40.9	20.5
assignment	Fe(II) LS	Fe(III) HS	Fe(II) HS

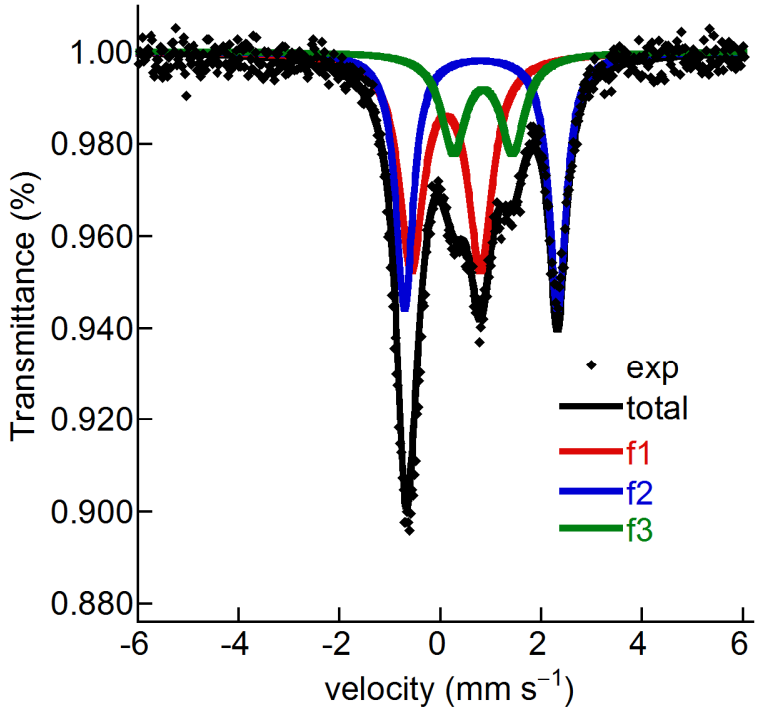

Figure 28. A ^{57}Fe Mössbauer spectrum of **S2** at 31 K.

Table 7. ^{57}Fe Mössbauer least-squares fitting parameters for **S2** at 31 K.

	f1	f2	f3
IS (mm s^{-1})	0.11	0.81	0.85
QS (mm s^{-1})	1.37	3.04	1.18
ratio (%)	42.9	37.4	19.7
assignment	Fe(III) LS	Fe(II) HS	Fe(III) HS

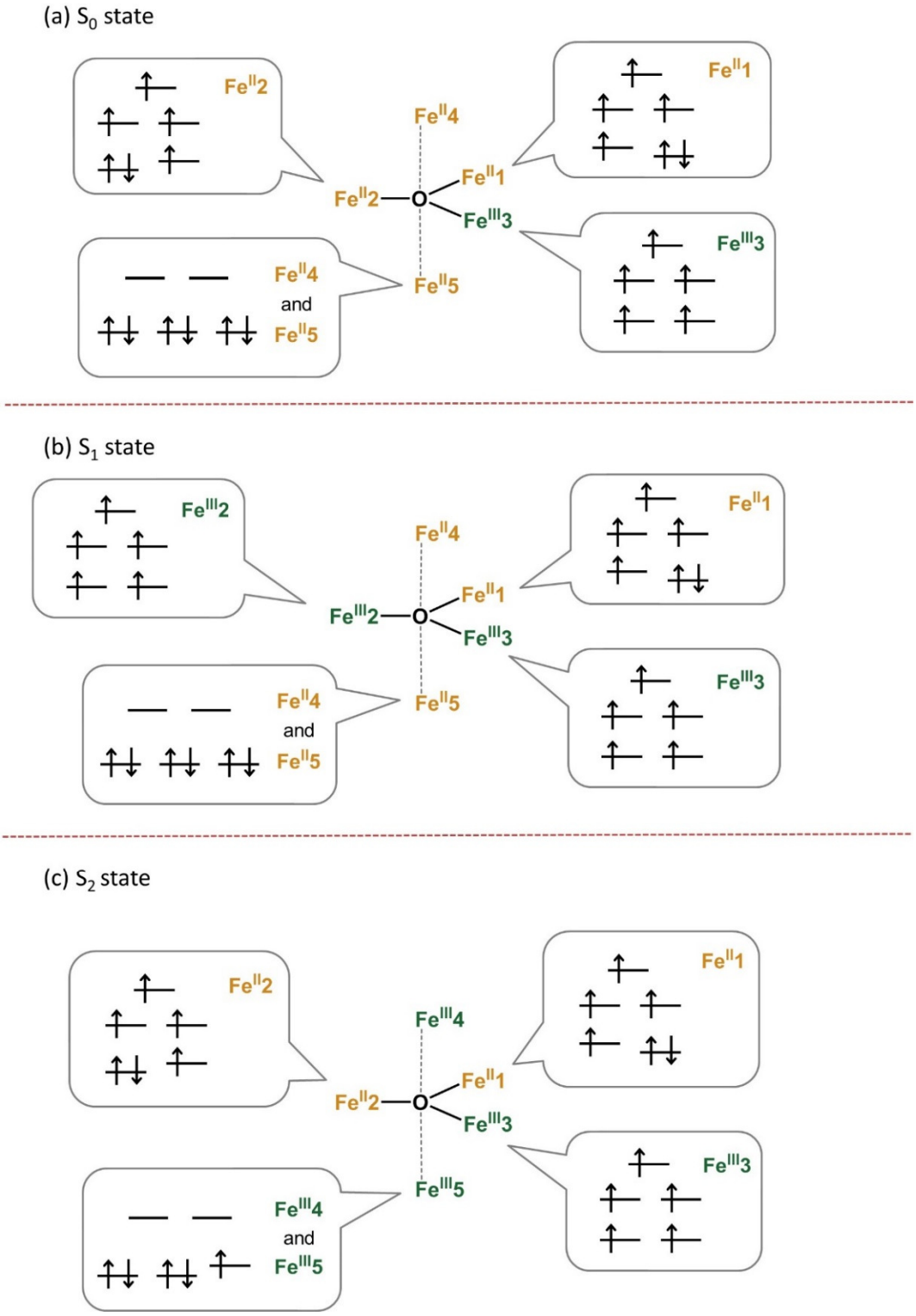

Figure 29. Electron configurations and oxidation states of Fe centers for (a) **S0**, (b) **S1**, and (c) **S2** determined by the UV- vis spectroscopy and the ^{57}Fe Mössbauer spectroscopy.

Computational details

Quantum chemistry calculations were performed on the pentanuclear iron complex (**1**) and its reaction intermediates using density functional theory (DFT). All the DFT calculations were carried out with the ORCA software package (versions 2.9.1 and 3.0.0) [53]. The following computational settings were used throughout all the calculations unless otherwise noted.

1. The scalar relativistic contracted versions of the def2-TZVP (Fe and O) and def2-SVP (C, N, and H) basis sets [54-55] were employed.
2. The hybrid B3LYP [56] and hybrid meta-GGA TPSSh functionals [57] were used for the exchange-correlation functionals in conjunction with Grimme's van der Waals corrections [58] (`VDW10` option in ORCA 2.9.1 or `D3ZERO` in 3.0.0), denoted B3LYP-D and TPSSh-D, respectively.
3. Scalar relativistic effects were included using the second-order Douglas-Kroll-Hess (DKH) Hamiltonian. [59]
4. The Coulomb integrals were evaluated by taking advantage of the RI approximation with the auxiliary def2-TZVP/J (Fe and O) and def2-SVP/J (C, N, and H) fitting basis sets [60]. For the hybrid density functional calculations, the RIJCOSX approximation [61] was used.
5. Tight SCF convergence criteria were adopted (`TightSCF` option in ORCA).
6. The total net charge of **1** for the $\mathbf{S}_n$ state (n = 0, 1,.., 4) was set to n + 3; for example, $\mathbf{1}^{7+}$ for $\mathbf{S}_4$.

Consideration of environmental effects is out of scope in the present theoretical investigation. For later convenience, the Fe and O atoms are labelled as FeX (X = 1,..,5) and OX (X = 1,2,3), as displayed in Figure 30.

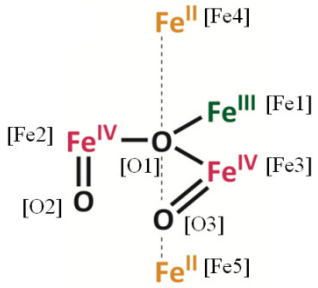

Figure 30. Labels of Fe ions and O atoms (Fe1,…,Fe5 and O1,…,O3 in […]) in case of **B** intermediate (taken from Fig. 20).

(i) Determination of the Reaction Pathway for Water Attack ($S_4 + H_2O \rightarrow A$)

Reaction pathways for the insertion of a single water molecule into the Fe^{III}_5 state (**S_4**) were explored. In the DFT calculations, the open-shell electronic structures in the Fe ions were treated with the high-spin unrestricted orbital approach (i.e., without use of spin polarisation). Increased numerical integration grids (`Grid6` option in ORCA) were used for the DFT calculations. Two types of open-shell spin states were considered, depending on the number of the resulting unpaired electrons at Fe4 and Fe5; these open-shell states are referred to as low-spin (LS) and high-spin (HS) states, respectively. Overall, pathway search was performed on the two types of spin states for **S_4**, denoted S4-LS, and S4-HS, which were obtained by setting the M_S parameter (total spin quantum number) to 18 and 26, respectively.

Table 8 shows Mulliken spin populations of the five Fe ions along with total energies for the optimised structures of **1** (without water). One of the notable differences between HS and LS was found in the bond distance between Fe4 (or Fe5) and the N atom of the pyridyl ligand of **L**: R(Fe4-N) = 2.01 Å (S4-LS), and 2.18 Å (S4-HS). In addition, LS was shown to be lower in energy than HS for the given oxidation state.

Table 8. | Mulliken spin populations of Fe ions and total energies obtained with the TPSSh-D functional for the pentanuclear iron complex (**1**) with the S4-LS and S4-HS states (without water).

	charge	*Ms*	Fe1	Fe2	Fe3	Fe4	Fe5	Total energy (in E_h)
S4-LS	+7	18	4.2	4.2	4.2	1.1	1.1	−10754.839 78
S4-HS	+7	26	4.2	4.2	4.2	4.2	4.2	−10754.793 30

The insertion of a single water molecule into **1** with **S_4** state was computationally simulated. Computational exploration of reaction pathways for water attack revealed that H_2O breaks into **S_4** towards the triangle Fe cores (Fe1-Fe2-Fe3) through a space opened between the two π-stacked **L** units, which were found to be weakly bound and easily dissociated (Fig. 31). The geometries along the reaction coordinate of the water attack reaction were obtained by the potential energy surface (PES) scan calculations using the TPSSh-D functional. Let the progress of the reaction be parameterized by a single reaction coordinate μ, ranging from 0 [reactant (**R**)] to 1 [product (**P**)]. The structures of **S_4** + H_2O of **R** and **P** as well as transition state (**TS**) for the S4-LS and S4-HS electronic states are shown in Figure. 31. The relative energies were plotted as a function of the reaction coordinate (Fig. 32). The activation energies (ΔE(**R** → **TS**)) and reaction

energies (ΔE(**R** → **P**)) are shown in Table 9 The functional-dependence of these energies was examined using the BP86 functional [62-63] and nonlocal (NL) van der Waals corrections [64] (`NL` option in ORCA 3.0.0) in addition to the earlier-mentioned functionals.

In our theoretical model, the coordination of water to the Fe2 (or Fe3) site in the reaction **S4** + H_2O → **A** (Fig. 20) occurs with activation energy of 15-17 and 11-14 kcal/mol for S4-LS and S4-HS, respectively. This aquation leads to the saturation of the coordination of Fe2 or Fe3.

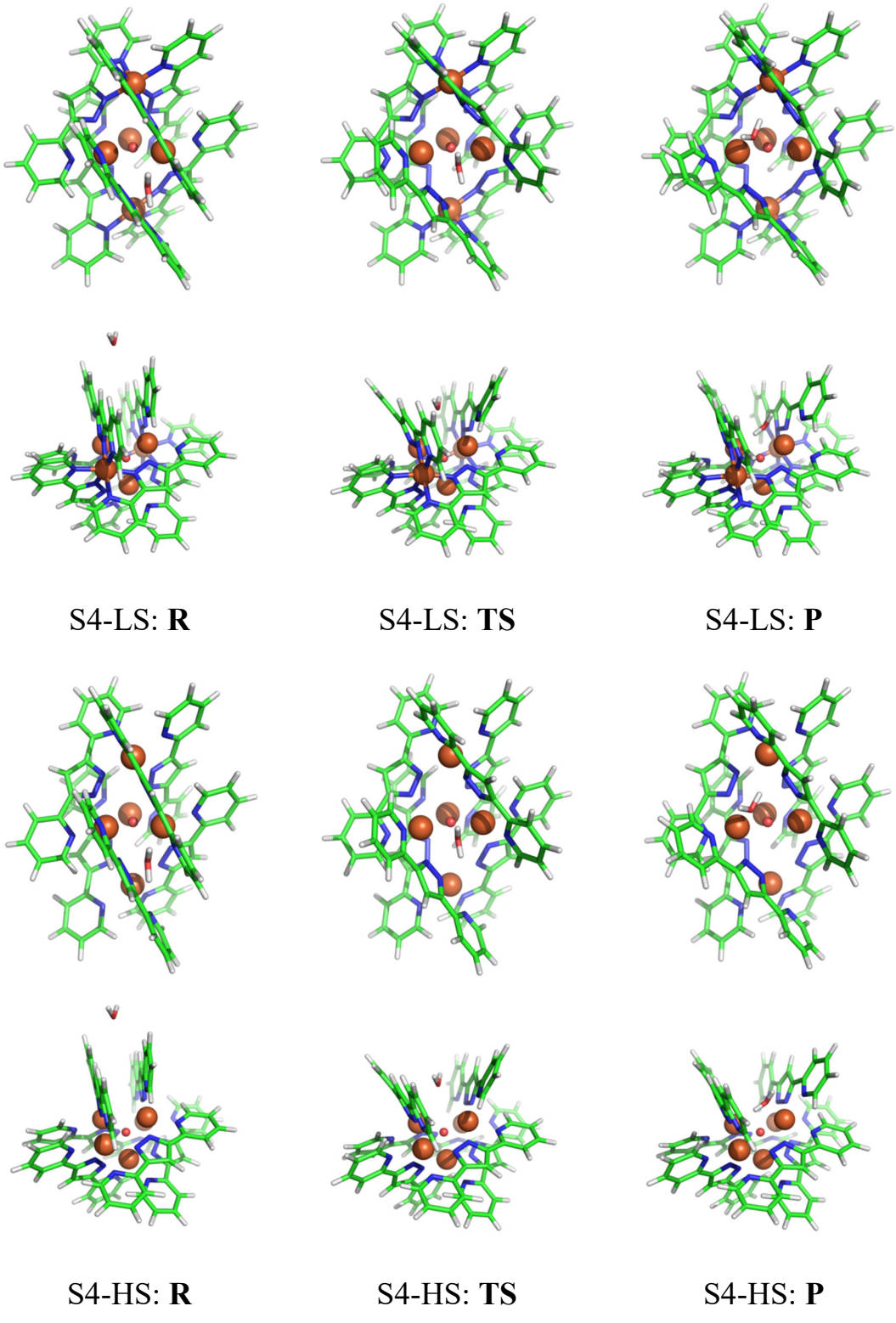

Figure 31. Structures obtained from potential energy scan calculations for water attack reaction (**S**$_4$ + H_2O → **A** in catalytic cycle of Fig. 20): Side and top views of the reactant (**R**), transition state (**TS**), and product (**P**) structures determined at the TPSSh-D level of theory for the S4-LS and S4-HS states of **S**$_4$.

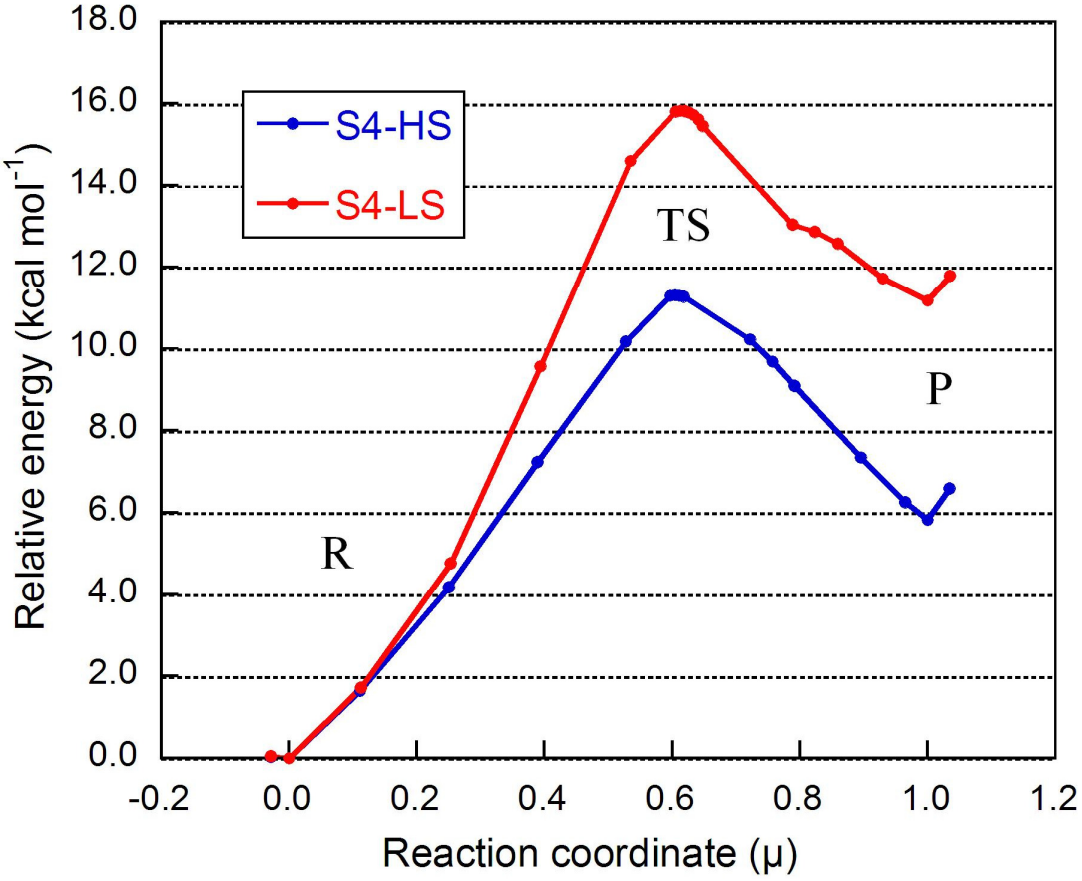

Figure 32. Relative energies of **S4** + H_2O along the reaction coordinate of water attack (μ(**R**) = 0.0 and μ(**P**) = 1.0) for the low-spin (S4-LS) and high spin (S4-HS) electronic states of **S4**. The total energies were calculated using the TPSSh-D functional. The plotted energies were given relative to the energy of **R**.

Table 9. Activation barriers (ΔE(**R** → **TS**)) and reaction energies (ΔE(**R** → **P**)) of water attack reaction (**S4** + H_2O) obtained by DFT calculations with various functionals (in kcal mol^{-1}). The both low-spin (S4-LS) and high spin (S4-HS) states were considered for the electronic state of **S4**.

		Activation barrier ΔE(**R** → **TS**)	Reaction energy ΔE(**R** → **P**)
S4-LS	TPSSh-D	16.1	11.3
	B3LYP-D [a)]	16.7	12.3
	BP86-D [a)]	17.0	13.1
	TPSSh-NL [a)]	14.9	10.0
	B3LYP-NL [a)]	15.6	11.4
S4-HS	TPSSh-D	11.8	6.0
	B3LYP-D [b)]	13.7	7.9
	BP86-D [b)]	11.9	6.7
	TPSSh-NL [b)]	10.5	4.8
	B3LYP-NL [b)]	12.9	7.4

a) On S4-LS/TPSSh-D geometries.

b) On S4-HS/TPSSh-D geometries.

(ii) Examination of Potential Energy Profile of Oxo-coupling Reaction (B → C)

Coordination of another water molecule leads to the formation of two adjacent [Fe^{III}-(OH_2)] moieties bridged by O1. They undergo sequential or simultaneous deprotonation, resulting in the adjacent Fe-oxo units. We computationally investigated the electronic-level mechanism of the direct oxo-coupling reaction that leads to the O-O bond formation (**B** → **C**). Spin polarized (or broken symmetry) DFT calculations were performed on the Fe_3(Fe-O)$_2$ intermediate to account for antiferromagnetic order arising from the two localised spin sites at the Fe2-O and Fe3-O units. The PES scan calculations were carried out using TPSSh-D and B3LYP-D functionals to identify the reaction pathway of the oxo coupling. In the PES scan calculations, the O-O bond distance was used as the scanning variable, which was set to constant values, allowing the other geometric parameters to be relaxed. The total charge was set to +3; the charge of Fe_5 complex and a single oxo ligand was assumed to be +7 (**S**$_4$ state) and −2, respectively. The DFT functionals were numerically evaluated using increased integration grids (`Grid4` option in ORCA).

Figure 33 shows the structures obtained by geometry optimisations for **B** and **C** intermediates, which correspond to the reactant (**R**) and product (**P**) states of oxo-coupling reaction, respectively. The length of the O-O bond was estimated at the B3LYP level of theory to be 2.696 and 1.395 Å for **R** and **P**, respectively. The electron occupancies and oxidation states of the Fe ions for **R** and **P** are sketched in Figure 34. The oxidation states of Fe ions were derived from unrestricted natural orbitals (UNOs) and associated electron occupancies, which were obtained by diagonalising the spin-summed density matrix as eigenfunctions and eigenvalues. The electronic configurations shown in Figure 34 are energetically the most stable in the sense that they yield the lowest total energy as a variational solution of the Kohn-Sham equation in DFT.

The mixed-valence $Fe^{II}_2Fe^{III}(Fe^{IV}{=}O)_2$ and $Fe^{II}_2Fe^{III}(Fe^{III}$-O-O-$Fe^{III})$ intermediates are formed for **R** and **P**, respectively. The DFT calculations predicted that (i) the **R** structure having Fe^{II} for Fe4 and Fe5 is more stable than that having Fe^{III} instead, and (ii) **R** with Fe^{IV}=O (oxo) for Fe2 and Fe3 units is lower in energy than that with Fe^{III}-O$^{\cdot}$ (oxyl). This highlights that the varying oxidation nature of Fe ions offers an intriguing intra-molecular redox behavior of the Fe_5 complex. The marked feature is that, to afford **R** (or **B**) via deprotonation of the two [Fe^{III}-(OH_2)] units, Fe4 and Fe5 serve as oxidants that withdraw two electrons from these units to produce the [Fe^{IV}=O] units, and then are reduced to Fe^{II}. This indicates that **1** is capable of promoting this oxidation reaction by itself without external interaction.

Table 10 shows Mulliken spin densities of Fe1—Fe5 and O1—O3 for **R**, **TS**, and **P**, and Figure 35 shows the spin density distributions of **R** and **P**. The Mulliken spin density built-up at the oxo ligand for **R** is estimated to be approximately 0.9. This can be understood by the fact that the singly-occupied *3d* orbitals of Fe is hybridised to a certain extent with the doubly-occupied *2p* orbital of the oxo ligand, and thus [Fe^{IV}=O] shares some characters with [Fe^{III}-O· (oxyl)]. Two local spin sites at the Fe-oxo units are antiferromagnetically coupled. The cofacial oxo groups proceeds to the O-O bond formation. This process was monitored by theoretical means, showing that radicals of the oxo moieties are antiferromagnetically coupled to form the σ O-O bonding (peroxo bridge), and the associated spin density on the oxo ligands diminishes for **P**. The O-O bonding reaction proceeds smoothly without spin-rearrangement and with the activation barrier less than 10 kcal mol^{-1} (Table11 and Fig. 36).

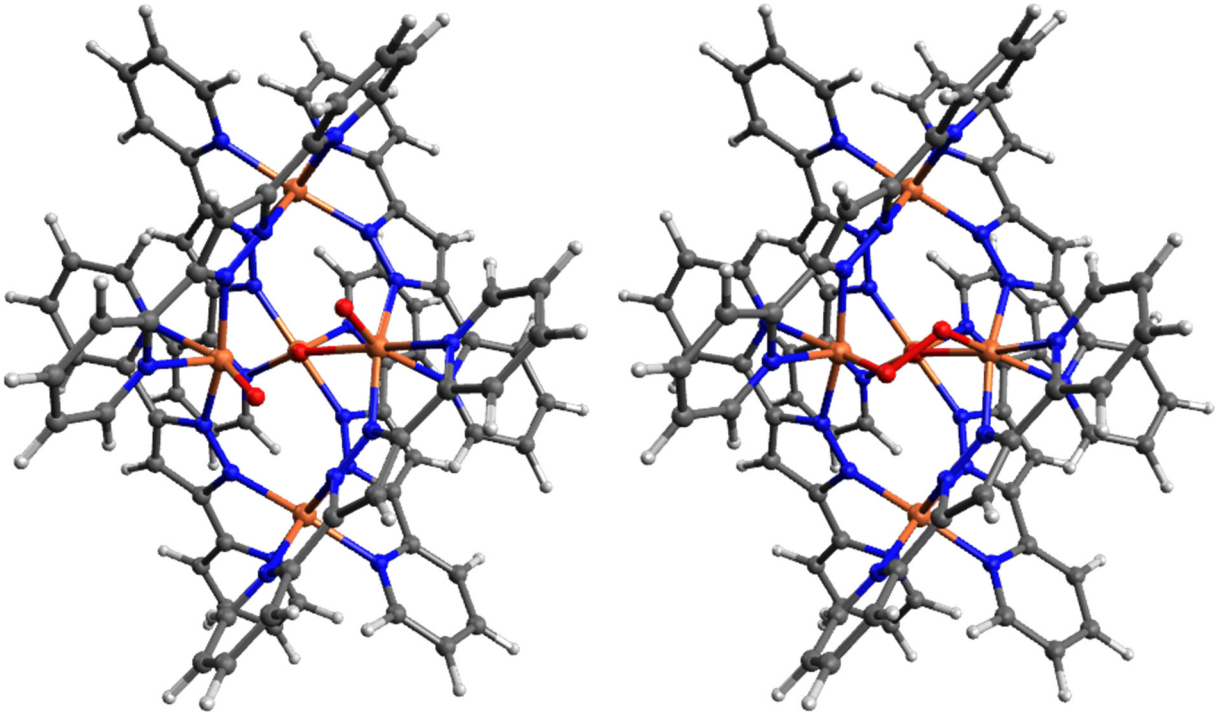

Reactant (**R**) / **B** Product (**P**) / **C**

Figure 33. Molecular structures optimised by DFT calculations using the B3LYP functional for the reactant (**R**) and product (**P**) states of oxo-coupling reaction (**B** → **C** reaction in catalytic cycle of Fig. 20). The estimated length of the O-O bond was 2.696 and 1.395 Å for **R** and **P**, respectively.

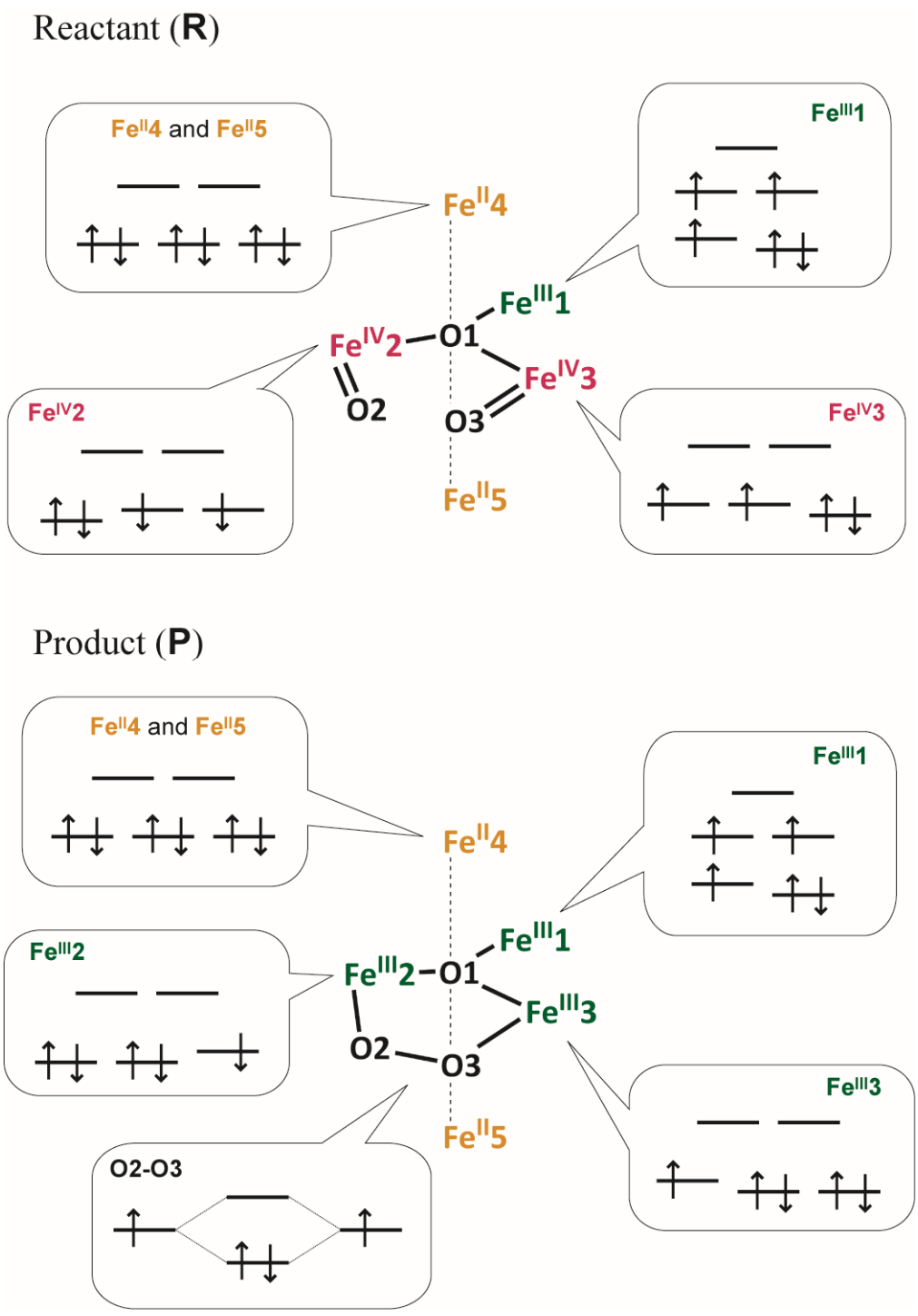

Figure 34. Electron configurations and oxidation states of Fe sites of the Fe_5 complex for the reactant (**R**) and product (**P**) of oxo-coupling reaction, and orbital interaction diagram for O2-O3 bonding in **P**.

Table 10. Mulliken spin densities for **R**, **TS**, and **P** of oxo-coupling reaction obtained at the B3LYP level of theory.

	Fe1	O1	Fe2	O2	Fe3	O3	Fe4	Fe5
R	2.68	0.26	−1.12	−0.89	1.13	0.89	0.00	0.00
TS	2.67	0.26	−0.93	−0.73	0.96	0.72	0.00	0.00
P	2.67	0.27	−0.89	−0.10	0.88	0.13	0.00	0.00

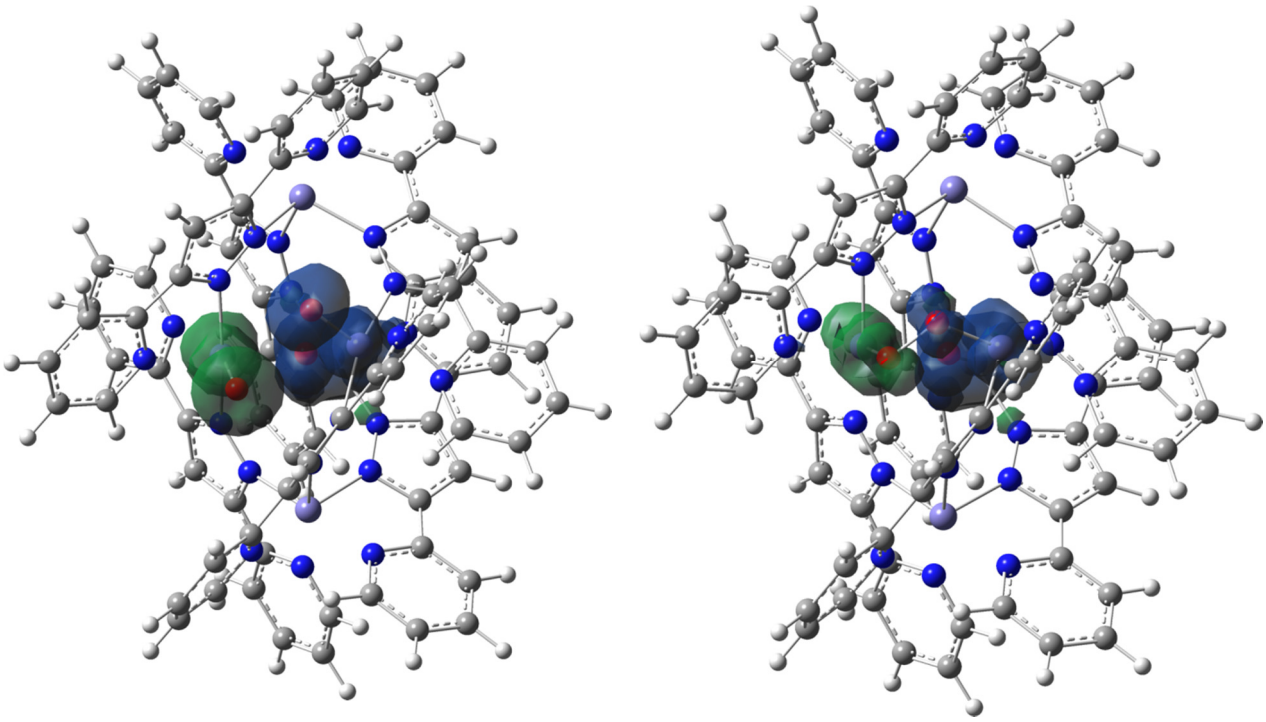

Reactant (**R**) Product (**P**)

Figure 35. Spin density distributions of **R** and **P** of oxo-coupling reaction calculated with the B3LYP functional.

Table 11. Activation barriers (ΔE(**R** → **TS**)) and reaction energies (ΔE(**R** → **P**)) of oxo-coupling reaction obtained by DFT calculations (in kcal mol^{-1}).

	Activation barrier ΔE(**R** → **TS**)	Reaction energy ΔE(**R** → **P**)
TPSSh-D	6.4	−8.9
B3LYP-D	9.0	−8.4

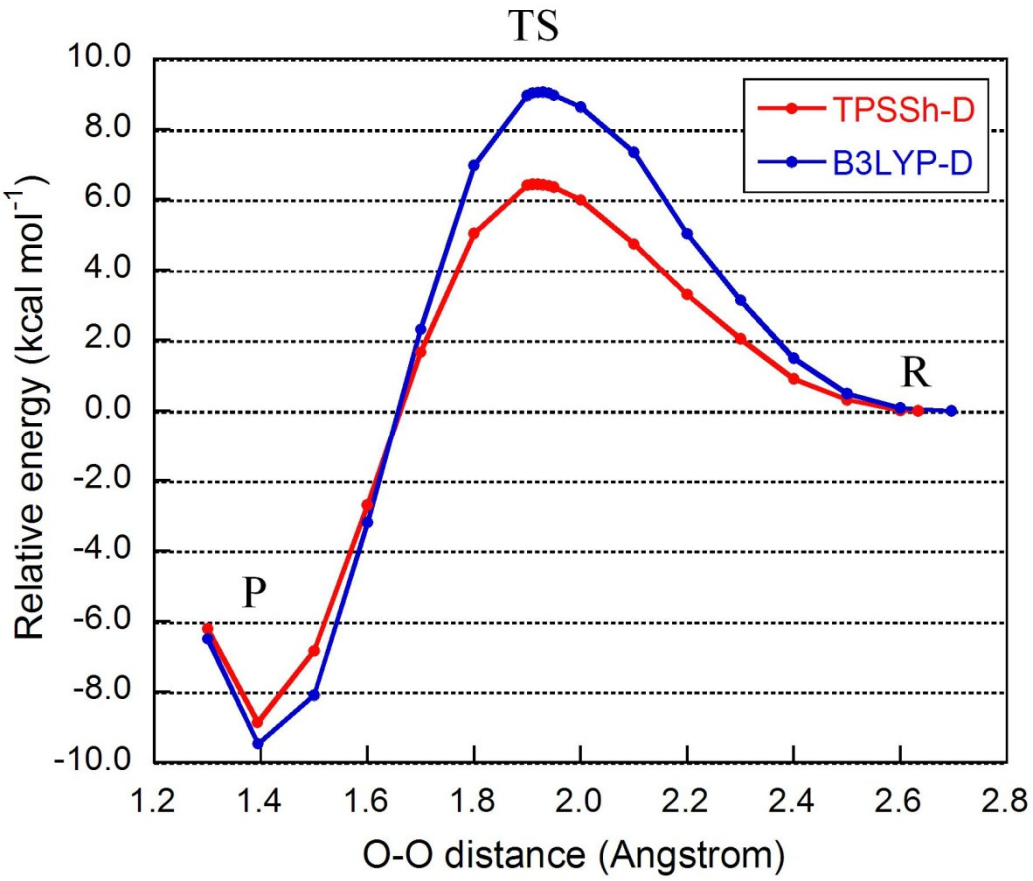

Figure 36. Relative energies along the oxo-coupling reaction pathway determined by B3LYP-D and TPSSh-D functionals. The energies were measured relative to that of **R**.

Relative stability of various electronic states for R intermediate

In addition, a detailed analysis was performed on the relative stability of the mixed-valence **R** intermediate, in which coexistence of Fe(IV) and Fe(II) ions is allowed as the most stable species. We examined various electronic states derived from all possible combinations of the following local electronic (spin and oxidation) configurations:

Chart 1.

- Fe1

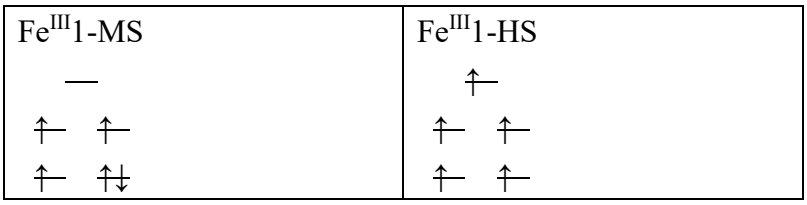

- Fe2, Fe3

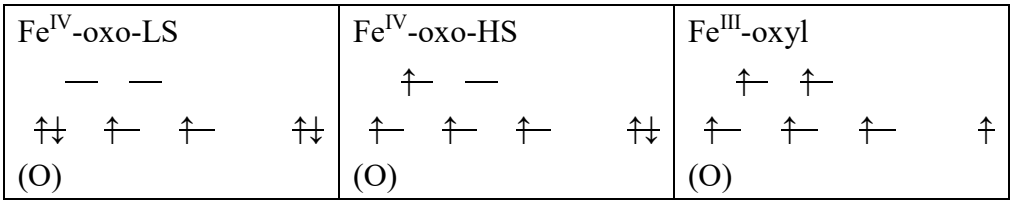

- Fe4, Fe5

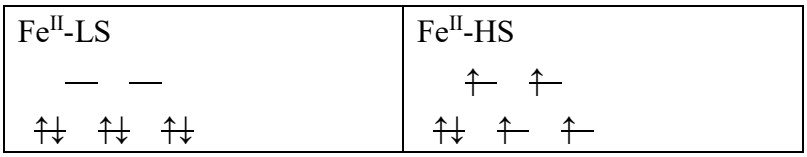

The combinations thus lead to twelve (=2×3×2) electronic states, accounting for two types of oxidation states corresponding to $(Fe^{II})_2(Fe^{III})_3$ and $(Fe^{II})_2(Fe^{III})(Fe^{IV})_2$. DFT/TPSSh calculations were carried out to evaluate the energetics of these states. Table 12 shows relative energies of the twelve electronic states, offering the following observations:

(i) The $(Fe^{II})_2(Fe^{III})(Fe^{IV})_2$ state composed of Fe^{III}1-MS (middle spin) for Fe1, Fe^{IV}-oxo-LS for Fe2 and Fe3, and Fe^{II}-LS state Fe4 and Fe5 is the most stable.

(ii) The $(Fe^{II})_2(Fe^{III})_3$ states are higher-lying by more than 43 kcal mol^{-1} relative to the most stable $(Fe^{II})_2(Fe^{III})(Fe^{IV})_2$ state.

Table 12. Relative energies (in kcal mol^{-1}) of various electronic states for **R** intermediate, which are derived from all possible combinations of local configuration sets: two local electronic configurations (Fe^{III}1-MS and Fe^{III}1-HS) for Fe1, three (Fe^{IV}-oxo-LS, Fe^{IV}-oxo-HS, and Fe^{III}-oxyl) for Fe2 and Fe3, and two (Fe^{II}-LS and Fe^{II}-HS) for Fe4 and Fe5. Energies as a function of local configuration states are given relative to the $(Fe^{II})_2(Fe^{III})(Fe^{IV})_2$ state composed of Fe^{III}1-MS (middle spin) for Fe1, Fe^{IV}-oxo-LS for Fe2 and Fe3, and Fe^{II}-LS state Fe4 and Fe5.

Fe1	Fe2, Fe3	Fe4, Fe5	
		Fe^{II}-LS	Fe^{II}-HS
Fe^{III}1-MS	Fe^{IV}-oxo-LS	0.0	7.8
	Fe^{IV}-oxo-HS	11.1	19.4
	Fe^{III}-oxyl	43.8	51.5
Fe^{III}1-HS	Fe^{IV}-oxo-LS	24.0	32.0
	Fe^{IV}-oxo-HS	37.1	47.4
	Fe^{III}-oxyl	73.8	79.9

(iii) Atomic charge and spin population analysis of S_0−S_4 states

The electron density maps resulting from the DFT calculations were analysed for the **S_0**−**S_4** states. In the DFT calculation of the **S_n** state (a net charge of n + 3), the M_S parameter was set to n + 14; i.e., M_S = 14 (**S_0**), 15 (**S_1**), 16 (**S_2**), 17 (**S_3**), and 18 (**S_4**). The molecular geometries were optimised for each **S_n** state using the TPSSh-D and B3LYP-D functionals respectively with exception that the geometry optimisation for **S_2** was performed using the BP86-D functional in order to circumvent the convergence issue.

The atomic charges and spin populations of Fe ions for each **S_n** state were calculated from Mulliken population formula. Using them as a measure of the gross electron occupancy, the oxidation state (or valence) and spin configuration of each Fe site were assigned (Table 13). Note that Mulliken population scheme underestimates the number of electrons residing in the Fe ions where the occupied orbitals associated with Fe electrons are delocalised over ligand atoms (electron delocalisation). For comparison, Table 13 includes the results of ^{57}Fe Mössbauer measurement for **S_0**−**S_2** states (P. 52 and P. 85-88).

The most important observation is that the electronic configurations determined by the DFT calculations accord with the assignments by ^{57}Fe Mössbauer spectroscopy for **S_0**−**S_2** states (see also Fig. 29). Note that, as usually done in the standard DFT procedure, we specified the total number of electrons in the entire system *a priori* as input (with net charge and M_S), but the local electron occupancies of the Fe centers were given without any manual specification as a result of the solution of DFT equation. These results strongly indicate that the electronic states of our iron catalyst can be characterized by the DFT calculations with adequate accuracy.

Table 13. Mulliken atomic charges and spin populations of Fe ions determined at TPSSh-D and B3LYP-D levels of theory for the pentanuclear iron complex (**1**) with the **S_0-S_4** states.

(a) **S_0** state (a net charge of +3 with M_S = 14)

	Atomic charge	Spin population	Oxidation state	Unpaired electrons
TPSSh-D				
Fe1	1.08	3.89	2.33	+4.33
Fe2	1.09	3.99	2.33	+4.33
Fe3	1.05	3.96	2.33	+4.33
Fe4	0.41	0.04	II	+0
Fe5	0.42	0.04	II	+0
B3LYP-D				
Fe1	0.92	3.77	II	+4
Fe2	1.14	4.13	III	+5
Fe3	0.97	3.85	II	+4
Fe4	0.38	0.02	II	+0
Fe5	0.38	0.01	II	+0

	Local electronic configuration		
	TPSSh-D	B3LYP-D	Exptl.[a)]
Fe1	Fe(II) HS × 2 Fe(III) HS × 1	Fe(II) HS Fe(III) HS Fe(II) HS	Fe(II) HS × 2 Fe(III) HS × 1
Fe2			
Fe3			
Fe4	Fe(II) LS	Fe(II) LS	Fe(II) LS
Fe5	Fe(II) LS	Fe(II) LS	Fe(II) LS

a) Assignment from ^{57}Fe Mössbauer spectroscopy (P. 52).

Table 13. (Continued)

(b) $\mathbf{S_1}$ state (a net charge of +4 with $M_S = 15$)

	Atomic charge	Spin population	Oxidation state	Unpaired electrons
TPSSh-D				
Fe1	1.20	4.18	2.66	+4.66
Fe2	1.08	4.02	2.66	+4.66
Fe3	1.08	4.02	2.66	+4.66
Fe4	0.43	0.15	II	+0
Fe5	0.43	0.15	II	+0
B3LYP-D				
Fe1	1.14	4.22	III	+5
Fe2	1.00	3.93	II	+4
Fe3	1.10	4.13	III	+5
Fe4	0.37	0.03	II	+0
Fe5	0.38	0.04	II	+0

	Local electronic configuration		
	TPSSh-D	B3LYP-D	Exptl.[a)]
Fe1	Fe(II) HS × 1 Fe(III) HS × 2	Fe(III) HS	Fe(II) HS × 1 Fe(III) HS × 2
Fe2		Fe(II) HS	
Fe3		Fe(III) HS	
Fe4	Fe(II) LS	Fe(II) LS	Fe(II) LS
Fe5	Fe(II) LS	Fe(II) LS	Fe(II) LS

a) Assignment from ^{57}Fe Mössbauer spectroscopy (P. 86).

Table 13. (Continued)

(c) **S_2** state (a net charge of +5 with M_S = 16)

	Atomic charge	Spin population	Oxidation state	Unpaired electrons
TPSSh-D				
Fe1	0.99	3.94	2.33	+4.33
Fe2	0.99	3.92	2.33	+4.33
Fe3	0.98	3.92	2.33	+4.33
Fe4	0.44	1.06	III	+1
Fe5	0.46	1.06	III	+1
B3LYP-D				
Fe1	0.93	3.90	2.33	+4.33
Fe2	0.94	3.90	2.33	+4.33
Fe3	0.94	3.90	2.33	+4.33
Fe4	0.37	1.07	III	+1
Fe5	0.38	1.07	III	+1

	Local electronic configuration		
	TPSSh-D	B3LYP-D	Exptl.[a)]
Fe1	Fe(II) HS × 2	Fe(II) HS × 2	Fe(II) HS × 2
Fe2	Fe(III) HS × 1	Fe(III) HS × 1	Fe(III) HS × 1
Fe3			
Fe4	Fe(III) LS	Fe(III) LS	Fe(III) LS
Fe5	Fe(III) LS	Fe(III) LS	Fe(III) LS

a) Assignment from ^{57}Fe Mössbauer spectroscopy (P. 87).

Table 13. (Continued)

(d) **S_3** state (a net charge of +6 with M_S = 17)

	Atomic charge	Spin population	Oxidation state	Unpaired electrons
TPSSh-D				
Fe1	1.14	4.10	2.66	+4.66
Fe2	1.13	4.11	2.66	+4.66
Fe3	1.13	4.11	2.66	+4.66
Fe4	0.54	1.07	III	+1
Fe5	0.54	1.07	III	+1
B3LYP-D				
Fe1	0.93	3.78	II	+4
Fe2	1.14	4.22	III	+5
Fe3	1.14	4.22	III	+5
Fe4	0.50	1.07	III	+1
Fe5	0.50	1.07	III	+1

	Local electronic configuration	
	TPSSh-D	B3LYP-D
Fe1	Fe(II) HS × 1 Fe(III) HS × 2	Fe(II) HS
Fe2		Fe(III) HS
Fe3		Fe(III) HS
Fe4	Fe(III) LS	Fe(III) LS
Fe5	Fe(III) LS	Fe(III) LS

Table 13. (Continued)

(e) **S$_4$** state (a net charge of +7 with M_S = 18)

	Atomic charge	Spin population	Oxidation state	Unpaired electrons
TPSSh-D				
Fe1	1.17	4.21	III	+5
Fe2	1.17	4.21	III	+5
Fe3	1.17	4.21	III	+5
Fe4	0.55	1.08	III	+1
Fe5	0.55	1.08	III	+1
B3LYP-D				
Fe1	1.13	4.22	III	+5
Fe2	1.13	4.22	III	+5
Fe3	1.13	4.22	III	+5
Fe4	0.51	1.08	III	+1
Fe5	0.51	1.08	III	+1

	Local electronic configuration	
	TPSSh-D	B3LYP-D
Fe1	Fe(III) HS	Fe(III) HS
Fe2	Fe(III) HS	Fe(III) HS
Fe3	Fe(III) HS	Fe(III) HS
Fe4	Fe(III) LS	Fe(III) LS
Fe5	Fe(III) LS	Fe(III) LS

In conclusion, water oxidation by a pentanuclear iron complex was demonstrated with redox flexibility and adjacent water-activation sites. Plausible reaction mechanism derived from experimental and calculation results suggest the roles of these key factors as follows. The redox flexibility enables the accumulation of positive charges (**S_0→S_4** in Fig. 20, P. 78) and intramolecular electron rearrangement (**A→B**) to form the reactive, high-valent oxo species. The adjacent active sites afford cofacial oxo units, which can be converted to peroxo species *via* intramolecular O-O bond formation with a low activation barrier and without spin-rearrangement (**B→C**). These two structural characteristics facilitating charge accumulation and O-O bond formation enabled the high catalytic activity and durability of **1** for water oxidation. Hence, the TOF value for **1** was found to be 1,900 s^{-1}, which is more than 1,000 times greater than those of other reported iron-based catalysts (~1.3 s^{-1}, ref 7). Our results reported here offer a new strategy for creating abundant metal-based molecular catalysts for water oxidation with substantial efficiency and robustness. Because the high activity of our pentairon catalyst was achieved in acetonitrile/water mixture with large overpotential (0.52 V at pH=2), one of the next targets in this project is to provide a design of catalyst that operates water oxidation in water with low overpotential like OEC in PSII, in which the water oxidation proceeds in water with a very small overpotential (less than 0.3 V, based on the estimated potential of the tyrosine residue (Y_z) of 1.0-1.2 V).

Materials and Methods

Materials.

$NaBF_4$ and NaOH were purchased from Wako Pure Chemical Industries, Ltd. $FeSO_4 \cdot 7H_2O$ was purchased from Kanto Chemical Co., Inc. 3,5-Bis(2-pyridyl)pyrazole and tetraethylammonium perchlorate were purchased from Tokyo Chemical Industry Co., Ltd. Tris(4-bromophenyl)ammoniumyl hexachloroantimonate (from Aldrich) was used as received. Tris(2,4-dibromophenyl)ammoniumyl hexachloroantimonate was synthesized using the reported procedure [65]. Dry acetonitrile (CH_3CN) was degassed and purified under N_2 atmosphere using a GlassContour solvent system (Nikko Hansen Co., Ltd.). All solvents and reagents are of the highest quality available and used as received except for tetraethylammonium perchlorate. Tetraethylammonium perchlorate was recrystallised from absolute ethanol. H_2O was purified using a Millipore MilliQ purifier, and was sparged with argon before use.

Synthesis of [{Fe^{II}(μ-L)$_3$}$_2$ $Fe^{II}_2Fe^{III}$ (μ-O)](BF$_4$)$_3$·7H$_2$O (1(BF$_4$)$_3$·7H$_2$O).

Aqueous solution (2.88 mL) of NaOH (0.72 mmol, 28.8 mg) was added to the methanolic solution (6 mL) of 3,5-bis(2-pyridyl)pyrazole (**L**H; 0.72 mmol, 160 mg). $FeSO_4 \cdot 7H_2O$ (0.60 mmol, 168 mg) was then added to the reaction mixture and stirred at room temperature for a few minutes. The reaction mixture was filtered to remove undissolved residues and a few drops of saturated aqueous $NaBF_4$ solution was added to the filtrate. The obtained suspension was kept in a refrigerator for 30 min and the precipitate was collected by filtration. The obtained precipitate was dissolved in 1:1 mixture of acetonitrile and water (40 mL) and a slow evaporation of acetonitrile at ambient temperature gave dark orange crystals after a few days. The crystals were collected by filtration and dried under vacuum. Yield 137 mg (72%). Elemental analysis Calcd. for **1**$(BF_4)_3 \cdot 7H_2O$: $C_{78}H_{68}F_{12}Fe_5N_{24}O_8B_3$: C, 46.63; H, 3.41; N, 16.73%. Found: C, 46.46; H 3.59; N 16.83%. ESI-TOF MS (positive ion, acetonitrile): m/z: 540.7 $[\{Fe^{II}(\mu\text{-}\mathbf{L})_3\}_2Fe^{II}_2Fe^{III}(\mu\text{-O})]^{3+}$.

Measurement Apparatus.

Elemental analyses were carried out on a J-SCIENCE LAB MICRO CORDER JM10 elemental analyser. ESI-TOF mass spectra were recorded on a JEOL JMS-T100LP mass spectrometer. Gas analysis for O_2 was performed using a Shimadzu GC-8A gas chromatograph equipped with a thermal conductivity detector and fitted with a molecular sieve 5A column, calibrated with air. X-ray photoelectron spectroscopy (XPS, Omicron

EA125 analyzer) measurements were carried out using a monochromatic Al Kα excitation source (1486.6 eV) to examine the atomic composition of the ITO surface.

X-ray Crystallography.

A crystal of **1**$(BF_4)_3$ were mounted in a loop. Diffraction data at 123 K were measured on a RAXIS-RAPID Imaging Plate diffractometer equipped with confocal monochromated Mo-Kα radiation and data was processed using RAPID-AUTO (Rigaku). The structure was solved by direct method using *SIR-92* [66] and refined by the full-matrix least squares techniques on F^2 (*SHELXL-97* [67]). All non-hydrogen atoms were refined anisotropically and refined with a riding model with U_{iso} constrained to be 1.2 times U_{eq} of the carrier atom. The diffused electron densities resulting from residual solvent molecules were removed from the data set using the SQUEEZE routine of PLATON [68] and refined further using the data generated.

^{57}Fe Mössbauer Spectroscopy.

The Mössbauer spectra (isomer shift *vs.* metallic iron at room temperature) were measured with a Wissel MVT-1000 Mössbauer spectrometer with a ^{57}Co/Rh source in the transmission mode. All isomer shifts are given relative to α-Fe at room temperature. Measurements at low temperature were performed with a closed-cycle helium refrigerator cryostat (Iwatani Co., Ltd.).

Electrochemical and UV-Vis Spectral Measurements.

All experimental procedures were conducted at ambient temperature, 20 ºC, under argon. A standard three-electrode configuration was employed in conjunction with a CH Instruments potentiostat interfaced to a computer with CH Instruments 650 DKMP software. In all cases, a platinum auxiliary electrode and Ag/Ag^+ reference electrode were used. Cyclic voltammetry was performed using a GC disk working electrode (diameter 3 mm, from BAS Inc.). The working electrode was treated between scans by means of polishing with 0.05 μm alumina paste (from BAS Inc.) and washing with purified H_2O. Ferrocene was used as an internal standard, and all potentials reported within this work are referenced to the ferrocenium/ferrocene couple at 0 V. Controlled potential electrolysis was performed in a custom-designed gas-tight cell using an ITO-coated glass electrode (0.7 mm thick, 10 Ω/sq from Furuuchi Chemical Co. Ltd.). The ITO electrode was washed by ultrasonication in a methanolic solution of 0.5 M K_2CO_3 for 30 min and then rinsed with acetonitrile and purified water prior to use. UV-vis spectral measurements were recorded using SHIMADZU UV-2550 UV-VIS spectrophotometer

with a conventional quartz cuvette (path length, l = 1 cm). Spectroelectrolysis was performed using a BAS Inc. spectroelectrochemical quartz cell (l = 1 mm) containing a Pt gauze (working electrode), Pt wire (auxillary electrode) and Ag/Ag^+ (reference electrode) in conjunction with the CH Instruments potentiostat.

Controlled Potential Electrolysis

Controlled potential electrolysis was carried out in a two compartment cell separated by an anion-exchange membrane (Fig. 6). The working electrode was a 1.0 cm × 3.5 cm piece of ITO-coated glass cut. Typically, 1.0 cm × 2.0 cm was immersed in the solution. 6.5 mL of the electrolyte solution (0.1 M Et_4NClO_4 in acetonitrile/water (10 : 1) mixed solvent) degassed with vacuum/Ar cycles was electrolysed for 30 min at 1.42 V (*vs.* Fc/Fc^+) with stirring. **1**$(BF_4)_3 \cdot 7H_2O$ (1.3 μmol) was added to the electrolyte solution and degassed again. The catalyst solution was electrolysed for 120 min at the same potential as the blank solution. After the electrolysis, the oxygen evolved in the headspace of the reaction cell was quantified by a gas chromatography. Subsequently, the oxygen dissolved in the reaction mixture was also quantified. 2.0 mL of the reaction mixture was transferred to a glass vessel filled with Ar and was kept at room temperature for 20 min until the system reached to the equilibrium. The oxygen released from the solution was quantified by gas chromatography.

References

1. S. W. Gersten, G. J. Samuels and T. J. Meyer, *J. Am. Chem. Soc.* **1982**, *104*, 4029.
2. T. Wada, K. Tsuge and K. Tanaka, *Angew. Chem. Int. Ed.* **2000**, *39*, 1479.
3. R. Zong and R. P. Thummel, *J. Am. Chem. Soc.* **2005**, *127*, 12802.
4. J. J. Concepcion, J. W. Jurss, J. L. Templeton and T. J. Meyer, *J. Am. Chem. Soc.* **2008**, *130*, 16462.
5. W. C. Ellis, N. D. McDaniel, S. Bernhard and T. J. Collins, *J. Am. Chem. Soc.* **2010**, *132*, 10990.
6. Q. Yin, J. M. Tan, C. Besson, Y. V. Geletii, D. G. Musaev, A. E. Kuznetsov, Z. Luo, K. I. Hardcastle and C. L. Hill, *Science* **2010**, *328*, 342.
7. M. Yoshida, S. Masaoka, J. Abe and K. Sakai, *Chem. Asian J.* **2010**, *5*, 2369.
8. J. L. Fillol, Z. Codolà, I. Garcia-Bosch, L. Gómez, J. JoséPla and M. Costas, *Nature Chem.* **2011**, *3*, 807.
9. L. Duan, F Bozoglian, S. Mandal, B. Stewart, T. Privalov, A. Llobet and L. Sun *Nature Chem*. **2012**, *4*, 418.
10. S. M. Barnett, K. I. Goldberg and J. M. Mayer, *Nature Chem.* **2012**, *4*, 498.
11. L. Vigara, M. Z. Ertem, N. Planas, F. Bozoglian, N. Leidel, H. Dau, M. Haumann, L. Gagliardi, C. J. Cramer and A. Llobet, *Chem. Sci.* **2012**, *3*, 2576.
12. D. Hong, S. Mandal, Y. Yamada, Y.-M. Lee, W. Nam, A. Llobet and S. Fukuzumi, *Inorg. Chem.* **2013**, *52*, 9522.
13. D. Wang and J. T. Groves, *Proc. Natl Acad. Sci. USA* **2013**, *110*, 15579.
14. M. K. Coggins, M.-T. Zhang, A. K. Vannucci, C. J. Dares and T. J. Meyer, *J. Am. Chem. Soc.* **2014**, *136*, 5531.
15. R. Matheu, M. Z. Ertem, J. Benet-Buchholz, E. Coronado, V. S. Batista, X. Sala and A. Llobet, *J. Am. Chem. Soc.* **2015**, *137*, 10786.
16. M. W. Kanan and D. G. Nocera, *Science* **2008**, *321*, 1072.
17. R. K. Hocking, R. Brimblecombe, L.-Y. Chang, A. Singh, M. H. Cheah, C. Glover, W. H. Casey and L. Spiccia, *Nature Chem.* **2011**, *3*, 461.
18. Y. Umena, K. Kawakami, J.-R. Shen and N. Kamiya, *Nature* **2011**, *473*, 55.
19. B. Meunier, S. P. de Visser and S. Shaik, *Chem. Rev.* **2004**, *104*, 3947.
20. C. E. Tinberg and S. J. Lippard, *Acc. Chem. Res.* **2011**, *44*, 280.
21. M. Costas, K. Chen and L. Jr. Que, *Coord. Chem. Rev.* **2000**, *200-202*, 517.
22. G. C. Dismukes, R. Brimblecombe, G. A. N. Felton, R. S. Pryadun, J. E. Sheats, L. Spiccia and G. F. Swiegers, *Acc. Chem. Res.* **2009**, *42*, 1935.
23. O. Einsle, F. A. Tezcan, S. L. A. Andrade, B. Schmid, M. Yoshida, J. B. Howard, D. C. Rees, *Science* **2002**, *297*, 1696.

24. M. Kodera, Y. Kawahara, Y. Hitomi, T. Nomura, T. Ogura and Y. Kobayashi, *J. Am. Chem. Soc.* **2012**, *134*, 13236.
25. S. Kundu, E. Matito, S. Walleck, F. F. Pfaff, F. Heims, B. Rábay, J. M. Luis, A. Company, B. Braun, T. Glaser and K. Ray, *Chem. Eur. J.* **2012**, *18*, 2787.
26. K. Yoneda, K. Adachi, K. Nishio, M. Yamasaki, A. Fuyuhiro, M. Katada, S. Kaizaki and S. Kawata, *Angew. Chem. Int. Ed.* **2006**, *45*, 5459.
27. M. L. Helm, M. P. Stewart, R. M. Bullock, M. R. DuBois and D. L. A DuBois, *Science* **2011**, *333*, 863.
28. C. C. L. McCrory, C. Uyeda and J. C. Peters, *J. Am. Chem. Soc.* **2012**, *134*, 3164.
29. S. C. Marinescu, J. R. Winklerand and H. B. Gray, *Proc. Natl Acad. Sci. USA* **2012**, *109*, 15127.
30. C. Costentin, S. Drouet, M. Robert and J.-M. Savéant, *Science*, **2012**, *338*, 90.
31. A. Sartorel, M. Carraro, G. Scorrano, R. De Zorzi, S. Geremia, N. D. McDaniel, S. Bernhard and M. Bonchio, *J. Am. Chem. Soc.* **2008**, *130*, 5006.
32. M. Yagi, A. Syouji, S. Yamada, M. Komi, H. Yamazaki and S. Tajima, *Photochem. Photobiol. Sci.* **2009**, *8*, 139.
33. J. J. Concepcion, J. W. Jurss, P. G. Hoertz and T. J. Meyer, *Angew. Chem. Int. Edn.* **2009**, *48*, 9473.
34. L. Duan, Y. Xu, P. Zhang, M. Wang and L. Sun, *Inorg. Chem.* **2010**, *49*, 209.
35. Y. Xu, L. Duan, L. Tong, B. Åkermark and L. Sun, *Chem. Commun.* **2010**, *46*, 6506.
36. Y. Xu, A. Fischer, L. Duan, L. Tong, E. Gabrielsson, B. Åkermark and L. Sun, *Angew. Chem. Int. Ed.* **2010**, *49*, 8934.
37. Z. Chen, J. J. Concepcion, H. Luo, J. F. Hull, A. Paul and T. J. Meyer, *J. Am. Chem. Soc.* **2010**, *132*, 17670.
38. Z. Chen, J. J. Concepcion and T. J. Meyer, *Dalton Trans.* **2011**, *40*, 3789.
39. M. Natali, M. Orlandi, S. Berardi, S. Campagna, M. Bonchio, A. Sartorel and F. Scandola, *Inorg. Chem.* **2012**, *51*, 7324.
40. M. D. Kärkäs, T Åkermark, E. V. Johnston, S. R. Karim, T. M. Laine, B.-L. Lee, T. Åkermark, T. Privalov and B. Åkermark, *Angew. Chem. Int. Ed*. **2012**, *51*, 11589.
41. L. Wang, L. Duan, B. Stewart, M. Pu, J. Liu, T. Privalov and L. Sun, *J. Am. Chem. Soc.* **2012**, *134*, 18868.
42. M. D. Kärkäs, T Åkermark, H. Chen, J. Sun and B. Åkermark, *Angew. Chem. Int. Ed*. **2013**, *52*, 4189.

43. N. Song, J. J. Concepcion, R. A. Binstead, J. A. Rudd, A. K. Vannucci, C. J. Dares, M. K. Coggins and T. J. Meyer, *Proc. Natl Acad. Sci. USA* **2015**, *112*, 4935.
44. D. J. Wasylenko, C. Ganesamoorthy, J. Borau-Garcia and C. P. Berlinguette, *Chem. Commun*. **2011**, *47*, 4249.
45. D. K. Dogutan, R. Jr. McGuire, and D. G. Nocera, *J. Am. Chem. Soc.* **2011**, *133*, 9178.
46. S. Tanaka, M. Annaka and K. Sakai, *Chem. Commun.* **2012**, *48*, 1653.
47. T. Nakazono, A. R. Parent and K. Sakai, *Chem. Commun.* **2013**, *49*, 6325.
48. M.-T. Zhang, Z. Chen, P. Kang and T. J. Meyer, *J. Am. Chem. Soc*. **2013**, *135*, 2048.
49. K. S. Joya, N. K. Subbaiyan, F. D'Souza and H. J. M. de Groot, *Angew. Chem. Int. Edn. Engl.* **2012**, *51*, 9601.
50. Z. Codolà, J. M. S. Cardoso, B. Royo, M. Costas and J. L. Fillol, *Chem. Eur. J.* **2013**, *19*, 7203.
51. J. Limburg, J. S. Vrettos, H. Chen, J. C. de Paula, R. H. Crabtree and G. W. Brudvig, *J. Am. Chem. Soc.* **2001**, *123*, 423.
52. N. G. Connelly and W. E. Geiger, *Chem. Rev*. **1996**, *96*, 877.
53. F. Neese, ORCA — An Ab Initio Density Functional and Semiempirical Program Package, (v. 2.6-35), Universität Bonn, Bonn, Germany, **2007**.
54. F. Weigend and R. Ahlrichs, *Phys. Chem. Chem. Phys.* **2005**, *7*, 3297.
55. D. A. Pantazis, X. Y. Chen, C. R. Landis and F. Neese, *J. Chem. Theory Comput*. **2008**, *4*, 908.
56. A. D. Becke, *J. Chem. Phys*. **1993**, *98*, 5648.
57. J. Tao, J. P. Perdew, V. N. Staroverov and G. E. Scuseria, *Phys. Rev. Lett.* **2003**, *91*, 146401.
58. S. Grimme, J. Antony, S. Ehrlich and H. Krieg, *J. Chem. Phys.* **2010**, *132*, 154104.
59. M. Douglas and N. M. Kroll, *Ann. Phys. (N.Y.)* **1974**, *82*, 89.
60. F. Weigend, *Phys. Chem. Chem. Phys.* **2006**, *8*, 1057.
61. F. Neese, F. Wennmohs, A. Hansen and U. Becker, *Chem. Phys.* **2009**, *356*, 98.
62. A. D. Becke, *Phys. Rev. A* **1988**, *38*, 3098.
63. J. P. Perdew, *Phys. Rev. B* **1986**, *33*, 8822.
64. O. A. Vydrov and T. V. Voorhis, *J. Chem. Phys.* **2010**, *133*, 244103.
65. S. L. Matthews and D. M. Heinekey, *Inorg. Chem*. **2011**, *50*, 7925.

66. A. Altomare, G. Cascarano, C. Giacovazzo and A. Guagliardi, *J. Appl. Cryst*. **1933**, *26*, 343.
67. G. M. Sheldrick, *Program for Crystal Structure Refinement*, University of Göttingen, Germany, **1997**.
68. A. L Spek, *Acta Cryst*. **2009**, D*65*, 148.

Chapter 3

Water oxidation reaction catalyzed by a penta-nuclear iron complex bearing PCET sites

Introduction

The oxidation of water into molecular oxygen is a crucial process in many schemes of artificial photosynthesis that could solve the world's energy and environmental problems. In nature, the water oxidation is catalyzed by an oxygen evolving complex (OEC)[1] with a high reaction rate (TOF = 400 s^{-1})[2] and a small overpotential (< 0.3 V)[3]. To mimic the functional activity of the OEC, the development of molecular catalysts for water oxidation have been extensively investigated and variety of metal complexes were reported to date.[4] Especially, the efforts devoted to the catalyst based on iron which have an advantage of the low cost and the richness in the earth[5]. In Chapter 2, the author describes rationally designed a pentanuclear iron complex, $[Fe^{II}_4Fe^{III}(\mu_3\text{-}O)(\mu\text{-}\mathbf{L})_6]^{3+}$ (**1**; **L**H = 3,5-bis(2-pyridyl)pyrazole) showing a high catalytic activity toward water oxidation.[Chapter 2] Experimental and theoretical investigation revealed that the complex is oxidized to form four oxidized species that react with water to form iron(IV) oxo intermediate and the O-O bond formation occurs from the two adjacent oxo unit with a low activation barrier. Although the TOF for water oxidation catalyzed by **1** reach 1900 s^{-1} calculated by electrochemical measurements, a high overpotential (> 0.52 V) is required. This study indicates that efficient water oxidation catalysts based on iron complexes can be created by ensuring the system has redox flexibility and contains adjacent water-activation sites, but the challenge to operate the water oxidation with much a lower overpotential is still remained.

One of the primary factor of the large overpotential is considered to be the high positive charge of the Fe^{III}_5 state active for oxidizing water. During the processes of the water oxidation, the total charge of the complex is accumulated from +3 to +7, because the oxidation of the complex is not coupled with a proton transfer. Therefore, the suppression of charge increase probably lead the decrease of the overpotential. Based on such a point of view, the author employed a new pentanuclear iron complex with PCET sites, [{Fe^{II}(μ-

$H_2bip)_3\}_2Fe^{II}_2Fe^{III}(\mu_3\text{-}O)]^{3+}$ (**2**) (H_2bip = 3,5-bis(benzimidazolyl)pyrazole; Fig. 1), as a promising candidate for water oxidation catalysts with a low overpotential. The ligand bears two dissociative protons and is expected to serve as a PCET module by proton transfer from the ligand coupled with electron transfer from iron center. Indeed, our previous work demonstrates that the introduction of the imidazolyl group into the Ru complex allow the avoidance of the charge build-up, leading to the decrease of the overpotential.[Chapter 1]

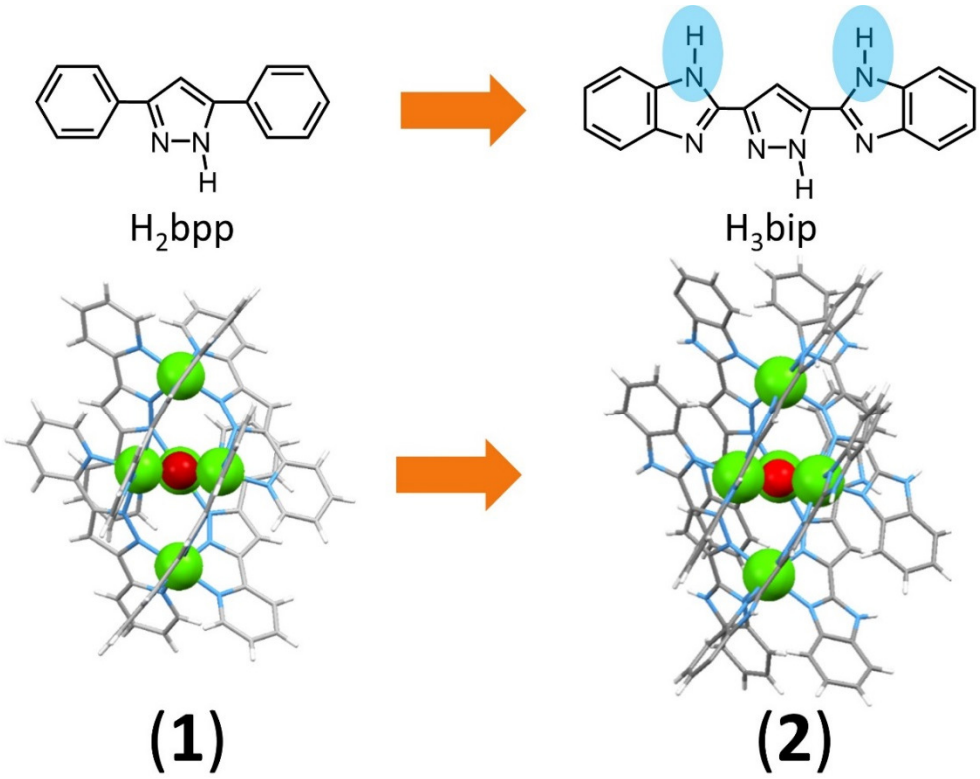

Figure 1. Introduction of the PCET sites in the pentanuclear complex.

Synthesis

The complex **2** was synthesized by the reaction of $Fe(ClO_4)_2 \cdot 6H_2O$ and 1 equiv. H_3bip with base in a DMF/H_2O mixed solution at 90 °C for 5 hours. **2** was isolated as the $Fe^{II}_4Fe^{III}$ oxidation state, which one iron ion of **2** was oxidized to Fe^{III}. Single crystals of **2** suitable for X-ray analysis were grown by a vapor diffusion of Et_2O into a MeOH solution of the complex. The X-ray crystallographic structure and summary of the crystallographic data for **2** are shown in Figure 2 and Table 1 respectively. **2** crystallized in the space group *P* 2/*n*, with crystallographically unique two half of the pentanuclear complex in the asymmetric unit. The coordination geometry of the five iron ions can be categorized into two types, three iron ions at the centered triangle and two iron ions in apical position. The three iron ions at the triangle [$Fe_3(\mu_3\text{-}O)$] core shows a distorted trigonal-bipyramidal geometry, being coordinated by two H_2bip^- and an O^{2-} anion. As shown in Figure 3, the Fe-O-Fe angles is similar in the comparison with that of **1** and the Fe-O bonds in the complex **2** have an average length of 1.923(3) Å, close to that of **1** (1.940(3) Å), indicating the same coordination environment of the triangle core. On the other hand, the two iron ions at the apical positions have distorted octahedral coordination geometries, being coordinated by three H_2bip^- to form [$Fe(\mu\text{-}H_2bip)_3$] units. The average Fe_{apical} N bond length in **2** is 2.208(3) Å, which is much prolonged than that in **1** (1.990(3) Å), presumably due to the steric repulsion of the benzimidazolyl moieties.

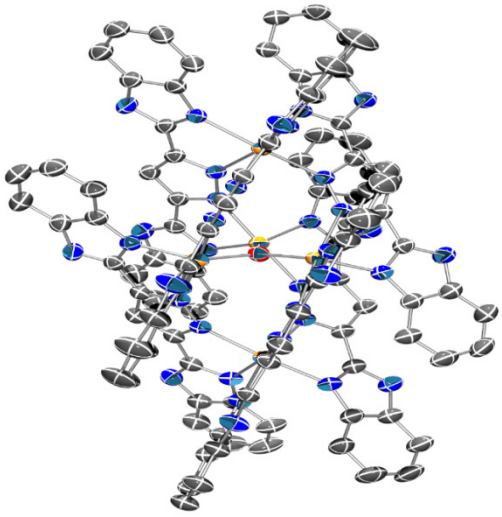

Figure 2. An ORTEP drawing (50% probability ellipsoids) of one of two crystallographically independent units in **2**$(PF_6)_3$ (hydrogen atoms are omitted for clarity).

Table 1. Summary of the crystallographic data for **2** $(PF_6)_3$.

Formula	$C_{204}H_{130}F_{36}Fe_{10}N_{72}O_2P_6$
Fw	5050.11
Crystal color, habit	brown, block
Crystal size, mm^3	0.60 × 0.21 × 0.10
Crystal system	monoclinic
Space group	*P 2/n*
a, Å	25.9630(5)
b, Å	15.3697(3)
c, Å	31.5282(6)
β, deg	96.9240(7)
Z	2
F(000)	5096.0
d_{calc}, g/cm^3	1.343
μ(MoKα), mm^{-1}	0.690
T, K	123(2)
R_1	0.069
wR_2	0.2269
GOF	1.088

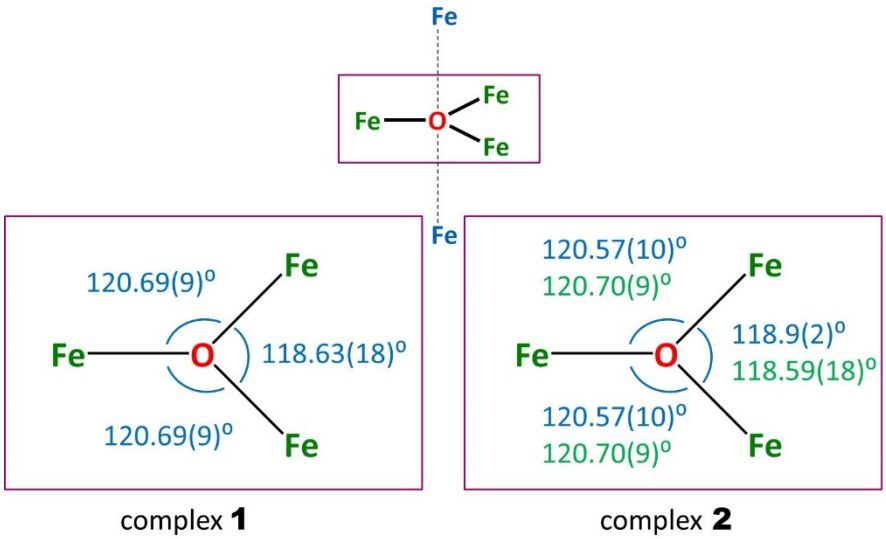

Figure 3. Comparison of the structure of the triangle [$Fe_3(\mu_3\text{-}O)$] core for **1** and **2**.

UV-visible Absorption Spectra

The proton dissociation behavior has been studied quantitatively by performing spectrophotometric titrations of the complex (Fig 4). The addition of the base up to 1.0 equiv. triazabicyclodecene (TBD) showed well-defined isosbestic point (*ca*. 320 nm) suggesting a clean deprotonation from the complex. The second deprotonation process occurred by the addition of more 1 equiv. TBD, accompanying an isosbestic point at 316 nm. Further addition of TBD (up to 3.0 equiv.), caused much larger spectral change with isosbestic point (*ca.* 355 nm), and resulted in the gradual precipitation due to the neutralization by three H^+ release. A reverse titration in which p-toluenesulfonated acid added to the dispersed solution of the complex, led to an immediate recovery of spectra. These results indicate three acid–base equilibrium associated with the protonation/deprotonation of the H_2bip moiety.

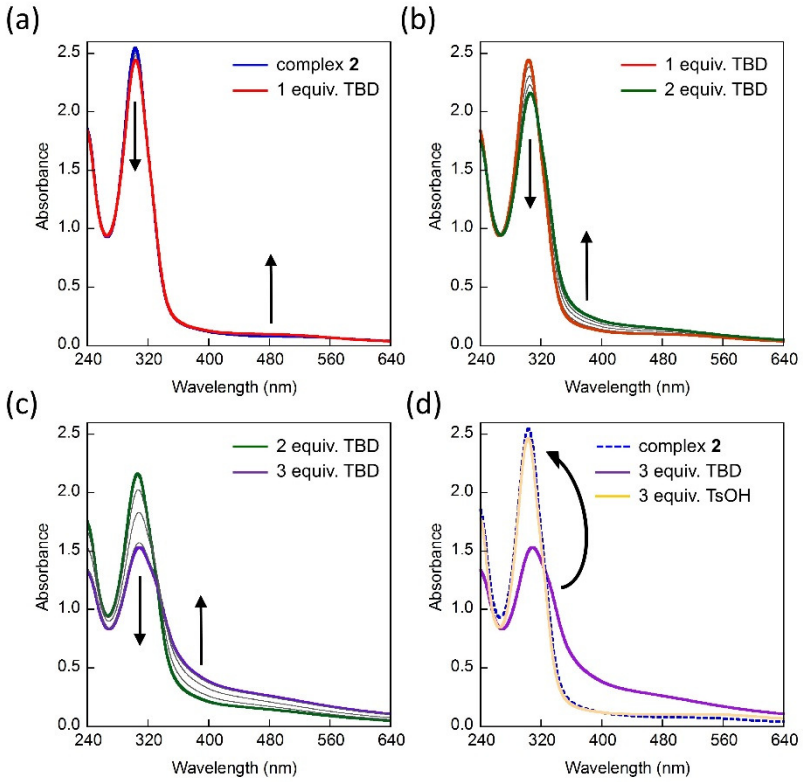

Figure 4. UV-Visible spectral changes of the complex (0.011 mM) in acetonitrile upon the addition of triazabicyclodecene (TBD) and *p*-toluenesulfonate (TsOH): (a) 0 – 1 equiv. TBD, (b) 1 – 2 equiv. TBD, (c) 2 – 3 equiv. TBD (d) 3 equiv. TBD and 3 equiv. TsOH.

Cyclic Voltammetry

The cyclic voltammogram (CV) of **2** (0.2 mM) was measured in a γ-butyrolactone solution containing Et_4NClO_4 (0.1 M) at a scan rate of 10 mV s^{-1}. As shown in Figure 5, there are four reversible oxidation waves at $E_{1/2}$ = – 0.11, 0.27, 0.61, 0.95 V *vs.* ferrocene/ferrocenium (Fc/Fc^+). This five redox processes were assigned to the sequential one-electron redox couple of each iron ion between Fe^{II} and Fe^{III}. The open-circuit potential of **2** was determined to be –0.08 V, indicating that **2** possesses the $Fe^{II}_4Fe^{III}$ state in both the solution and solid states (*vide supra*). The redox behaviour of **2** is basically similar to that of **1** except for small negative shift of the oxidation potential (Table 2). The potential shifts are due to stronger σ donating ability of the imidazolyl group than that of pyridyl group.

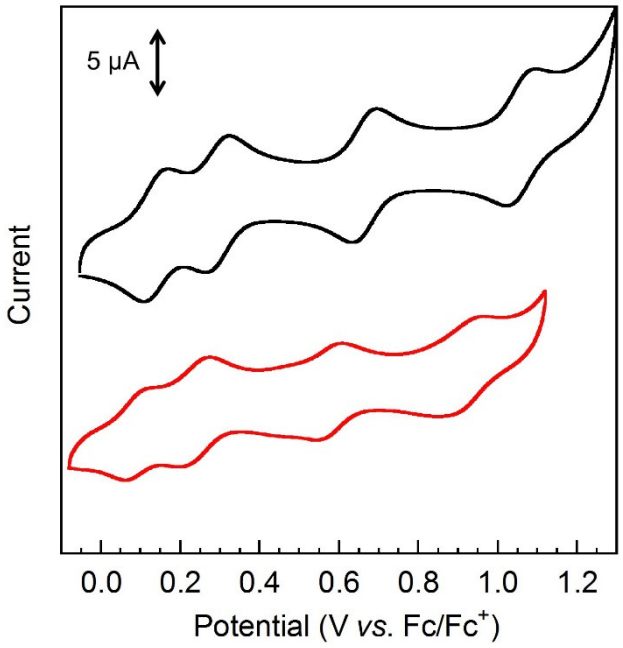

Figure 5. Cyclic voltammograms of **2** and **1** (0.2 mM) in γ-butyrolactone solution.

Table 2. Redox potentials for **1** and **2** in γ-butyrolactone solution.

Complex	Potential (V *vs.* Fc/Fc^+)			
	$E_{1/2}$ (1)	$E_{1/2}$ (2)	$E_{1/2}$ (3)	$E_{1/2}$ (4)
1	0.14	0.30	0.67	1.05
2	0.11	0.27	0.61	0.95

The proton dissociation ability of **2** is expected to exhibit PCET in aqueous conditions, however the analysis of **2** in solution containing H_2O can't be done because of the poor solubility of **2** in water. Therefore, we made a Nafion/Complex layer on the electrode surface and used the modified electrode for electrochemical measurements in aqueous media (Fig. 6). The CV with the modified electrode in phosphate buffer solution (pH =2.0) revealed four oxidation waves (Fig. 7). Importantly, the profile of the cyclic voltammogram of **2** changed dramatically when the CV was performed at pH = 5.0, as shown in Figure 7. The third and fourth waves were largely shifted to a negative direction, while the first and second waves were slightly shifted, resulting the overlap of the second and third waves.

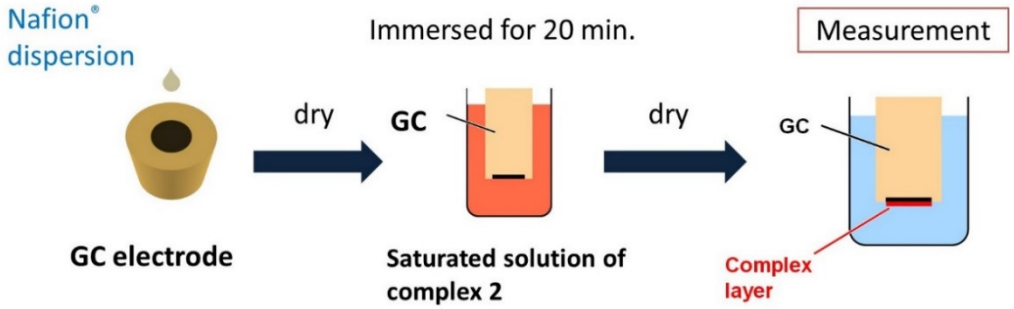

Figure 6. Illustration of the modification method of **2** in the electrode.

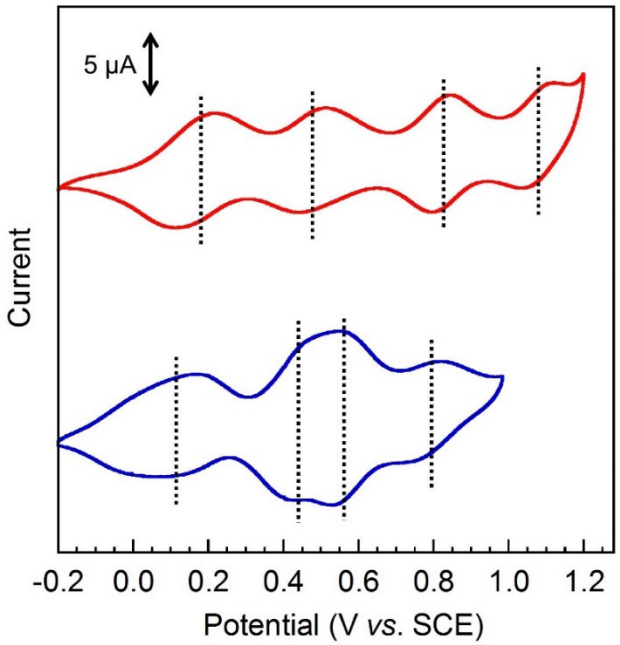

Figure 7. Cyclic voltammograms of **2**/GC in buffer solutions at pH 2 (red line) and 5 (blue line).

The pH-dependent shift was also confirmed by the square wave voltammetry (SWV). Based on the data from SWV, the potential versus pH (Pourbaix) diagram was made for **2** over the range of 1 < pH < 7 in buffer solution (Fig. 8). According to the Nernstian relationship described bellow[6], the slope in this diagram is equivalent to –(m/n)0.059 V/pH, where m and n represent the number of protons and electrons transferred, respectively.

$$\mathrm{Ox} + \mathrm{m}H^{+} + \mathrm{n}e^{-} \rightleftharpoons \mathrm{Red}$$

$$E_{1/2} = E^{\mathrm{o}'} - \frac{\mathrm{m}}{\mathrm{n}} 0.059\mathrm{pH}$$

Thus, all of the species can be identified as shown in Figure 8. For example, the first oxidation waves were observed at a potential of around 0.2 V in low pH region (1 < pH < 4), indicating non-PCET process. In contrast, plots in the higher pH range (4 < pH < 7) shows linear decrease with a slope of –0.059 V/pH, indicating the one electron and one proton process. The second and third oxidation is much complicated and two peaks are overlapped from pH 5 because of presence of the non-PCET process in the second oxidation. When the pH is more than 5, **2** shows sequentially occurring 4 step PCET processes.

Importantly, **2** exhibits pH-dependence of the oxidation potential, which is not observed in **1**. As a result, the oxidation of **2** required to form the Fe^{III}_5 state is (0.8 V *vs*. SCE), much smaller than that of **1** (1.39 V). These different electrochemical properties reveal that the ligands bearing proton dissociative sites can play a key role in lowering the potentials through PCET which avoid the charge buildup during oxidation of the complex. Finally, the catalysis of electrochemical water oxidation was evaluated. Cyclic voltammogram of **2** in buffer solution exhibits a large irreversible anodic current, which is considered to be a catalytic current attributed to water oxidation. Moreover, the behavior of the catalytic current of the water oxidation was changed depending on the pH. As shown in Figure 9, the onset potentials of the water oxidation were negatively shifted in response to the pH.

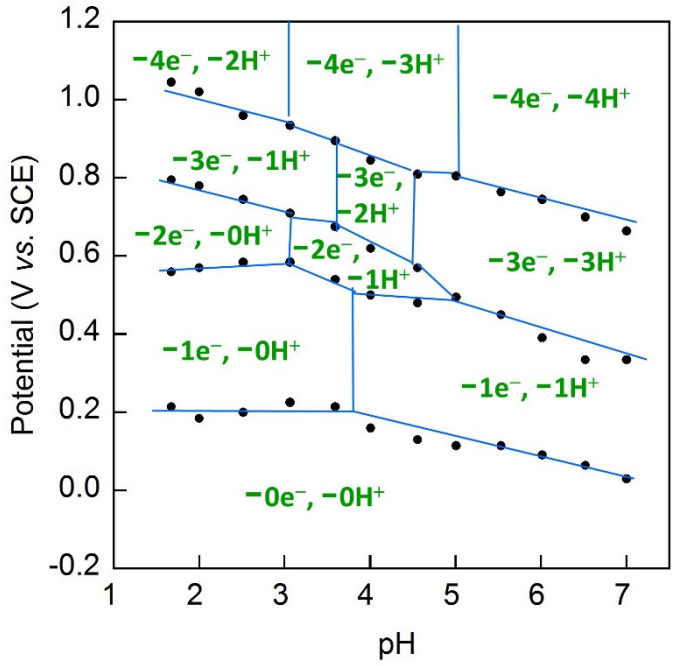

Figure 8. Plots of $E_{1/2}$ (V *vs*. SCE) *vs*. pH (Pourbaix diagram) for **2**. Symbols of me^-, nH^+ are abbreviations for oxidized/deprotonated forms of **2**, where m and n are the numbers of removed electrons and protons, respectively.

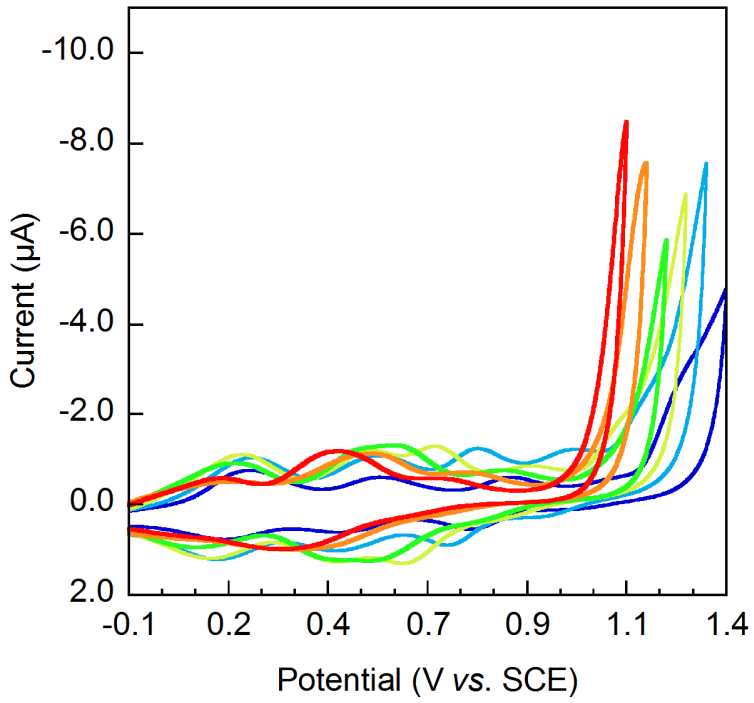

Figure 9. Cyclic voltammograms of **2**/GC in buffer solutions from pH 7 to pH 2.

In conclusion, the complex bearing PCET sites was synthesized and electrochemical properties and catalytic activities were investigated. The cyclic voltammetry (CV) at various pH using the complex-modified electrode revealed pH-dependent shifts in the oxidation potentials, which is not observed in **1**. Furthermore, the catalytic current attributed to water oxidation was observed at lower oxidation potential than that of **1**. The rational and substantial design described here opens up new avenues for the development of water oxidation catalysts for sustainable energy conversion systems.

Materials and Methods

Materials.

$NaPF_6$ and $Fe(ClO_4)_2 \cdot 6H_2O$ were purchased from Wako Pure Chemical Industries, Ltd. Tetraethylammonium perchlorate (TEAP), 1,8-diazabicyclo[5.4.0]-7-undecene (DBU) and p-toluenesulfonic acid (TsOH) monohydrate were purchased from Tokyo Chemical Industry Co., Ltd. 1,5,7-Triazabicyclo[4.4.0]dec-5-ene (TBD) and Nafion® perfluorinated resin, aqueous dispersion (10 wt%) were purchased from Aldrich Chemical Co. Inc. H_2O was purified using a Millipore MilliQ purifier. Dry acetonitrile (CH_3CN) was degassed and purified under N_2 atmosphere using a GlassContour solvent system (Nikko Hansen Co., Ltd.). All solvents and reagents are of the highest quality available and used as received except for tetraethylammonium perchlorate. Tetraethylammonium perchlorate was recrystallized from absolute ethanol. 3,5-bis(2-benzimidazolyl)pyrazole (H_3bip) was prepared using a literature method.[7]

Synthesis of $[\{Fe^{II}(\mu\text{-}H_2bip)_3\}_2\, Fe^{II}_2Fe^{III}\,(\mu\text{-}O)](PF_6)_3 \cdot 9H_2O$ ($2(PF_6)_3 \cdot 9H_2O$).

3,5-bis(2-benzimidazolyl)pyrazole (H_3bip; 1.0 mmol, 301.2 mg) was dissolved in DMF with 1,8-Diazabicycloundec-7-ene (1.3 mmol, 194 μl). $Fe(ClO_4)_2 \cdot 6H_2O$ (1.0 mmol, 367.7 mg) was then added to the solution and the reaction mixture was heated at 90 ºC for two hours. After filtration, an aqueous $NaPF_4$ solution was added to the filtrate to result in the precipitate. The precipitate was collected by filtration and recrystallized from Et_2O/CH_3OH to give dark orange crystals. Yield 144.8 mg (32%). Elemental analysis Calcd. for **2**$(PF_6)_3 \cdot 9H_2O$: $C_{102}H_{84}F_{18}Fe_5N_{36}O_{10}P_3$: C, 45.57; H, 3.15; N, 18.76%. Found: C, 45.59; H 3.22; N 18.78%. ESI-TOF MS (positive ion, acetonitrile): m/z: 697.1 $[\{Fe^{II}(\mu\text{-}H_2bip)_3\}_2Fe^{II}_2Fe^{III}(\mu\text{-}O)]^{3+}$.

Measurement Apparatus.

UV-visible absorption spectra were recorded on a SHIMADZU UV-1800 UV/Visible spectrophotometer. Elemental analyses were carried out on a J-SCIENCE LAB MICRO CORDER JM10 elemental analyser. ESI-TOF mass spectra were recorded on a JEOL JMS-T100LP mass spectrometer.

X-ray Crystallography.

A crystal of **2**$(PF_6)_3$ were mounted in a loop. Diffraction data at 123 K were measured on a RAXIS-RAPID Imaging Plate diffractometer equipped with confocal monochromated Mo-Kα radiation and data was processed using RAPID-AUTO (Rigaku). The structure was solved by direct method using *SIR-92* [8] and refined by the full-matrix least squares techniques on F^2 (*SHELXL-97* [9]). All non-hydrogen atoms were refined anisotropically and refined with a riding model with U_{iso} constrained to be 1.2 times U_{eq} of the carrier atom. The diffused electron densities resulting from residual solvent molecules were removed from the data set using the SQUEEZE routine of PLATON [10] and refined further using the data generated.

Electrochemical Measurements.

All experimental procedures were conducted at ambient temperature, 20 ºC, under argon. A standard three-electrode configuration was employed in conjunction with a CH Instruments potentiostat interfaced to a computer with CH Instruments 650 DKMP software. Cyclic voltammetry was performed using a GC disk working electrode (diameter 3 mm, from BAS).

Preparation method of the GC electrode modified with 2.

Nafion dispersion in MeOH (0.05 wt%) was dropped on the electrode and dried it in the oven. The electrode was then immersed in a saturated solution of **2** in methanol for 20 min. followed by washing them with absolute methanol. Then, it was dried again and used in the electrochemical measurements.

References

1. Y. Umena, K. Kawakami, J.-R. Shen and N. Kamiya, *Nature* **2011**, *473*, 55.
2. G. C. Dismukes, R. Brimblecombe, G. A. N. Felton, R. S. Pryadun, J. E. Sheats, L. Spiccia and G. F. Swiegers, *Acc. Chem. Res.* **2009**, *42*, 1935.
3. H. Dau, I. Zaharieva, *Acc. Chem. Res*. **2009**, *42*, 1861.
4. a) G. W. Brudvig and R. H. Crabtree, *Prog. Inorg. Chem.* **1989**, *37*, 99; b) T. J. Meyer, *Acc. Chem. Res.* **1989**, *22*, 163; c) W. Rüttinger and C. Dismukes, *Chem. Rev.* **1997**, *97*, 1; d) M. Yagi and Kaneko, *Chem. Rev.* **2001**, *101*, 21; d) I. Romero, M. Rodríguez, C. Sens, J. Mola, M. R. Kollipara, L. Francàs, E. Mas-Marza, L. Escriche and A. Llobet, *Inorg. Chem.* **2008**, *47*, 1824; e) D. J. Wasylenko, R. D. Palmer and C. P. Berlinguette, *Chem. Commun.* **2013**, *49*, 218; f) A. Singh and L. Spiccia, *Coord. Chem. Rev.* **2013**, *257*, 2607; g) T. Kikuchi and K. Tanaka, *Eur. J. Inorg. Chem.* **2014**, *4*, 607.
5. a) W. C. Ellis, N. D. McDaniel, S. Bernhard and T. J. Collins, *J. Am. Chem. Soc.* **2010**, *132*, 10990; b) J. L. Fillol, Z. Codolà, I. Garcia-Bosch, L. Gómez, J. JoséPla and M. Costas, *Nature Chem.* **2011**, *3*, 807; c) Hong, D. S. Mandal, Y. Yamada, Y.-M. Lee, W. Nam, A. Llobet and S. Fukuzumi, *Inorg. Chem.* **2013**, *52*, 9522; d) M. K. Coggins, M.-T. Zhang, A. K. Vannucci, C. J. Dares and T. J. Meyer, *J. Am. Chem. Soc.* **2014**, *136*, 5531.
6. a) M. H. Huynh and T. J. Meyer, *Chem. Rev.* **2007**, *107*, 5004; b) J. J. Warren, T. A. Tronic and J. M. Mayer, *Chem. Rev*. **2010**, *110*, 6961.
7. S. Baitalik, U. Flörkeand and K. Nag, *Inorg. Chem*. **1999**, *38*, 3296.
8. A. Altomare, G. Cascarano, C. Giacovazzo and A. Guagliardi, *J. Appl. Cryst*. **1933**, *26*, 343.
9. G. M. Sheldrick, *Program for Crystal Structure Refinement*, University of Göttingen, Germany, **1997**.
10. A. L Spek, *Acta Cryst*. **2009**, D*65*, 148.

General Conclusion

The development of efficient catalysts for water oxidation is difficult to achieve because the reaction requires the loss of $4e^-$ and $4H^+$ and the formation of the O-O bond from two water molecules. In this thesis, three keys, (1) introduction of PCET modules, (2) accumulation of metal ions and (3) installation of adjacent water activation sites, were suggested to realize water oxidation with high efficiency and a low overpotential.

The introduction of PCET modules into water oxidation catalysts was demonstrated in Chapter 1. Ru complex bearing two kinds of PCET modules (H_2bim and M–OH_2) was developed and found to exhibit an interesting acid-base and redox behavior. The Ru complex showed a four-step PCET process to give a four-electron oxidized species without electrostatic charge buildup during the reaction. As a result, the complex served as a water oxidation catalyst with a low overpotential.

The effects of the accumulation of metal ions and the installation of adjacent water activation sites were discussed in Chapter 2. The pentanuclear iron catalyst which satisfies these two requirements was employed as a catalyst for electrochemical water oxidation. As a result, the pentairon complex served as a water oxidation catalyst with the turnover frequency of 1,900 s^{-1}, which is more than 1,000 times greater than those of other reported iron-based catalysts. Thus, the author believes that the approach described in Chapter 2 may open a new door for developing molecular catalysts with extremely high activity.

Although the finding of the pentanuclear iron complex offers a new strategy for creating efficient molecular catalysts for water oxidation, a large overpotential of more than 0.5 V remain a major challenge in this system. In Chapter 3, the idea described in Chapter 1, the introduction of PCET modules, was applied to the pentairon catalyst. Indeed, a pentanuclear iron complex bearing PCET-active ligand (H_2bip) was newly synthesized and characterized. The electrochemical measurements in aqueous media revealed multiple PCET processes in the redox reactions of the complex. Moreover, the onset of the catalytic current was found to exhibit pH dependence, thus resulting in water oxidation with a low overpotential.

The pentanuclear iron catalyst bearing PCET modules, described in Chapter 3, is considered the ideal catalyst with the three keys, (1) introduction of PCET modules, (2) accumulation of metal ions and (3) installation of adjacent water activation sites. However, although the overpotential for water oxidation was found to be much decreased in comparison with that of the parent pentairon catalyst, the reaction rate also seems to be decreased judging from the intensity of catalytic current for water oxidation. This may be due to the high activation energy in the rate-determining step. Theoretical calculations

demonstrated in Chapter 2 suggested that the rate-determining step of the water oxidation catalyzed by the pentairon complex is the water attack process which requires space open between two π-stacked ligands. The author now assumes that the strong π-π interaction between H_2bip ligands causes a high activation barrier of the water insertion process. Therefore, a design of PCET-active ligands to have a moderate inter-ligand π-π interaction should be a promising way to create a water oxidation catalyst with high activity and with a low overpotential.

Acknowledgements

I have been studied from April 2011 to March 2016 under the direction of Associate Professor Shigeyuki Masaoka in the Institute for Molecular Science and express gratitude for his impassioned guidance, encouragement and valuable discussion. His sincere attitude and passion for Science, and creative thinking inspired me and contributed to my growth as a scientist. I am deeply grateful to Assistant Professor Mio Kondo for kind guidance, encouragement, and fruitful discussion. I could learn a lot from her about the insight based on a logical approach and a broader perspective. I would like to thank Assistant Professor Masaki Yoshida in Hokkaido University for giving me numerous knowledge of chemistry and helpful advices. I sincerely acknowledge Ms. Reiko Kuga for friendly attitude and many experimental assistance. I would not be where I am without her cooperation. I also gratefully acknowledge Dr. Vijayendran K. K. Praneeth for experimental support. I am deeply grateful to Professor Dr. Ken Sakai in Kyushu University for many advices and guidance.

I wish to thank our members in the Institute for Molecular Science, Mr. Takahiro Itoh, Mr. Yuki Okabe, Ms. Pondchanok Chinapang, Ms. Arisa Fukatsu, Ms. Yukino Fukahori, Mr. Sze Koon Lee, Mr. Takafumi Enomoto, Mr. Hitoshi Izu, Mr. Riku Ushijima, Ms. Reiko Kuga, Ms. Mari Kanaike and Ms. Akane Shibata, for the kind support, encouragement, valuable discussion, and friendship. I also wishes to express sincere thanks to our graduated member, Ms. Sena Torii, Mr. Masakazu Murase, Ms. Kaori Wakabayashi, Mr. Ke Liu and Dr. Go Nakamura. I also grateful to Ms. Mayuko Taniwake and Ms. Kyoko Nogawa for their clerical support.

I gratefully acknowledge Professor Shinya Hayami in Kumamoto University for the measurement of the Mössbauer spectroscopy, Associate Professor Takeshi Yanai and Assistant Professor Yuki Kurashige in the Institute for molecular Science for the quantum chemistry calculations, Assistant Professor Ko Yoneda in Saga University and Professor Satoshi Kawata in Fukuoka University for the advice in the synthesis of the penta-nuclear complex, and Professor Tetsuro Murahashi in the Institute for Molecular Science for the kind use of the single-crystal X-ray diffraction instrumentation.

I am deeply grateful to Professor Koji Tanaka, Assistant Professor Katsuaki Kobayashi in Kyoto University, Associate Professor Hideki Ohtsu in Toyama University, and Professor Koichi Kato in the Institute for molecular Science and Associate Professor Takumi Yamaguchi in Japan Advanced Institute of Science and Technology for kindly support in the lab rotation. I also gratefully acknowledge Professor Toshi Nagata in Meijo University, Professor Hidehiro Sakurai in Osaka University, Assistant Professor Shuhei Higashibayashi, Associate Professor Norie Momiyama, Assistant Professor Atsuto Izumiseki, Assistant Professor Takuya, Kurahashi in the Institute for molecular Science, and the other members in the joint seminar for a lively discussion of chemistry.

I would like to thank Assistant Professor Eric J. Schelter and his group members in University of Pennsylvania for invaluable experiences through the internship.

I am indebted to my colleagues at Kyushu University, Mr. Kyoji Kitamoto, Mr. Tomohiro Shinto, Ms. Yuki Nakamura, who inspired and encouraged me.

I would like to thank everyone who gave me valuable advice and precise comments to my work.

I gratefully acknowledge the financial support of the Research Fellowships of the Japan Society for the Promotion of Science for Young Scientists.

List of Publications

Chapter 1

Masaya Okamura, Masaki Yoshida, Reiko Kuga, Ken Sakai, Mio Kondo and Shigeyuki Masaoka
"A Mononuclear Ruthenium Complex Showing Multiple Proton-Coupled Electron Transfer toward Multi-electron Transfer Reactions"
Dalton Trans. **2012**, *41*, 13081.

Chapter 2

Masaya Okamura, Mio Kondo, Reiko Kuga, Yuki Kurashige, Takeshi Yanai, Shinya Hayami, Vijayendran K. K. Praneeth, Masaki Yoshida, Ko Yoneda, Satoshi Kawata and Shigeyuki Masaoka
“A pentanuclear iron catalyst designed for water oxidation”
Nature accepted.

Chapter 3

Masaya Okamura, Reiko Kuga, Satoshi Kawata, Mio Kondo and Shigeyuki Masaoka
“Water oxidation reaction catalyzed by a penta-nuclear iron complex bearing PCET sites”
Manuscript in preparation.

Other Publications

Tomomi Koshiyama, Nao Kanda, Koki Iwata, Masayuki Honjo, Sana Asada, Tatsuru Hatae, Yasuhiro Tsuji, Masaki Yoshida, **Masaya Okamura**, Reiko Kuga, Shigeyuki Masaoka, and Masaaki Ohba
"Regulation of Cerium(IV)-driven O_2 Evolution Reaction using Composites of Liposome and Lipophilic Ruthenium Complexes"
Dalton Trans. **2015**, *44*, 15126.

Masaya Okamura

"A pentanuclear iron catalyst designed for water oxidation"

Bull. Jpn. Soc. Coord. Chem. **2015**, *65*. 18.

Masaya Okamura and Shigeyuki Masaoka
"Design of Mononuclear Ruthenium Catalysts for Low-Overpotential Water Oxidation"
Chem. Asian J. **2015***, 10,* 306.

Go Nakamura, **Masaya Okamura**, Masaki Yoshida, Takayoshi Suzuki, Hideo D. Takagi, Mio Kondo, and Shigeyuki Masaoka
"Electrochemical Behavior of Phosphine-Substituted Ruthenium(II) Polypyridine Complexes with a Single Labile Ligand"
Inorg. Chem. **2014**, *53*, 7214.

Arisa Fukatsu, Mio Kondo, **Masaya Okamura**, Masaki Yoshida, and Shigeyuki Masaoka
"Electrochemical response of metal complexes in homogeneous solution under photoirradiation"
Sci. Rep. **2014**, *4*, 5327.

岡村将也, 正岡重行
〝プロトン共役電子移動を示す有機配位子を導入した多電子移動錯体触媒〟
ペトロテック **2013**, *36*, 613.